

THESIS

SEMI-RIGID STEEL FRAMES SUBJECTED TO MAINSHOCK-AFTERSHOCK  
EARTHQUAKE SEQUENCES

Submitted by

Sushant Ajay Admuthe

Department of Civil and Environmental Engineering

In partial fulfilment of the requirements

For the Degree of Master of Science

Colorado State University

Fort Collins, Colorado

Spring 2018

Master's Committee:

Advisor: Hussam Mahmoud

Rebecca Atadero  
Scott Shuler

Copyright by Sushant Ajay Admuthe 2018  
All Rights Reserved

## ABSTRACT

### SEMI-RIGID STEEL FRAMES SUBJECTED TO MAINSHOCK-AFTERSHOCK EARTHQUAKE SEQUENCES

In a typical seismic event, large number of aftershocks are generally triggered due to the complex interaction within and between tectonic plates. Despite the fact that aftershocks are typically smaller in magnitude than mainshocks, their ground-motion intensity, measured by peak ground acceleration, is not always smaller. As a result, vulnerability of structures to extensive damage and complete collapse as a result of the aftershocks increases. In spite of their in evaluating the true risk of system failure and collapse, the inclusion of aftershocks in code provisions and guidelines for seismic risk assessment and performance-based engineering is lacking.

In this study, three semi-rigid frames, with connection capacity of 50%, 60% and 70% of the plastic moment of the beam, were designed and their performance under mainshock-aftershock sequences assessed. The objective of this study, pertaining to the seismic performance of the frames, was twofold. First was to develop fragility functions for the frames under sequential mainshock-aftershock hazards as the basic ingredient for performance-based engineering. Second, was to evaluate the extent of spread of inelasticity and period elongation as a result of the sequential events. The first objective was realized through performing incremental dynamic analysis (IDA) using a new set of ground-motion records, with naturally available aftershock data. Scaling of the aftershocks for the IDA was performed while maintaining the Peak Ground

Acceleration (PGA) relationship, established priori, between the respective mainshock and aftershock events. The results showed that the inclusion of the aftershocks increase the probability of reaching or exceeding a particular damage state. The increase in the probability is higher for the complete damage state and lower for the slight damage state. In other words, the probability, of the structure slightly or moderately damaged in the mainshock, to exceed the same damage state is not increased in aftershocks but in the case of extensive and complete damage, there is considerable increase in the probability of exceeding the same damage state in aftershock. In addition assessment of the spread of inelasticity and period elongation, performed using Short-Term-Fourier-Transformation, show that a relationship between the elongated period and connection capacities for different ground-motion intensities can be established.

## ACKNOWLEDGEMENTS

I would first like to thank my thesis advisor Dr. Hussam Mahmoud for his excellent technical guidance, patience and motivation over the past years of my graduate school. The door to Dr. Mahmoud's office was always open whenever I ran into a trouble spot or had a question about my research or writing. He consistently allowed this research to be my own work, but steered me in the right the direction whenever he thought I needed it. His guidance helped me in all the time of research and writing of this thesis. I could not have imagined having a better advisor and mentor for my master's study.

Besides Dr. Mahmoud, I would like to thank the rest of my thesis committee Dr. Rebecca Atadero, Dr. Scott Shuler for their insightful comments and encouragement, but also for the hard questions which incented me to widen my research from various perspectives.

I would also like to acknowledge Mr. Hassan Emad, Ph.D., Colorado State University as the second reader of this thesis, and I am gratefully indebted to his for his very valuable guidance and comments on this thesis.

Finally, I must express my very profound gratitude to my parents, my brother and to my friends for providing me with unfailing support and continuous encouragement throughout my years of study and through the process of researching and writing this thesis. This accomplishment would not have been possible without them. Thank you.

## TABLE OF CONTENTS

ABSTRACT .....	ii
LIST OF TABLES .....	viii
LIST OF FIGURES .....	x
CHAPTER 1. INTRODUCTION.....	1
1.1. Problem Statement .....	1
1.2. Objectives and Scope of the Research .....	3
1.3. Organization of the Dissertation .....	5
CHAPTER 2. LITERATURE REVIEW AND BACKGROUND .....	7
2.1. Earthquake Design Philosophy .....	7
2.2. Moment Resisting Curves for Semi Rigid Connections .....	9
2.3. Mainshock and Aftershock Relationship .....	15
2.4. Simulation of mainshock-aftershock sequences .....	19
2.5. Effects of Mainshock-Aftershock Sequences on Steel Frames.....	20
2.6. Period Elongation.....	23
CHAPTER 3. MODEL DESCRIPTION & DESIGN .....	28
3.1. Description of the Building.....	28
3.2. Loads and Load Combinations.....	30

3.3.	Seismic Constants .....	31
3.4.	Materials and Modelling .....	32
3.5.	Design Procedure .....	34
3.6.	Connection Design Assumptions .....	35
3.7.	Global Analysis .....	36
3.8.	Structural Properties of the joints.....	37
3.9.	Connection Design procedure .....	40
3.10.	Modeling Approach.....	44
CHAPTER 4. METHODOLOGY .....		50
4.1.	Pushover Analysis .....	50
4.2.	Eigenvalue Analysis .....	58
4.3.	Dynamic Time History Analysis.....	59
4.4.	Dynamic Analysis using Zeus-NL .....	59
4.6.	Incremental Dynamic Analysis .....	79
4.7.	Period Elongation.....	87
CHAPTER 5. RESULTS AND OBSERVATIONS .....		98
5.1.	Pushover Analysis .....	98
5.2.	Eigenvalue Analysis .....	103
5.3.	Incremental Dynamic Analysis .....	104
5.4.	Assessment of Fragility Function Parameters .....	112

5.5. Period Elongation.....	122
CHAPTER 6. SUMMARY AND CONCLUSIONS .....	127
6.1. Summary of current work .....	127
6.2. Conclusions .....	128
REFERENCES .....	130
APPENDIX A. STEEL CONNECTION DESIGN .....	138
General .....	138
Strong-axis Calculation .....	139
Connection analysis: Side [beam] .....	139
APPENDIX B. EARTHQUAKES RECORDS FROM PEER NGA DATABASE.....	153

## LIST OF TABLES

Table 3.1 Seismic Constants Considered in the study .....	32
Table 3.2 Beams and Columns sections .....	35
Table 3.3: Type of Joint Model after [55].....	37
Table 3.4 : Plastic Capacities of beam sections and Connection Moment Capacities.....	39
Table 3.5 : Connection configuration details for beam W21X50.....	41
Table 3.6: Connection configuration details for beam W18X35 .....	42
Table 3.7 : Connection initial stiffness .....	43
Table 4.1 Calculated Design Base Shear .....	53
Table 4.2 Floor heights and weights .....	54
Table 4.3 Lateral load distribution for the model frames .....	54
Table 4.4 Magnitude to PGA conversion .....	73
Table 4.5 Example Damage States from Hazus [61].....	82
Table 4.6 Model building type from Hazus [61] .....	84
Table 4.7 Inter-story drift ratio of structural damage sates considered in this study .....	84
Table 5.1 Initial stiffness and the connection capacities of the model frames .....	99
Table 5.2 Maximum strength, design strength and over-strength factor of the model frames with their respective connection capacities.....	101
Table 5.3 Yield displacement, ultimate displacement and ductility ratio of the model frames with their respective connection capacities.....	102
Table 5.4 Modes and fundamental periods.....	104

Table 5.5 Fragility Function Parameters for model frames under FEMA-P965 Ground-motions Record Set.....	114
Table 5.6 Fragility function parameters for model frames under selected mainshocks ground-motion record set.....	115
Table 5.7 Fragility Parameters for model frames under selected Mainshock-Aftershock Sequences.....	117
Table B.1 Far-field ground motion records set.....	153
Table B.2 Site and source data for far-field records set.....	154
Table B.3 Summary of PEER NGA Database information and parameters for far-field set .....	155
Table B.4 Mainshock ground motions downloaded from PEER NGA Database .....	156
Table B.5 Aftershock ground motions downloaded from PEER NGA Database .....	160
Table B.6 Details of the selected mainshocks for the analysis .....	163
Table B.7 Details of the selected aftershocks for the analysis.....	164
Table B.8 PGA values of the mainshock horizontal components .....	164
Table B.9 PGA values of the aftershock horizontal components .....	166
Table B.10 PGA values for the mainshock and aftershock records scaled for 70% $M_{pb}$ Model.	167

## LIST OF FIGURES

Figure 2.1 Connection classification based on moment rotation curve and beam line.....	9
Figure 2.2 Classifications of connections by stiffness in accordance with Eurocode 3 .....	13
Figure 2.3 Tri-linear elasto-plastic model for joint behavior.....	14
Figure 2.4 Difference between the mainshock magnitude and magnitude of its largest aftershock versus the magnitude of the mainshock .....	17
Figure 2.5 Pattern Classification for Signal Processing.....	27
Figure 3.1: (a) Plan view and (b) Elevation view of the sample building .....	30
Figure 3.2 Bilinear elasto-plastic material model.....	33
Figure 3.3 (a) Configuration of the beam and column elements along with the rotational springs, (b) Idealized moment-rotation curve with stiffness degradation .....	34
Figure 3.4 (a) Schematic of an end-plate connection, (b) Design moment-rotation characteristic for a joint: after [55].....	38
Figure 3.5 : Components of connection behavior: after [13].....	39
Figure 3.6 (a) Moment-rotation curve for connection to beam W21X50, (b) Moment-rotation curve for connection to beam W18X35 .....	44
Figure 3.7 : Joint element configuration .....	46
Figure 3.8 : Joint element modelling .....	46
Figure 3.9 : SMTR hysteretic model.....	48
Figure 3.10 : HFC hysteretic model.....	49
Figure 4.1 Design response spectrum .....	52

Figure 4.2 Lateral loads distribution.....	53
Figure 4.3 Relationship between strength, over-strength and ductility ratio: after [63].....	57
Figure 4.4 Configuration for dynamic analysis .....	61
Figure 4.5 Response spectra for far field ground motion set (44 components).....	66
Figure 4.6 (a) Normalized ground motion records (before anchoring), (b) Scaled ground motion records (after anchoring).....	67
Figure 4.7 Far-field set Scaled Response Spectra (a) for 70% $M_{pb}$ analysis model, (b) for 60% $M_{pb}$ analysis model, (c) for 50% $M_{pb}$ analysis model.....	68
Figure 4.8 (a) Magnitude of the mainshock versus the mean value of the difference between the mainshock magnitude and the magnitude of the respective largest aftershock, (b) Mainshock magnitude vs. maximum aftershock magnitude and relationship between the magnitudes of the mainshocks and aftershocks with a linear trend-line .....	72
Figure 4.9 Magnitude to PGA conversion .....	73
Figure 4.10 Relationship between mainshock and aftershock PGA values.....	74
Figure 4.11 All PGA values with current and required relationship .....	75
Figure 4.12 (a) Downloaded ground motion records from PEER NGA database and (b) final relationship between the PGA values of the selected ground motion records.....	76
Figure 4.13 (a) Response spectra of selected unscaled aftershock ground motion records and (b) Response spectra of the scaled aftershock ground motion records for 70% $M_{pb}$ analysis model .	77
Figure 4.14 Final PGA relationship for aftershock sequences scaled for 70% $M_{pb}$ model and scaled mainshocks scaled with respect to their aftershocks.....	79
Figure 4.15 Incremental dynamic analysis procedure for one earthquake record .....	82
Figure 4.16 Schematic of fragility functions and their associated damage states: after [61] .....	85

Figure 4.17 (a) Sample sinusoidal wave with frequency equal to 2Hz, (b) FFT analysis of a simple sine wave with frequency 2Hz i.e. period of 0.5 seconds .....	90
Figure 4.18 (a) Structural response of the 50% $M_{pb}$ model frame for the earthquake ‘DUZCE/BOL090’, (b) FFT analysis of the signal .....	91
Figure 4.19 (a) Sample sinusoidal wave with frequency equal to 3Hz, 2Hz and 1Hz, (b) Spectrogram of the Simple sinusoidal wave with three different frequencies.....	94
Figure 4.20 (a) Spectrogram of the sample signal and (b) Tracked frequency of the sample signal in the same time domain .....	96
Figure 5.1 (a) Pushover curves of the sample frames, (b) Pushover curves compared to the reference frame in [13].....	99
Figure 5.2 Design strength, maximum strength and over-strength factor (a) 50% $M_{pb}$ model frame, (b) 60% $M_{pb}$ model frame, (c) 70% $M_{pb}$ model frame .....	100
Figure 5.3 Relationship between the ultimate and yield displacement to the ductility ratio, (a) 50% $M_{pb}$ model frame, (b) 60% $M_{pb}$ model frame, (c) 70% $M_{pb}$ model frame.....	102
Figure 5.4 Fundamental periods and connection capacities .....	103
Figure 5.5 Incremental dynamic analysis results for FEMA-P695 records set, (a) 50% $M_{pb}$ model frame, (b) 60% $M_{pb}$ model frame, (c) 70% $M_{pb}$ model frame .....	105
Figure 5.6 Incremental dynamic analysis results for selected mainshocks only (a) 50% $M_{pb}$ model frame, (b) 60% $M_{pb}$ model frame, (c) 70% $M_{pb}$ model frame .....	106
Figure 5.7 Incremental dynamic analysis results for mainshock-aftershock sequences (a) 50% $M_{pb}$ model frame, (b) 60% $M_{pb}$ model frame, (c) 70% $M_{pb}$ model frame .....	107
Figure 5.8 Fragility curves for FEMA-P695 ground-motion record set (a) 50% $M_{pb}$ model frame, (b) 60% $M_{pb}$ model frame, (c) 70% $M_{pb}$ model frame.....	109

Figure 5.9 Fragility curves for FEMA-P695 ground-motion record set for all the analysis models .....	109
Figure 5.10 Fragility curves for selected mainshocks (a) 50% $M_{pb}$ Model Frame, (b) 60% $M_{pb}$ model frame, (c) 70% $M_{pb}$ model frame .....	110
Figure 5.11 Fragility curves for selected mainshocks for all the analysis models .....	111
Figure 5.12 Fragility curves for mainshock-aftershock sequences (a) 50% $M_{pb}$ Model Frame, (b) 60% $M_{pb}$ Model Frame, (c) 70% $M_{pb}$ Model Frame.....	112
Figure 5.13 Fragility Curves for mainshock-aftershock sequences for all analysis models.....	112
Figure 5.14 Fragility curves and fragility function parameters for FEMA-P965 ground-motions record set (a) 70% $M_{pb}$ model frame, (b) 60% $M_{pb}$ model frame and (c) 50% $M_{pb}$ model frame. ....	114
Figure 5.15 Fragility curves and fragility function parameters for selected mainshocks ground-motion record set (a) 70% $M_{pb}$ model frame, (b) 60% $M_{pb}$ model frame and (c) 50% $M_{pb}$ model frame .....	115
Figure 5.16 Fragility curves and fragility function parameters for mainshock-aftershock sequences (a) 70% $M_{pb}$ model frame, (b) 60% $M_{pb}$ model frame and (c) 50% $M_{pb}$ model frame .....	117
Figure 5.17 Comparison of fragility curves for 70% Model frame under FEMA-P695 ground-motion set and selected mainshocks record Set.....	118
Figure 5.18 Comparison of fragility curves for 60% Model frame under FEMA-P695 ground-motion set and selected mainshocks record Set.....	119
Figure 5.19 Comparison of fragility curves for 50% Model frame under FEMA-P695 ground-motion set and selected mainshocks record Set.....	119
Figure 5.20 Comparison of fragility curves for 70% model frame under selected mainshocks record set and record set of mainshock-aftershock Sequences.....	121

Figure 5.21 Comparison of fragility curves for 60% model frame under selected mainshocks Record Set and record set of mainshock-aftershock Sequences .....	121
Figure 5.22 Comparison of fragility curves for 50% model frame under selected mainshocks record Set and record set of mainshock-aftershock sequences .....	122
Figure 5.23 (a) Structural response of 70% $M_{pb}$ model frame in terms of ‘top-story displacement’, (b) Spectrogram of the response with the tracked frequency of the structure and (c) Changing period of the structure and the mean elongated period .....	123
Figure 5.24 (a) Structural response of 60% $M_{pb}$ model frame in terms of ‘top-story displacement’, (b) Spectrogram of the response with the tracked frequency of the structure and (c) Changing period of the structure and the mean elongated period .....	124
Figure 5.25 (a) Structural response of 50% $M_{pb}$ model frame in terms of ‘top-story displacement’, (b) Spectrogram of the response with the tracked frequency of the structure and (c) Changing period of the structure and the mean elongated period .....	125
Figure 5.26 Elongated period and the respective connection capacity and the relationship between them for mainshocks at (a) spectral acceleration $S_a = 1g$ and (b) spectral acceleration $S_a$ $= 2g$ .....	126
Figure 5.27 Elongated period and the respective connection capacity and the relationship between them for aftershocks at (a) spectral acceleration $S_a = 1g$ and (b) spectral acceleration $S_a$ $= 2g$ .....	126

## CHAPTER 1. INTRODUCTION

### 1.1. Problem Statement

Moment-resisting steel frames are utilized routinely in low and mid-rise structures situated in high seismic regions because of their high strength and ductility. The poor performance of the beam-to-column welded connections of many steel frames, manifested in brittle fractures, in the 1994 Northridge and the 1995 Kobe earthquakes brought doubt to the suitability of using welded moment frames in high seismic regions. As a result, various research programs were initiated to assess the reason for brittle fracture in the connections [1] [2] [3] as well as to evaluate bolted connections as viable connection options under large earthquake demands [4] [5] [6] [7] [8].

Bolted connections, commonly known as semi rigid connections, are an appealing alternative to welded connections for many reasons. Frames with bolted connections exhibit relatively larger natural periods compared to their fully welded frames counterparts. As a result, the structure attracts lower magnitude of forces during earthquakes since they become displacement controlled. In addition, bolted connections are cheaper to fabricate, require less time to erect, and provide excellent and more reliable construction quality without the need for very skilled labors.

For moment frames in seismic regions, the ‘strong-column-weak-beam’ design approach is generally utilized in the U.S., which results in the development of plastic hinges in the beams away from the face of the columns to reduce the potential for brittle fracture of the connections. In the U.S., moment frames are used only in the perimeter of the entire structure and are designed to carry the lateral load developed due to the entire mass of the structure since the interior frames are

gravity frames that are featured with simple shear connections. The potential drawback of this approach is that local damages in the perimeter frames might give rise to eccentricities that could result in additional torsional actions that are otherwise not accounted for, increasing the potential for extensive damage and complete structural collapse [9]. Therefore, by distributing the moment frames across the structure' footprint and by using semi-rigid connections as energy dissipative elements, the greater part of the previously mentioned inadequacies can be mitigated, and the strong-column-weak-beam design approach avoided, resulting in more economical column sections. Previous studies on the seismic performance of semi-rigid frames [10] [11] [12] have demonstrated their stable and ductile hysteretic performance. In addition, it has been observed that the base shear of the frame increases with increase in connection stiffness. Therefore, an optimum system, using bolted connections, can be achieved to result in the least possible base shear with an acceptable level of lateral deformation [13].

As discussed previously, most of the seismic investigation of the steel frames are conducted using only mainshocks. However, according to various studies [14] [15] [16] [17] [18] [19] [20] [21], aftershock can cause more damage to a structure that is already deteriorated and damaged due to the mainshock. While most studies on mainshock-aftershock effects on frames have highlighted the importance of including aftershocks for assessing the seismic vulnerability of buildings, to the author's knowledge, none have been conducted on semi-rigid steel frames. In this thesis, the seismic performance of semi-rigid steel frames, subjected to real mainshock-aftershock ground motions is being thoroughly assessed.

## 1.2. Objectives and Scope of the Research

In this study three bolted moment resisting semi-rigid frames are designed and analyzed. The primary objective is to assess and compare the seismic behavior of the semi rigid frames with different connection capacities subjected to a suite of realistic mainshock-aftershock sequences, specifically, for the mainshocks, the record set given in ATC-63 [22] is used. Unlike previous studies, in this research the as-recorded real mainshocks and their respective aftershocks are used for the seismic assessment of the frames. Previous studies have synthesized the mainshock-aftershock sequences by using generalized Omori's law and Bath's law to predict the aftershock magnitude based on the magnitude of the respective mainshock. In this study the as-recorded real pairs of mainshock-aftershocks are utilized in the seismic analysis while appropriately scaling the aftershock in terms of 'peak ground acceleration' values using a relationship developed between the mainshock and aftershock sequences.

The seismic behavior has been accessed in terms of push-over curves, fragility curves and period elongation of the frames. To track the inelastic period of the frame, 'Short Term Fourier Transformation' (STFT) is used to transform hysteretic behavior of the frame in terms of 'top story drift' to obtain all the frequency and periods it consists of.

The aforementioned-objectives are realized using the tasks listed below:

- Task 1: Conduct critical appraisal of previous studies using a comprehensive literature review.
- Task 2: Develop finite element models of the frames of interest
  - Design the frames using local demand spectrum.
  - Design bolted connections – extended end plate connections – with different capacities.
  - Conduct all design checks in accordance to AISC 360-10.

- Develop 2D finite element models capable of capturing the inelastic behavior of the connections and the frames.
- Task 3: Conduct Pushover analysis
  - Calculate design base shear and lateral forces at each floor level.
  - Carry out the pushover analysis.
- Task 4: Conduct dynamic analysis and incremental dynamic analysis using the ground motion record set given by ATC-63 (FEMA-P965).
  - Evaluate the fundamental periods of the frames by Eigenvalue analysis.
  - Scale the records using the fundamental period of the individual frames obtained from the eigenvalue analysis.
  - Evaluate the results in terms of the fragility curves for all the three model frames.
- Task 5: New set of Ground-motion record set
  - Obtain mainshock and aftershock sequences from PEER-NGA Ground-motion database.
  - Establish a relationship between the PGA values of mainshock and the respective aftershock.
  - Propose a new set of ground motion record set from the downloaded MS-AS sequences which obey the relationship between the PGA values as established.
- Task 6: Conduct incremental dynamic analysis using only mainshocks of the new record set.
  - Scale the mainshocks of the record set using the fundamental period of the individual frames obtained from the eigenvalue analysis.
  - Evaluate the results in terms of the fragility curves for all the three model frames.

- Compare the fragility curves and the results with the results obtained from the standard set of ground-motions.
- Proceed if the fragility curves match.
- Task 7: Conduct incremental dynamic analysis using the whole sequence of mainshocks and respective aftershocks of the new record set.
  - Scale the aftershocks using the fundamental period of the individual frames obtained from the eigenvalue analysis.
  - Scale the mainshocks in relation to the respective aftershocks by using the relationship established in task 6.
  - Evaluate the results in terms of the fragility curves developed from the peak responses of the frames only in aftershocks.
  - Interpret the results by comparing the mainshock fragility curves and aftershock fragility curves.
- Task 8: Assess and develop an equation to quantify period elongation of the frame as a function of connection strength at a particular spectral intensity by using Short-Term-Fourier Analysis.

### **1.3. Organization of the Dissertation**

This dissertation includes 6 different chapters. Chapter 1 introduces the problem statement, objectives of the study and the organization of the dissertation. Chapter 2 discusses the previous studies, background and literature review in reference to the earthquake resistant design methodology and philosophy, existing moment-rotation curve models for semi-rigid connection, and studies pertaining to the effects of mainshock-aftershock sequences on system response and period elongation of structures. Chapter 3 describes the design of the frame and the extended end plate bolted connections and the moment rotation curves as well as the development of the 2D

finite element models. Chapter 4 focuses on the analysis methodologies including the static and dynamic analyses. Specifically, the chapter describes the approaches for performing pushover analysis, eigenvalue analysis, and dynamic time-history analysis. In Chapter 4, the procedure followed to select and scale the different sets of ground-motions is presented along with the approaches for conducting incremental dynamic analysis (IDA), developing fragility functions, and assessing period elongations of the frames. The results of all the analysis are presented in Chapter 5. This includes results from pushover analysis in terms of over-strength factor and ductility ratio, the IDA results for three different sets of ground-motions and their comparison in terms of median collapse capacity and standard deviation of the fragility curves, and the development and quantification of period elongation of the frame as a function of connection capacity. And the last chapter, chapter 6, summarizes the study and also talks about conclusions.

## CHAPTER 2. LITERATURE REVIEW AND BACKGROUND

### 2.1. Earthquake Design Philosophy

Variability and uncertainty in earthquake loading makes it difficult to design a structure for a specific scenario event. Typical variations in earthquake loading characteristics includes peak ground acceleration, duration, frequency content, and the return period. Structures are typically intended to withstand gravity loads acting vertically with sufficient margin of safety. When subjected to ground motions, a structure will be subjected to cyclic lateral loadings, which can cause serious damage as manifested by the strength and stiffness degradation of the structural elements – beams, columns, and connections. Because the loading is dynamic in nature, consideration should be given for designing specific elements to dissipate energy in a seismic event in the form of damping for example [23].

Generally, high seismic events occur with a very low probability of occurrence during the service life of the structure. If the structure is designed to resist such earthquakes elastically, it has to be designed considering an expensive lateral load resisting system which is neither economical nor feasible. Therefore, the design philosophy in such case is to accept a considerable level of damage without compromising life safety. Under moderate earthquakes, however, the notion of an elastic (or near elastic) design of structures is acceptable. Furthermore, serviceability is usually checked to ensure that the structure will not deflect or vibrate excessively during its service life. Structural assessment is typically performed considering ultimate strength limit state under the design earthquake (typically with return period of 475 years and probability of exceedance 10 %

in 50 years) and damage limitation under an occasional earthquake for the serviceability limit state (typically with return period of 72 years and probability of exceedance 50 % in 50 years). These two hazard levels are the most generally used worldwide. In certain norms (e.g., US guidelines (FEMA-750 2009), it is also specified that structures should be capable to withstand (i.e., to avoid global collapse) the so-called maximum considered earthquake (typically, having return period equal to 2,475 years and probability of exceedance 2 % in 50 years) [24].

In addition to the return period, the elastic stiffness and the yield strength of the material are the important properties to consider in seismic design. However, generally amid an extreme seismic activity, the structure is probably going to experience inelastic deformations and needs to depend on its hysteretic energy dissipation capacity and its ductility to dodge collapse.

In addition to the return period, ductility is another important design consideration. Ductility is defined as the ratio of yield displacement of the structure to the ultimate displacement. Ductile structures can undergo large plastic deformations without losing their strength due to either material inelasticity or geometric nonlinearity. The energy dissipated through the cyclic inelastic deformations of the structure is called the hysteretic energy. The hysteretic energy, generally, is given by the area under the cyclic load-deformation curve which is also known as hysteretic curve. While the apparent ductility of the structure might be acceptable under monotonic loading, under cyclic loading the structure may exhibit low energy dissipation capacity due to the ‘low-cycle fatigue effect’, which can be defined as the degradation of stiffness and strength of a structure due to inelastic cyclic loading.

## 2.2. Moment Resisting Curves for Semi Rigid Connections

The behavior of beam-to-column connections fall within three categories. These are generally defined as Fully-Restrained (FR) moment connections, Partially-Restrained (PR) connections, and Simple Shear Connections. By using beam line, it can be assessed whether the behavior of the connection is close to rigid or pinned i.e. fully-restrained or simple shear. Figure 2.1 shows that if the connection is able to resist at least 90% of the fixed end moment ( $M_F$ ), then it falls under the category of fully-restrained. On the other hand, as long as the connection is resisting not more than 20% of the fixed end moment, it can be classified as simple connection. Any other connection with resistance between these two extremes is classified under the category of partially-restrained connection.

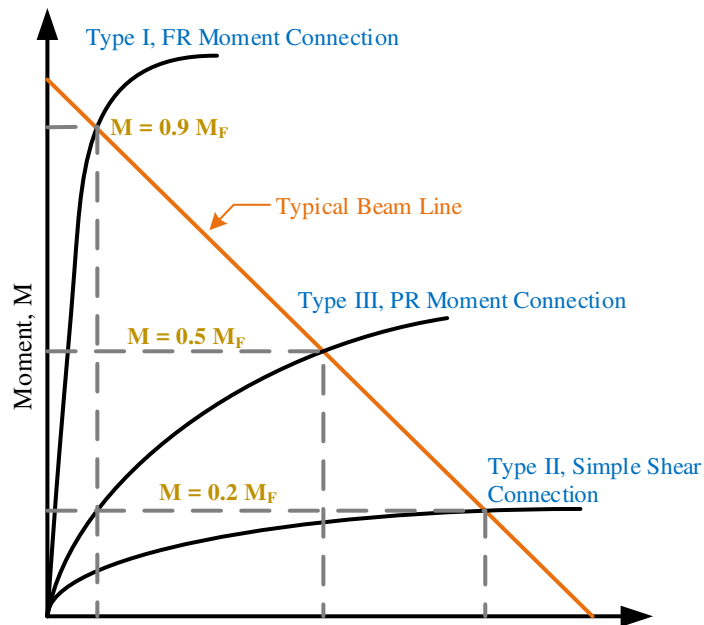


Figure 2.1 Connection classification based on moment rotation curve and beam line

An example of FR connections includes fully welded connections, T-stub connection, and connection with end-plate and column stiffeners. PR connections generally include bolted

connections such as extended-end-plate connection without columns stiffeners, flush-end-plate connection and also connection with top and seat angles with double web angles etc. Example of PR connections include connections with top and seat angles, connections with double web angles, among others.

The nonlinear attributes of a beam-to-column connection play a vital part in designing steel frames. For semi-rigid frames, some simplifications are made in analyzing and designing the connections which can cause erroneous results and misrepresentation of the connection behavior and overall structural response. It is very important to consider the true behavior of the steel connections, described by their moment-rotation curves, in order to analyze and design a steel structure. Various analysis strategies are suited for incorporating the behavior of the steel connections as semi-rigid connections, including for example moment distribution matrix stiffness method and slope deflection method.

As the connection deforms the stiffness matrix and force matrix gets updated in the force deformation relations. Therefore, it is necessary to incorporate the actual behavior of the connection in the mathematical relation (i.e. mathematical function) in the form of a moment rotation curve.

In 1975, a mathematical relationship was proposed by *Frye* and *Morris* [25]. The relationship was a polynomial function, which can be used to represent the moment rotation curve for seven different types of steel connections. These include end-plate connection with and without column stiffeners, T-stud, double web angle, top- and seat angle connection without double web angle, and single web angle. The polynomial function requires large number of experimental data and was developed as a function of size (dimensions) parameters. Experimental data were used to

evaluate the power component of the parameters, which ultimately play vital role in defining the behavior of the connection (Equation 2.1).

$$\theta = C_1(KM)^1 + C_2(KM)^3 + C_3(KM)^5$$

(Equation 2.1)

Where  $M$  is the moment acting on the connection,  $\theta$  is the rotation of the connection,  $C_1$ ,  $C_2$  and  $C_3$  are Curve fitting constants and  $K$  is a standardization parameter

*Picard and Giroux* [26] used the procedure given by *Frey and Morris* [25] and developed a polynomial moment rotation function for the connection between wide flange beams and tubular columns i.e. coped strap angle type connection. The function was developed for two different configurations, for width of the tube being equal to the width of the flange and for width of the beam less than that of the tube (Equation 2.2).

$$\phi = 1.04 * 10^{-5} (KM) - 1.62 * 10^{-11} (KM)^3 + 4.62 * 10^{-16} (KM)^5$$

(Equation 2.2)

Because of limited numbers of experiments, the *Frey and Morris* model may over estimate or under estimate the stiffness of the connection, particularly also that the effect of air gap between the beam and column section was not considered. Therefore, *Prabha* [27] developed a polynomial model by modifying *Frey and Morris* model and carried out FEM analysis for three configurations viz. No air gap, 7 mm air gap and 10 mm air gap (Equation 2.3).

$$\phi = 75.043(KM) - 1.583 * 10^3 (KM)^3 + 9.816 * 10^4 (KM)^5$$

(Equation 2.3)

Ramberg–Osgood function [28] is more widely used function to evaluate the stiffness of semi rigid joints. The function was initially developed for the nonlinear stress-strain relationship, but later was standardized by *Ang* and *Morris*, 1984 [29]. The modification was done so that the function can be used for five different types of connections (Equation 2.4).

$$\frac{\phi}{\phi_0} = \frac{KM}{[KM]_0} \left[ 1 + \left( \frac{KM}{[KM]_0} \right)^{n-1} \right]$$

(Equation 2.4)

Where  $KM$  is the moment,  $\phi$  is the rotation, and  $[KM]_0$ ,  $\phi_0$ , and  $n$  are the constants defining the shape of the standardization function.

In Eurocode 3 part 1-8, connections are classified based on their stiffness and strength. A connection is classified as fully-restrained, partially-restrained or pinned based on comparison of its rotational stiffness,  $S_{j,ini}$ , with the classification boundaries given in Figure 2.2, where zone 1 represents fully-restrained connection, zone 2 represents partially-restrained connection and zone 3 represents pinned connection.

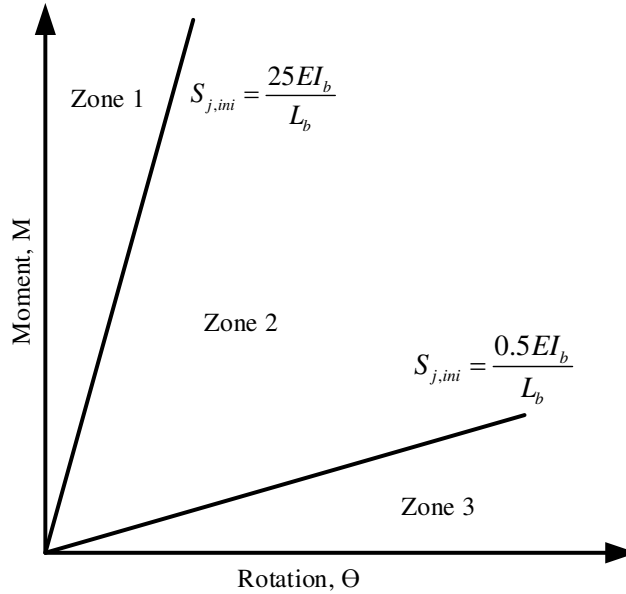


**Figure 2.2 Classifications of connections by stiffness in accordance with Eurocode 3**

According to Eurocode 3, the initial rotation stiffness of a connection,  $S_{j,ini}$ , should be obtained from the flexibility of its basic components. Stiffness of each component is considered in calculating the initial stiffness of the entire connection,  $S_{j,ini}$ . The initial rotational stiffness,  $S_{j,ini}$ , can be calculated from the following equation:

$$S_{j,ini} = \frac{Ez^2}{\mu \sum_i \frac{1}{k_i}}$$

(Equation 2.5)

Where,  $K_i$  is the stiffness coefficient of basic joint component  $i$ ,  $z$  is the lever arm and  $\mu$  is the stiffness ratio given by  $(S_{j,ini}/S_j)$ .

The design moment resistance of a beam-column connection,  $M_{j,rd}$ , with a bolted end plate can be calculated by following equation:

$$M_{j,Rd} = \sum_r h_r F_{tr,Rd}$$

(Equation 2.6)

Where,  $F_{tr,Rd}$  is the effective design tension resistance of bolt row  $r$ ,  $h_r$  is the distance of bolt row  $r$  to the center of compression and  $r$  is the bolt-row number.

To represent the behavior of the connection more accurately, a typical tri-linear elasto-plastic curve is used to model the elasto-plastic joint action. In which, a moment resisting curve is represented in three stiffnesses, of which  $K1$  is the initial stiffness as discussed above, and  $K3$  is equal to zero which represents the plastification of the connection, and the second stiffness,  $K2$ , is obtained as per to the figure given below:

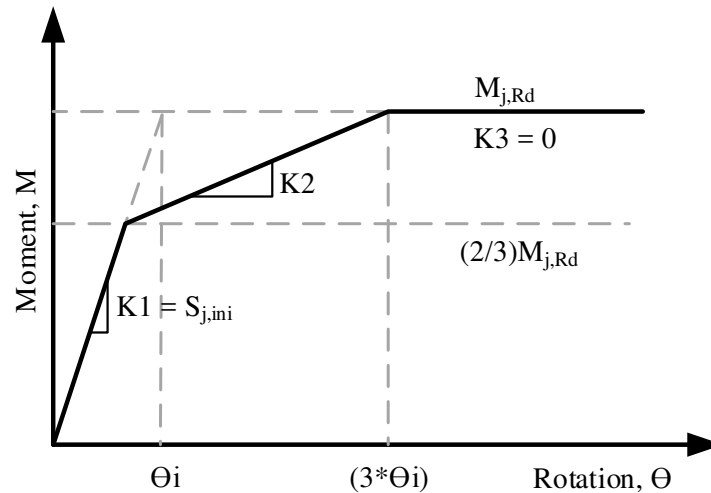


**Figure 2.3 Tri-linear elasto-plastic model for joint behavior**

*In this study, the moment resisting curves are calculated based on the specifications given in 'Eurocode 3 Part 1-8' and the detailed procedure of the same is described in APPENDIX A.*

### 2.3. Mainshock and Aftershock Relationship

While special cases do exist, it has been generally observed that an extensive shallow earthquake is trailed by numerous aftershocks. It is notable that earthquakes are emphatically correlated in time and space. A notable case of such relationship is aftershocks that are activated by the mainshock. The occasion reliance can be partially clarified by stress changes and auxiliary heterogeneity of the crust [30].

It has been observed that there is a proportionality between the logarithmic numbers of aftershocks occurring in a month after an expansive shallow earthquake to the logarithmic seismic moment of the mainshock. The corresponding constants for inter-plate and intra-plate earthquakes are unique, however this reflects a comparative contrast in scaling relations of the fault area to the seismic moment amongst inter-plate and intra-plate earthquakes. In this way, the key relationship can be inferred where the number of aftershocks corresponds to the fault zone of the mainshock. This is reliable with the speculation that aftershocks are produced by unbroken solid patches on the mainshock fault, if the patch density is consistent [31].

Consolidating this new outcome with the consequences of past investigations on aftershocks, it can be suggested that a rate of aftershock event can be calculated as shown in Equation 2.7( [31].

$$n(t)dt = \frac{kS10^{-bM_{th}}}{(t+c)^p} dt$$

(Equation 2.7)

Where  $n(t)$  is the number of aftershocks occurred in  $t$  days after the mainshock,  $S$  is the fault area of the Mainshock in  $\text{km}^2$ ,  $M_{th}$  is threshold magnitude,  $b$  is b-value of the Gutenberg-Richter

relationship.  $C$ ,  $P$  are the ‘c-’ and ‘p-’ values of the modified Omori formula and  $k = 13.4$  (for an inter-plate earthquake) and 31.7 to 63.5 (for an intra-plate earthquake)

Evidently the areal density of aftershocks on the fault plane is higher for an intra-plate earthquake than for an inter-plate earthquake. Advance examination of the outcomes proposes that the areal density of the aftershocks of a mainland intra-plate earthquake might be methodically higher than that of a maritime intra-plate earthquake. These distinctions may demonstrate some inherent contrast in the rupturing process among a mainland intra-plate, a maritime intra-plate, and an inter-plate events.

One critical experimental aspect of aftershock sequences was given by the Bath's law. The Bath's law states that the average difference between the magnitudes ( $\Delta M$ ) of the mainshock and its largest aftershock is always 1.2 autonomously [32].

Previous studies have confirmed Bath's law, with however extensive vacillations of  $\Delta M$  in the vicinity of 0 and 3 starting with one sequence then onto the next sequence [33]. Despite providing helpful data and information to understand the fault rupture, Bath's law is also significant in a communal point of view as one can form an idea about the magnitude of the possibly destructive aftershocks following the mainshocks. In the current study the focus is on two important values of an earthquake event - the difference between the magnitudes of the mainshock and that of the aftershock of the sequence and the seismic moment ratio of the moment ( $R$ ) released by the aftershock and the corresponding mainshock.

$$\Delta M = M_m - M_{a,\max}$$

(Equation 2.8)

In Figure 2.4, the magnitude difference between the mainshock and its largest aftershock from the same event is plotted versus the magnitude of the respective mainshock. The blue dotted line agrees the Bath's law, i.e.  $(m_m - m_{a,max} = 1.2)$ , while the data represents the results from the real catalog for various spatial cluster selection windows [34].

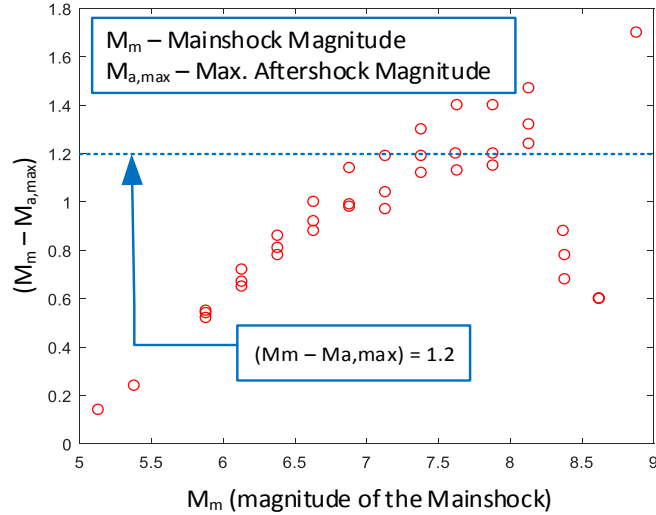


**Figure 2.4 Difference between the mainshock magnitude and magnitude of its largest aftershock versus the magnitude of the mainshock**

The  $\Delta M$  value cannot be directly considered in the presence of the background events, instead the effects of the background activities are taken into account by calculating the difference  $(M_a - M_f)$ , where  $M_f$  is the moment released before a mainshock event i.e. all the events that occurred before the mainshock and  $M_a$  is the moment released by the event after the mainshock.

$M_f$  and  $M_a$  are given as follows:

$$M_f = \sum_{i:t_i < t_m} M(m_i)$$

(Equation 2.9)

$$M_a = \sum_{i:t_i > t_m} M(m_i)$$

(Equation 2.10)

Where,  $t_m$  is the time of mainshock occurrence.

Therefore, the term  $(M_a - M_f)$  represents the relative difference between the excess of the after mainshock moment release and the moment released before the mainshock, noted that the before-mainshock events might also include the potential foreshocks. To estimate the seismic moment release before and after the mainshocks, the events are separated by using the time window  $[-T, 0]$  and  $[0, T]$  respectively, and the ratio  $R$  is given by following equation:

$$R = \frac{M_a - M_f}{M_m}$$

(Equation 2.11)

In view of the seismic moment ratio, the difference between the equivalent magnitudes can be estimated by using following equation [34].

$$\Delta m_{eff} = -\frac{\log_{10}(R_{corr})}{1.5} = m_m - m_{a,eff}$$

(Equation 2.12)

$$m_{a,eff} = \frac{\log_{10}[(M_a - M_f)C(m_m)] - 9.1}{1.5}$$

(Equation 2.13)

By using these equations, the effective magnitude can be used as a replacement for  $(M_{a,max})$  from the Bath's law (Equation 2.8), because in the effective magnitude the seismic moment

released by all the aftershocks are taken into account unlike  $M_{a,max}$  from the original Bath's law which only considers the moment released only by the largest aftershock of the ground-motion sequence.

#### 2.4. Simulation of mainshock-aftershock sequences

In the study of *Song et al.* [35], on the basis of the earthquake databases and ground motion models, a set of synthesized mainshock-aftershock sequences were generated. It has always been observed that the structural performance in an earthquake event is greatly affected by the variability in the seismic loading. A general far-field record set given by ATC-63 [22] was utilized to generate synthesized mainshock-aftershock sequences. The records set given in ATC-63 contains 44 ground-motion events with a lognormal distribution of the spectral acceleration of the earthquakes. Empirical ground motion models can be used to determine the median spectral acceleration and dispersion for the mainshocks and aftershocks.

Generally, empirical laws e.g. the Gutenberg–Richter law, Bath's law and Omori's law, which are well supported by real data and observations are used to determine the magnitude and occurrence time of the mainshocks and aftershocks. According to *Yin et al.* [36], the event of the mainshock is normally reproduced as a homogeneous Poisson process, while the aftershock event as a nonhomogeneous Poisson process.

Using the Gutenberg-Richter law [37], following equation gives the probability density function of earthquake magnitude (M).

$$f_M(m) = \frac{b \ln(10) 10^{-b(m-m_{\min})}}{1 - 10^{-b(m_{\max} - m_{\min})}}$$

(Equation 2.14)

Where  $m_{min}$  and  $m_{max}$  are the minimum and maximum magnitudes of the ground motions respectively at a particular region and  $b$  is the region-specific parameter.

The Omori's law and based on the modified Omori's law (Equation 2.15) the mean rate of aftershock occurrence can be calculated as:

$$\lambda(t) = \frac{10^{a+b(M_u-M_i)} - 10^a}{(t+c)^p}$$

(Equation 2.15)

Where  $M_u$  and  $M_i$  are the maximum and minimum magnitudes of the aftershocks respectively, of which  $M_u$  is generally the mainshock magnitude and the value of  $M_i$  is usually taken as M5.0 and  $\lambda(t)$  is the daily rate of the aftershock of which the magnitude is between  $M_u$  and  $M_i$ .

## 2.5. Effects of Mainshock-Aftershock Sequences on Steel Frames

In current seismic design codes of various countries, it is a provision to design a structure which is intended to act linear-elastically without undergoing any damage due only one earthquake [21]. However, recorded occasions show that the earthquakes, for the most part, occurring after mainshocks i.e. aftershocks, bring about the collective damage to the structures [20]. Aftershocks can possibly cause serious damage to structures, undermine life safety, and result in substantial economic losses even though the structure might have been only slightly damaged from the mainshock. For example, on August 11, 2012 an earthquake with moment magnitude M6.4 struck the upper east of Tabriz in East Azerbaijan and was followed by a severe aftershock of moment magnitude M6.3, eleven minutes after the mainshock. The mainshock– aftershock succession caused 327 deaths and more than 3000 injuries [38]. The immense Tohoku earthquake on March 11, 2011 in Japan, activated 60 aftershocks with M6.0 or more and three with M7.0. The aggregate

monetary losses in Japan was assessed at \$309 billion [35]. The M7.1 earthquake in Christchurch is another example where major mainshocks were activated reaching a magnitude of M6.3. This event caused 181 people to lose their life and resulted in approximately \$15 billion of repair costs [39]. Another example is the M8.8 Chile earthquake, which occurred on February 27, 2010. The event caused 304 aftershocks of M5.0 or more in the two months following the main shock and, causing an overall losses of approximately \$30 billion [40].

The aftershock magnitudes are typically less than that of the mainshock; however an aftershock record can possibly have a higher peak ground acceleration (PGA), longer duration, higher magnitude, and distinctive energy content than the mainshock [41]. Because of these reasons, aftershocks may result in larger seismic demand on a building. Structures weakened from the mainshocks have deteriorated structural properties and are more susceptible to damage from the aftershocks. The aftershock occurrence, which is space and time dependent, can be described by a non-stationary stochastic process. Generally, the event rate of aftershocks diminishes with time after the mainshock. The delay between the mainshock and biggest aftershock can extend between a few minutes to months [35]. Therefore, it is not a reasonable practice to instantly repair a building by the mainshock. It can take two years or longer to revive mainshock-damaged structures, depending on the extent of damage as a result of the aftershock magnitudes [42].

Approaches for generating the mainshock-aftershock earthquake sequences are generally separated into two groups: a) artificial sequence by randomized back-to-back approach and b) as-recorded sequences which can reflect the real characteristics of the mainshock and aftershock events. Both real and artificial sequences have been used in few studies to assess the impact of various seismic sequences on the response of single-degree-of-freedom (SDOF) and multiple-degree-of-freedom (MDOF) systems. *Yoshio and Anne* [19] assessed the seismic safety of a

concrete overpass under mainshock-aftershock seismic sequences, and found that the substantial magnitude of the aftershocks could cause noteworthy collective damage impact on structures. The mainshock-aftershock earthquake sequences consisted of the mainshock and the aftershock with the largest magnitude or two earthquakes with the largest and second largest magnitudes in the same earthquake event. Additionally, a numerical investigation of nine existing Mexican highway bridges under as-recorded mainshock-aftershock seismic sequences was completed by Ruiz-Garcia et al. [17] and it was observed that there was an increase in the peak lateral drift after the aftershocks than the mainshocks.

*Mahin* [18] investigated the response of nonlinear SDOF systems, which were subjected to mainshock– aftershock sequences representing the 1972 Managua seismic event. The study showed an increase in the displacement ductility demand of the elastoplastic systems at the end of aftershock than that of the mainshock.

*George and Asterios* [16] examined the inelastic response of eight RC structures which were subjected to five as recorded seismic sequences, recorded at a same station, in a same bearing and in a brief timeframe, within three days. In such cases, the primary observation was a critical damage accumulation because of the multiple earthquakes.

*Li and Ellingwood* [15] examined the response and damage state of two steel moment resisting model frames by subjecting them to artificial seismic sequences and by scaling the mainshock by a factor obtained from aftershock data from Eureka, California. It was established that the cumulative damage relied upon the period shift of the structure because of the damage due to the mainshock and also on the frequency characteristics of the aftershock event.

*Ruiz-Garcia and Juan* [14] investigated the response of the structure subjected to artificial sequences, which were based on back-to-back, randomized approach and also the as-recorded sequences. It was observed that the artificial sequences lead to an overestimation of the residual drift demands and the maximum lateral drift peak when compared to results from the as-recorded sequences. In addition, the investigation using as-recorded earthquake sequences, revealed that the frequency content of the mainshock and the aftershock with the highest magnitude are weakly correlated. The randomized approach dismissed the diverse attributes of the mainshock and aftershock sequences, however it can to some degree reflects the response and the damage state of the structures under aftershock.

Be that as it may, the seismic events of the mainshock-aftershock earthquake are entirely subjected to site conditions. In addition, sequential real events introduce distinctive attributes, making the examination more complex to perform, and a probabilistic approach is required to take care of the issue. Currently, no studies have been carried out specifically on semi-rigid steel moment-resisting frames subjected to as-recorded earthquake sequences. As discussed above, the cumulative damage of a structure depends on the period shift resulting from damage to the mainshock. To fill this gap, in this thesis three semi-rigid moment frames with different fundamental periods are studied and their performance is evaluated by subjecting them to as-recorded mainshock-aftershock sequences and assessing the fragility functions and period elongation in the structures.

## **2.6. Period Elongation**

Generally, steel moment frames soften due to their nonlinear responses during ground-motions, causing deterioration of the stiffness post yield deformations. The softening of the structure is

manifested by elongation in its fundamental period, which is often described by the secant or the tangent stiffness of the structure.

Spectral acceleration of ground-motions generally decreases as the period increases, therefore, the elongation of the period of the structure can be a beneficial phenomenon as it will reduce the seismic excitation as the period elongates.

While there has been some confirmation of the degree of period elongation from perceptions of structures damaged by the earthquakes, there is restricted data on the connection between the degree of period elongation and the intensity of seismic ground motion.

A study by *Heidebrecht and Naumoski* [43], investigated the performance of a medium height reinforced concrete frames under strong seismic ground motions. The objectives were to show how the fundamental period of the frame under study increases with the intensity of the ground motions it and development of a relationship between the ground-motion intensity and the elongated fundamental period of the structure. The observations included the fundamental period of the frame right after the end of the ground motion. A more recent study by *Mahmoud* [8] evaluated the inelastic period of the structures by using ‘Fourier Transformations’, which is a process of decomposing a signal into its constituting oscillatory functions.

## **2.6.1. Formulas for Fundamental Period**

### **2.6.1.1. Code Specified Formulas**

Evaluation of the fundamental period of the structure and providing a simple formula to estimate the period appeared in ACT3-06 [44] and was established using the following assumptions:

- Inter-drift of the structure at each story level is the same i.e. the displacements of the structure is governed by drift limitation.
- The static lateral forces are distributed uniformly/linearly along the height of the structure.
- Seismic base shear is proportional to  $1/T^{2/3}$

As specified in the U.S. building codes and guidelines (e.g. ATC3-06 [44], UBC-97 [45] and NEHRP-94 [46]), the empirical formula for the natural period of moment resisting frames is given as follows

$$T = C_t H^{3/4}$$

(Equation 2.16)

Where, H is the height of the structure (ft) above ground and  $C_t$  is a numerical coefficient equal to 0.035 for moment resisting steel frames and 0.030 for reinforced concrete frames.

An alternative formulation for a 12-storey or less building was given in NEHRP-94 [46] as shown below

$$T = 0.1 N$$

(Equation 2.17)

Where, N is the number of stories.

*Housner and Brady* [47] utilized the Rayleigh method to estimate the fundamental period of a given structure with equal floor masses and heights as follows

$$T = C_1 \sqrt{H}$$

(Equation 2.18)

Where, the numerical values of  $C_1$  generally relies on the stiff properties and the height of the structures.

*Goel and Chopra* [48] developed another formula to estimate the fundamental period using the Rayleigh's method as shown below:

$$T = C_3 H^{1/(2-\gamma)}$$

(Equation 2.19)

Where,  $\gamma = 2/3$ .

### **2.6.2. Signal Processing**

The previous discussion on estimating the fundamental period of the structure is limited to the elastic period. Another way of investigating the vibration period of the structure that is independent from the structural state (being elastic or inelastic) is to analyze the displacement response history of the structure. The top-story displacement of the structure is treated as a signal and is decomposed into the periods/frequencies that it is made up of, so that the frequency or frequencies of vibrations can be evaluated. The main motive of the signal processing is to assess the primary information from the signal by transforming it. These transformations can be characterized as either time or frequency time– recurrence domain based calculations. There are various techniques and methodologies that can be utilize for signal processing, as shown in Figure 2.5 [49].

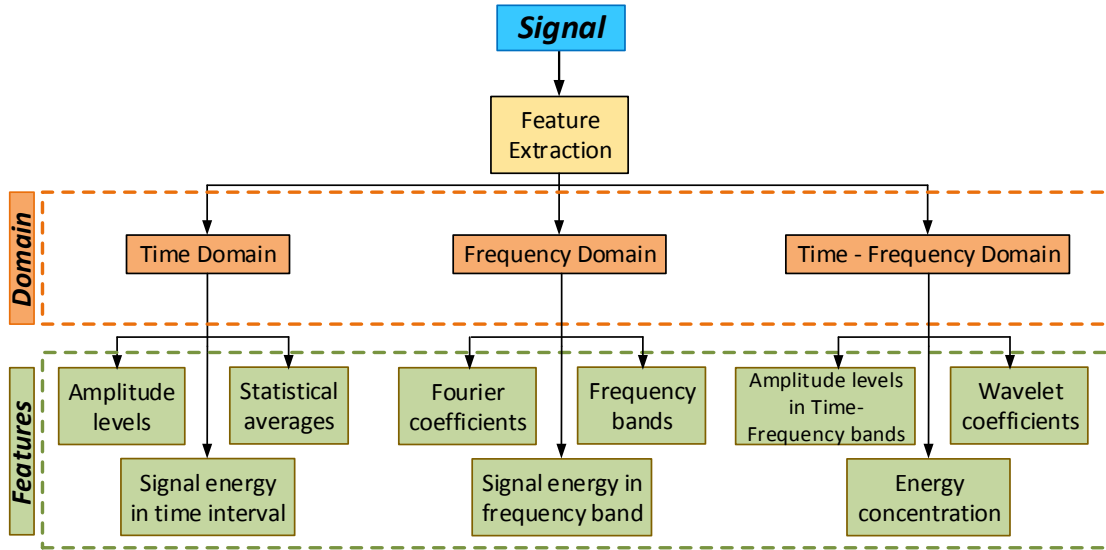


**Figure 2.5 Pattern Classification for Signal Processing**

As per *Oppenheim and Schaffer* [50], the standards of signal processing can be found in the traditional numerical investigation strategies of the seventeenth century. In 1822, Joseph Fourier noted that functions can always be rewritten as infinite sum of harmonics [51]. Differential equations, recurrence relation, transform theory, time-frequency analysis and spectral estimation are some of the mathematical methods used to process the signal and assess the underlying information. Following are some categories of signal processing:

- Analog Signal Processing – This category of signal processing is for the analog signals i.e. signals which are not digitized.
- Continuous-time Signal Processing – In this category, the signal which vary with the varying continuous domain.
- Discrete-time Signal processing – This category is for sampled signals, i.e. signals sampled at discrete points in time and are quantized in time and not in magnitude.

## CHAPTER 3. MODEL DESCRIPTION & DESIGN

In low-rise and mid-rise structures, located in high seismic areas, generally moment resisting-steel-frames are used. In the U.S., the general practice is to use ‘strong-column-weak-beam’ (SCWB) approach to design the exterior frames which are the lateral load resisting systems. The use of SCWB approach is to allow plastic hinges to develop in the beams away from the columns to prevent their potential damage. However, one of the disadvantage of the ‘SCWB’ approach is that it results in very large column sizes, which causes overdesign in low-mid-rise buildings [13].

Since oversized columns are only used in the perimeter lateral load resisting frame, the economic burden that results from using them is arguably marginal. That being said, another major drawback of such approach is the lack of redistribution capacity in the structure which hinder the full realization of the ductility of steel structures in general. To alleviate this problem, moment resisting frames can be modeled with energy dissipative zones, which are the connections, leading to a column sizes that are merely stronger than the connections (i.e. smaller columns). Another benefit of utilizing this approach is that all frames in the entire 3-D structure participate in resisting the lateral load, which reduces the  $P-\Delta$  demand on a given frame. Moreover, by making use of bolted connections, field erection time is reduced.

### 3.1. Description of the Building

In this study, a simple three-stories, three-bay building is designed and studied. The building is assumed to be a typical office building, situated in southern California. There are two types of frames considered in the building - moment resisting frames in the E-W direction and braced

frames in the N-S direction. The braced frames have span length of 9 meters and moment resisting frames have span length of 7 meters. The story heights are chosen to be 4.2 meters for the first floor and 3.6 meters for the remaining two floors. A typical plan and elevation of the building is shown in Figure 3.1 below [13]. The behavior of the structure in the E-W direction (only moment resisting frames) is assessed in this study. A total of four moment resisting frames are used in the building that are all similar and all frames are designed to be lateral load resistant. Therefore, all of the structure's weight is distributed to all moment resisting frames. For this study, only one interior frame is considered. The considered frame is designed for three cases where end-plate connection with capacities of 70%, 60% and 50% of the plastic moment capacity of the respective beams are used.

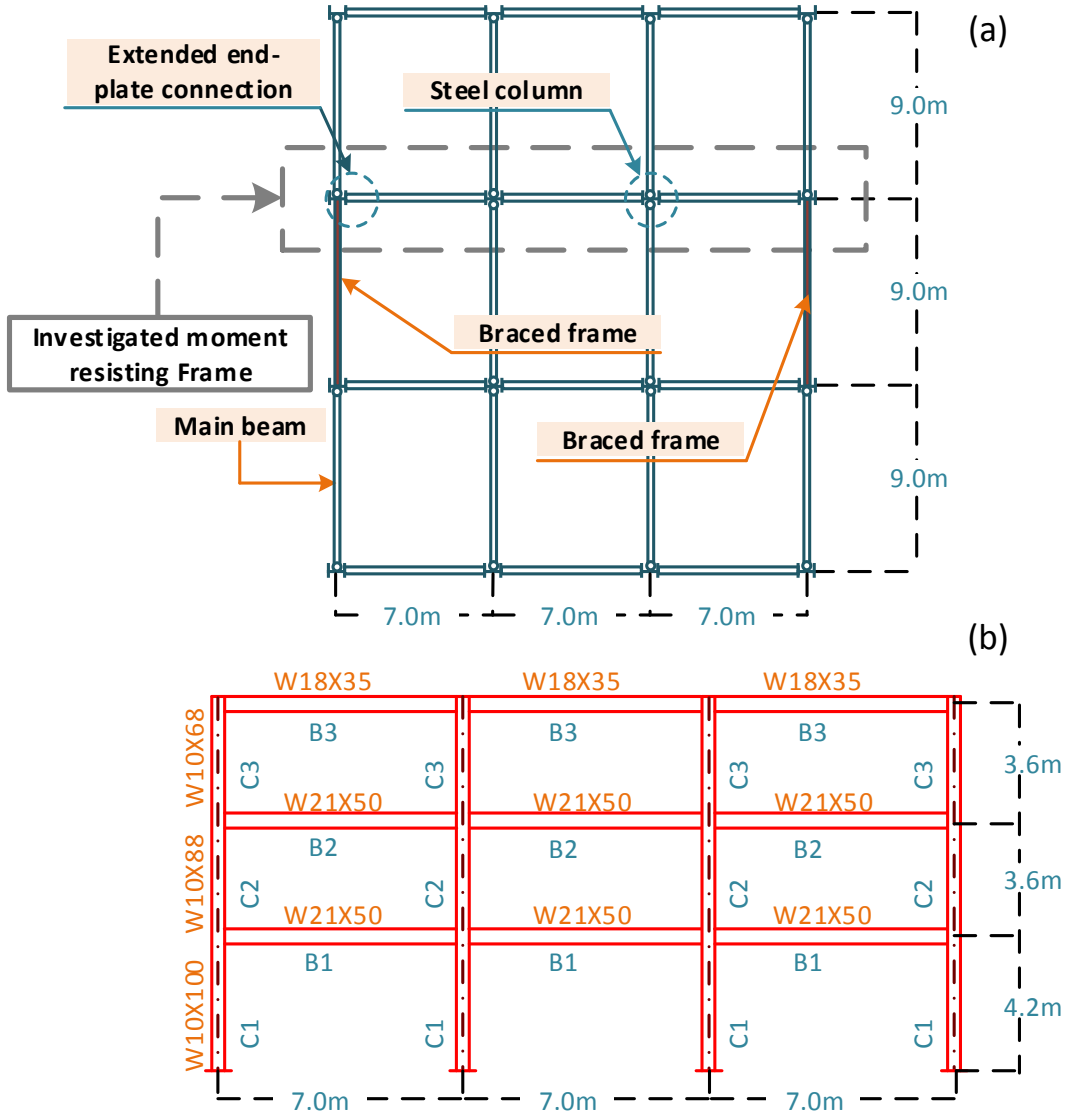


Figure 3.1: (a) Plan view and (b) Elevation view of the sample building

### 3.2. Loads and Load Combinations

All loads acting on the structure are determined per ASCE 7-05 [52] and IBC 2006. For gravity loads, a dead load of  $3.2 \text{ KN/m}^2$  is considered. This includes self-weight of the structure, electrical and mechanical equipment. Same gravity loads are applied to each floor and to the roof. Live load is  $1 \text{ KN/m}^2$  for the roof and  $3.8 \text{ KN/m}^2$  for the floors. This includes weight of the partition walls as

well. For design purpose, a load combination of  $1.2D + 1.6L$  is used, but for seismic analysis a load combination of  $1.2D+0.5L$  is considered.

### **3.3. Seismic Constants**

#### **3.3.1. Site Class**

The site class is categorized as Site Class A, B, C, D, E or F as per Chapter 20 of ASCE 7 [52]. Where the soil properties are not known in adequate detail to decide the site class, Site Class D should be utilized unless the building official or geotechnical information decides Site Class E or soils are available at the site [53].

#### **3.3.2. Seismic Design Category and Importance factor**

Risk categories of structures and different buildings are presented in IBC Table 1604.5. Importance factors,  $I_e$ , are in ASCE 7-05 Table 1.5-2 [52]. Structures with Risk Category I, II or III that are found where the mapped spectral response acceleration parameter at 1s period is more than or equal to 0.75 should be allocated to Seismic Design Category E. For the structures with Risk Category IV that with mapped spectral response acceleration parameter at 1s period more than or equal to 0.75, fall under Design Category F. Every other structure may be assigned a seismic design category in view of their occupancy category and the design spectral response acceleration parameters,  $S_{DS}$  and  $S_{D1}$ , decided per Section 1613.3.4 or the site-specific techniques of ASCE 7 [52]. Each building and structure should be relegated to the more serious seismic design category as per Table 1613.3.5(1) or 1613.5.5(2) of ASCE 7, independent of the fundamental period of vibration [53].

The building studied in this thesis, is a typical office building with importance factor 1 and occupancy category II. The soil category on which the building is supposed to be constructed is considered as D. Table 3.1 summarizes all the seismic constants considered in the study. The seismic loads are calculated and applied to the system according to the equivalent lateral force procedure explained in *ASCE 7-05* [52].

**Table 3.1 Seismic Constants Considered in the study**

<b>Seismic Constant</b>	<b>Value</b>
Importance Factor	1
Occupancy Category	II
Soil Category	D
Short Period Parameter	1.5 g
1 Sec period Parameter	0.60

### **3.4. Materials and Modelling**

#### **3.4.1. Materials**

The structural steel considered in this study is A992 ( $F_y = 345 \text{ N/mm}^2$ ) for beams and columns. A36 Gr 36 for end plates ( $F_y = 250 \text{ N/mm}^2$ ) and ASTM A490 for the bolts in the semi-rigid connections. For beams and columns, bilinear elasto-plastic model with kinematic-strain hardening equal to 0.01 is considered as shown in Figure 3.2.

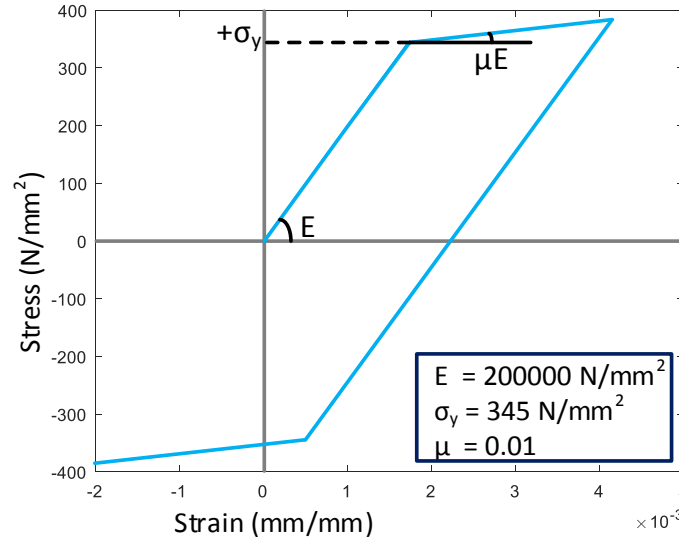


**Figure 3.2 Bilinear elasto-plastic material model**

### 3.4.2. Analytical Model

ZEUS-NL, which is a general-purpose finite element software, is used to carry out the pushover and dynamic analysis. ZEUS-NL is developed at Mid-America Earthquake Center (MAE) at the University of Illinois at Urbana-Champaign. This analysis program uses a layered ‘fiber’ approach which accounts for the spread of inelasticity along the member length and section depth. Additionally ZEUS-NL is configured to capture substantial displacements of the structure and individual members by forcing equilibrium in the deformed state [54] (i.e. geometric nonlinearity).

In the current study, a 2D finite element model is employed. The model includes 204 nodes and 400 elements and comprises of 1D beam and column elements. The connections in the model are introduced using springs connecting the ends of the line elements that represent the beam and column (Figure 3.3). Each spring is modelled with the ‘Zero Length Joint Elements’. The properties of the connections (i.e. springs) are specified in the form of a moment-rotation (action-deformation) curves as noted in detail in section 3.10.1.

Figure 3.3 (a) shows the configuration of the beam and column elements along with the rotational springs. Figure 3.3 (b) shows an idealized moment-rotation curve with stiffness degradation, which is employed as a rotational behavior of the so-called SMTR and HFC spring models in ZEUS-NL to represent the behavior of a connection. While the HFC spring model in ZEUS-NL is used to represent the behavior of the connection. The values describing the moment rotation curves in all three frames are essentially different.

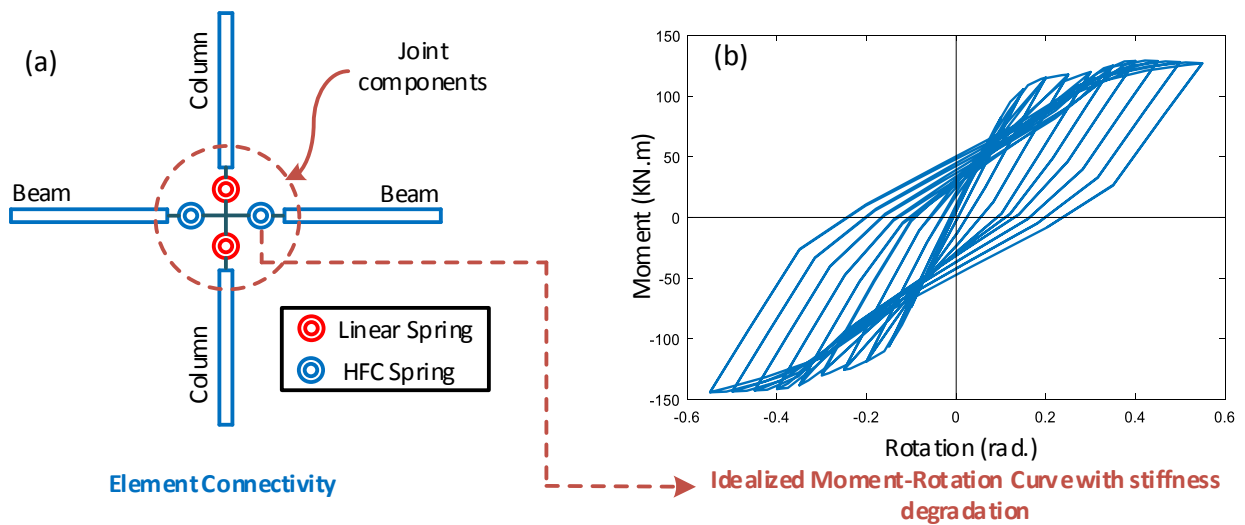


**Figure 3.3 (a) Configuration of the beam and column elements along with the rotational springs, (b) Idealized moment-rotation curve with stiffness degradation**

### 3.5. Design Procedure

The structure in this study is a low-rise long span building with end-plate connections that are classified as semi-rigid/partial strength acting as energy dissipative zones. The frames in the E-W direction are moment-resisting. However, since all frames in the frame resist the lateral load, the ‘Strong-column-weak-beam’ concept approach is avoided. The frame used in this study is the same the one in ‘Aksoylar, Elnashai, & Mahmoud, 2011’ [13]. Table 3.2 shows the details for the

sections used in the frame. AISC 360-10 [54] is used to evaluate the possible limit states in the frame including.

**Table 3.2 Beams and Columns sections**

	<b>Beam Sections</b>			<b>Column Sections</b>		
<b>Connection Capacity (%)</b>	<b>Third Story</b>	<b>Second Story</b>	<b>First Story</b>	<b>Third Story</b>	<b>Second Story</b>	<b>First Story</b>
70	W18X35	W21X50	W21X50	W10X68	W10X88	W10X100
60	W18X35	W21X50	W21X50	W10X68	W10X77	W10X88
50	W18X35	W21X50	W21X50	W10X68	W10X68	W10X77

### 3.6. Connection Design Assumptions

Although the frames were designed in [13], detailed on the connections including their configuration, dimension, bolts arrangement, etc., were not readily available. Therefore, it was decided that the connections should be designed for the purpose of conducting this study. This is also important so that the parameters for the SMTR and HFC springs, used to describe the moment-rotation behavior of the connections, can be defined in the finite element model. The connections should be designed considering the distribution of the internal forces and moments in the components. As per ‘Eurocode 3: Design of steel structures - Part 1-8: Design of Joints’ [55]. The following assumptions were used to evaluate the distribution of forces:

- a) The internal forces and moments are in equilibrium with the applied forces and moments to the joints,

- b) Each element in the joint is capable of resisting the internal forces and moments,
- c) The deformations resulting from this distribution do not exceed the deformation capacity of the fasteners or welds and the connected parts,
- d) The assumed distribution of internal forces shall be realistic with regard to relative stiffnesses within the joint,
- e) The deformations assumed in any design model based on elastic-plastic analysis are based on rigid body rotations and/or in-plane deformations which are physically possible, and
- f) Any model used is in compliance with previous test results.

### **3.7. Global Analysis**

1. The impacts of the behavior of joints on the distribution of internal forces and moments inside a structure, and on the general deformations of the structure, ought to, for the most part, be considered. This will depend on the extent of the impact of the joint on the behavior.
2. Joints models are generally characterized into 3 simplified categories to ascertain whether the effects of joint behavior should be considered in the analysis or not. This includes
  - Simple joint - moments are not transferred through the joint;
  - Continuous joint - joint behavior does not have any effect on analysis;
  - Semi-continuous - joint behavior should be taken into account in the analysis.
3. The suitable kind of joint model must to be determined from Table 3.3, contingent upon the characterization of the joint and on the chosen method of analysis [55].

**Table 3.3: Type of Joint Model after [55]**

<b>Method of global Analysis</b>	<b>Classification of joint</b>		
Elastic	Nominally pinned	Rigid	Semi-rigid
Rigid-Plastic	Nominally pinned	Full-strength	Partial-strength
Elastic-Plastic	Nominally pinned	Rigid and full-strength	Semi-rigid and partial-strength
			Semi-rigid and full-strength
			Rigid and partial-strength
Type of joint model	Simple	Continuous	Semi-continuous

### 3.8. Structural Properties of the joints

#### 3.8.1. Design moment-rotation characteristics

As shown in Figure 3.4(a), a joint is represented by a rotational spring at the intersection of the centerlines of the associated members, for a single sided beam-to-column joint. The properties of the spring are in the form of a design moment-rotation that depicts the behavior of the connection between the bending moment ' $M_{j,Ed}$ ' at a joint and the corresponding rotation ' $\theta_{Ed}$ ' between the associated members. The design moment-rotation characteristic is non-linear as shown in Figure 3.4(b).

A moment-rotation curve, see Figure 3.4 (b), should define the following three main structural properties:

1. Rotational stiffness;

2. Moment resistance;
3. Rotation capacity.

The assumptions made in the global analysis and the assumptions made in the design of the members (EN 1993-1-1) [55], should be consistent with the design moment-rotation characteristics. The design moment-rotation characteristic of a joint should depend on the properties of its basic components. The basic components with the corresponding behavioral features of the connection are defined in Figure 3.5.

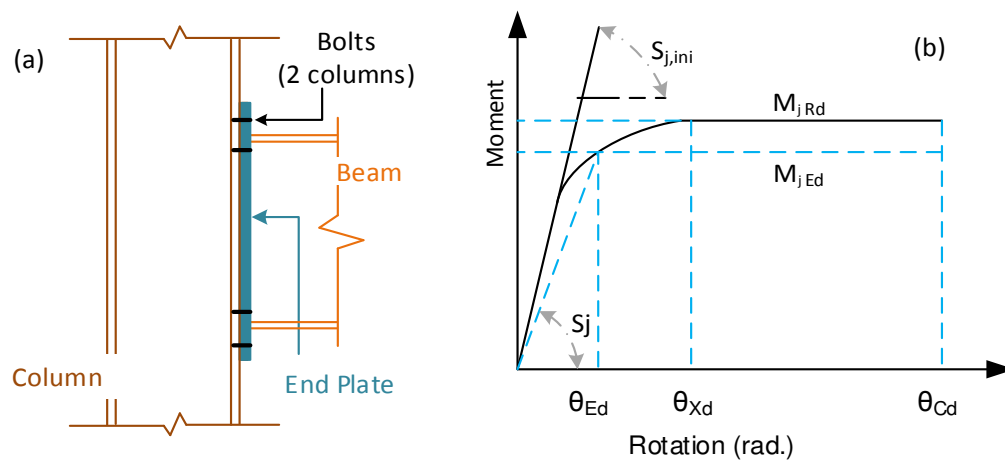


**Figure 3.4 (a) Schematic of an end-plate connection, (b) Design moment-rotation characteristic for a joint: after [55]**

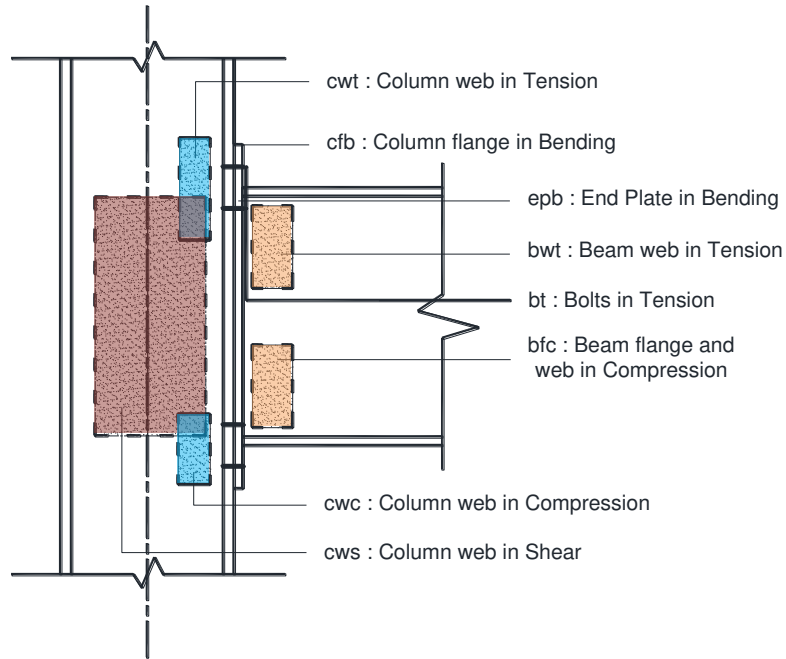


**Figure 3.5 : Components of connection behavior: *after* [13]**

It is worth noting that as per the clause 9.2a and 9.6 in AISC 341-05 [56], the requirements for designing the frame with semi-rigid energy dissipative connections are violated, therefore disobeying the SCWB principle, the columns are designed merely to stronger than the connections. In other words, the connection capacities are used in SCWB principle instead of beam capacities [13].

**Table 3.4 : Plastic Capacities of beam sections and Connection Moment Capacities**

Beam	W18X35	W21X50	W21X50
	Third Story	Second Story	First Story
$M_{pb}$ (kN-m)	375.1	622.2	622.2
$70\%M_{pb}$ (kN-m)	255.9	434.3	434.3
$60\%M_{pb}$ (kN-m)	230.1	365.9	365.9
$50\%M_{pb}$ (kN-m)	172.8	320	320

The semi-rigid connections are designed as ‘Extended End Plate Connections’ with four bolts in compression and four in tension with no stiffeners (Figure 3.4). The reason for selecting the ‘Extended End Plate’ type is that this type of connection can be designed as full-strength as well as partial-strength whereas for example ‘top & seat angle’ type of connections cannot reach the full connected beam moment capacity.

### 3.9. Connection Design procedure

‘Eurocode 3: Design of Steel Structures 1 – 8: Design of joints’ [55] is followed to design the connections for this study. For detailed procedure and design steps, please see ‘APPENDIX A: Steel Connection Design’ in this thesis.

The ‘Thin plate design procedure’ is followed to concentrate the failure within connection. This design procedure results in the behavior being governed by considerable yield in the end plate, or bolt rupture, causing the connection to fail well before the respective beam or column. To prevent brittle failure in the connection and to obtain sufficient inelastic rotation capacity, all requirements from ‘Eurocode 3: Design of steel structures - Part 1-8: Design of joints’ [55] were fulfilled. The connections were designed in such a way that either of the following control the moment resistance: End plate in bending, Column Web panel in shear or the Column Flange in bending. In addition, to avoid the bolts to fail and further concentrating the failure of the connection within the end-plate, following condition (Equation 3.1) is used per ‘Eurocode 3’:

$$t \leq 0.36d \sqrt{\frac{f_{ub}}{f_y}}$$

(Equation 3.1)

Where,  $f_{ub}$  is the ultimate tensile strength of the bolts and  $f_y$  is the yield strength of the end-plate.

### 3.9.1. Configuration Details

Details such as materials used for the end plate and bolts, configuration of the connection (end-plate thickness, bolt diameters etc.) for two beams are given the Table 3.5 and Table 3.6. For more details on connection topologies, such as internal bolt distances, please refer to APPENDIX A.

**Table 3.5 : Connection configuration details for beam W21X50**

<b>Beam W21X50</b>			
	<b>70% Conn Capacity</b>	<b>60% Conn Capacity</b>	<b>50% Conn Capacity</b>
<b>End Plate</b>			
Material	Grade A36	Grade A36	Grade A36
Thickness	20 mm	20 mm	20 mm
Top Extension	76.2 mm	80 mm	83 mm
Bottom Extension	76.2 mm	80 mm	83 mm
Left Extension	18 mm	12.7 mm	12.6 mm
Right Extension	18 mm	12.7 mm	12.6 mm
Width	201.862 mm	191.262 mm	191.06 mm
Height	680.72 mm	688.32 mm	694.32 mm
<b>Bolts</b>			
Material	A490N	A490N	A490N
Bolt Diameter	25.4 mm	22 mm	20 mm

Bolts per row	2	2	2
# of Tension Bolts	4	4	4
# of Comp Bolts	4	4	4

**Table 3.6: Connection configuration details for beam W18X35**

<b>Beam W18X35</b>			
	<b>70% Conn Capacity</b>	<b>60% Conn Capacity</b>	<b>50% Conn Capacity</b>
<b>End Plate</b>			
Material	Grade A36	Grade A36	Grade A36
Thickness	20 mm	20 mm	15 mm
Top Extension	85 mm	90 mm	80 mm
Bottom Extension	85 mm	90 mm	80 mm
Left Extension	12.7 mm	12.6 mm	12.6 mm
Right Extension	12.7 mm	12.6 mm	12.6 mm
Width	177.80 mm	177.60 mm	177.60 mm
Height	619.58 mm	629.58 mm	609.58 mm
<b>Bolts</b>			
Material	A490N	A490N	A490N
Bolt Diameter	20 mm	19.05 mm	16 mm

Bolts per row	2	2	2
# of Tension Bolts	4	4	4
# of Comp Bolts	4	4	4

### 3.9.2. Initial Rotational Stiffness

As per the design of the subject frame, there are two beam sections (one for the 1<sup>st</sup> and 2<sup>nd</sup> story and other for the 3<sup>rd</sup> story, Table 3.2). ‘Component Based Method’ is used to determine the initial stiffness of the connections (see Table 3.7 for details). For extended end plate, the controlling components, which affect the connection behavior, are as follows:

- Column web in tension
- Column flange in bending
- End plate in bending
- Beam web in tension
- Bolts in tension
- Beam flange and web in compression
- Column web in compression
- Column web in shear

**Table 3.7 : Connection initial stiffness**

<b>Connection initial stiffness (KN-m/rad)</b>			
<b>Connection Capacity (%)</b>	<b>Third Story</b>	<b>Second Story</b>	<b>First Story</b>

70	61,825	118,908	118,908
60	59,455	104,151	104,151
50	56,981	89,561	89,561

### 3.9.3. Moment-Rotation Curve

The moment-rotation curves shown in Figure 3.6 are the result of the previously discussed design process. For further details on the procedure, please see ‘APPENDIX A: Steel Connection Design.

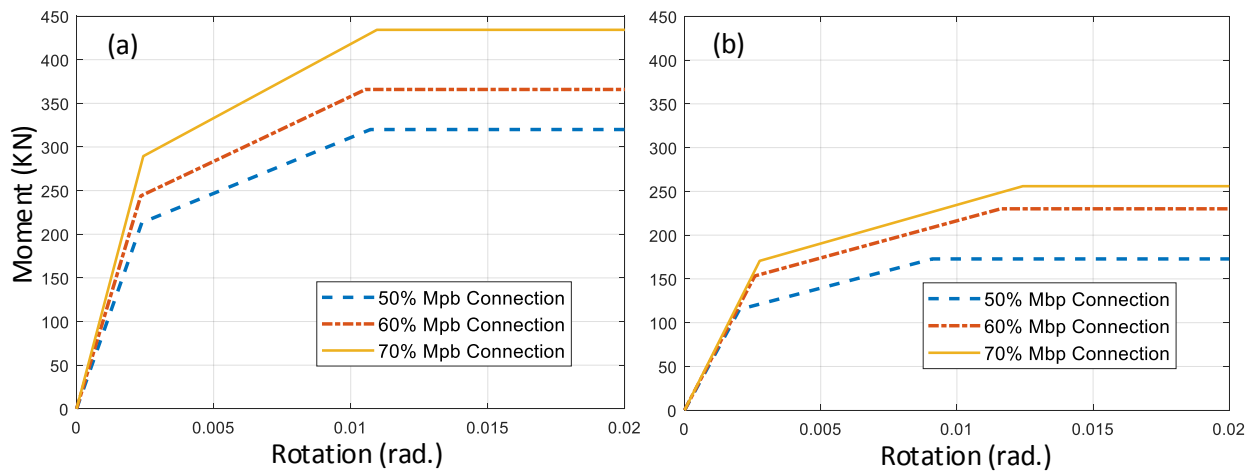


**Figure 3.6 (a) Moment-rotation curve for connection to beam W21X50, (b) Moment-rotation curve for connection to beam W18X35**

### 3.10. Modeling Approach

The analysis of the sample frames is carried out in ‘ZEUS-NL’ [57]. This program provides an easy and efficient way to run accurate nonlinear analysis on two-dimensional and three-dimensional steel or reinforced concrete structure. Element class: ‘Joint Element’ is used model the Extended End Plate Connections in the sample frames.

### 3.10.1. Joint Element

Three-dimensional joint element with uncoupled axial, shear and moment actions can be used to model pin joints, inclined supports, Elasto-plastic joint behavior, soil-structure interaction and structural gaps. To define a joint element, four nodes are required (as shown in Figure 3.7).

- Node number 1 & 2 are the structural joints, and since the joint element is a zero-length element, nodes 1 & 2 must initially be coincident.
- Node number 3 can be either structural or non-structural, and is used to define the X-axis of the joint.
- Node number 4 is a non-structural node, and is used to define the X-Y plane along with the already defined X axis.

The orientation of the X-axis, after the deformation, is determined by its initial orientation of the X-axis and global rotation of node number 1. Since, node 1 & 2 are initially coincident, the element has zero length. The joint element cannot be used to model coupled axial, coupled shear and coupled moment action. To manage the behavior of the joint, the ‘force-displacement’ or ‘moment-rotation’ characteristics for the axial force  $F_x$ , the shear forces  $F_y$  and  $F_z$ , and the moments  $M_x$ ,  $M_y$  and  $M_z$ , there are predefined curves in ‘ZEUS-NL’ libraries. Each curve requires few input parameters to define the curve and they should be given in the order:

$$F_x - F_y - F_z - M_x - M_y - M_z$$

Six curves have to be defined for the 6 DOF of the joint ( $F_x$ ,  $F_y$ ,  $F_z$ ,  $M_x$ ,  $M_y$ ,  $M_z$ ). There are currently seven curve types in ZEUS-NL libraries, out of which SMTR and HFC Curve has been implemented [57].

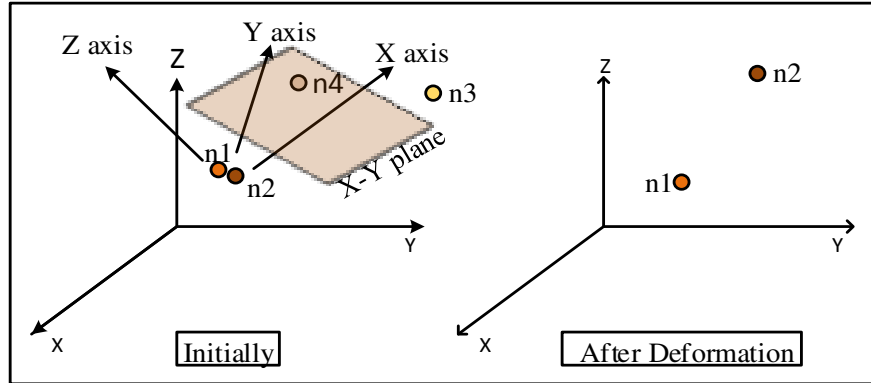


Figure 3.7 : Joint element configuration

### 3.10.2. Modeling

To configure a joint element, node 1 and node 2 are the end points of the column and the beam, respectively. Except from those, node 3 and 4, which are non-structural nodes are used to define the local axes of the joint element. See Figure 3.8 for more details.

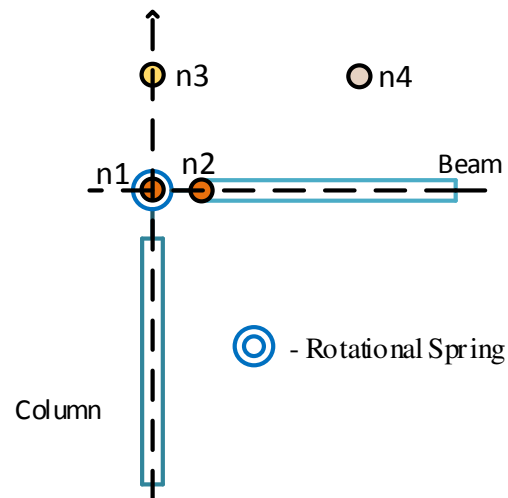


Figure 3.8 : Joint element modelling

An elasto-plastic model with symmetric bilinear curve and kinematic hardening is used to model the connection in this study. All semi-rigid connections are represented as a rotational spring for each connection zone (Scissors Model), see Figure 3.3 (b).

The response of the structure under earthquake loads is significantly governed by the cyclic behavior of the connections. Therefore, the cyclic behavior is modelled with two types of hysteretic models [13]:

- Symmetric Trilinear elasto-plastic Model with kinematic hardening (SMTR)
- Hysteretic Flexure Model under constant axial force (HFC)

### **3.10.3. SMTR Model**

In this model, there is no pinching and no stiffness degradation. Therefore, the model can be used to represent the behavior of the extended end plate connections.

In addition to requiring an accurate model of the connection as load is applied, it is necessary to have a model for unloading and reloading if a detailed analysis of a semi-rigid frame is to be carried out.

The normal assumption is that a connection loads along the moment rotation curve and unloads linearly with a slope equal to the initial slope of the curve [58]. In Figure 3.9, it can be easily seen that the stiffness during unloading is approximately equal to the initial stiffness of the moment rotation curve (no stiffness degradation).

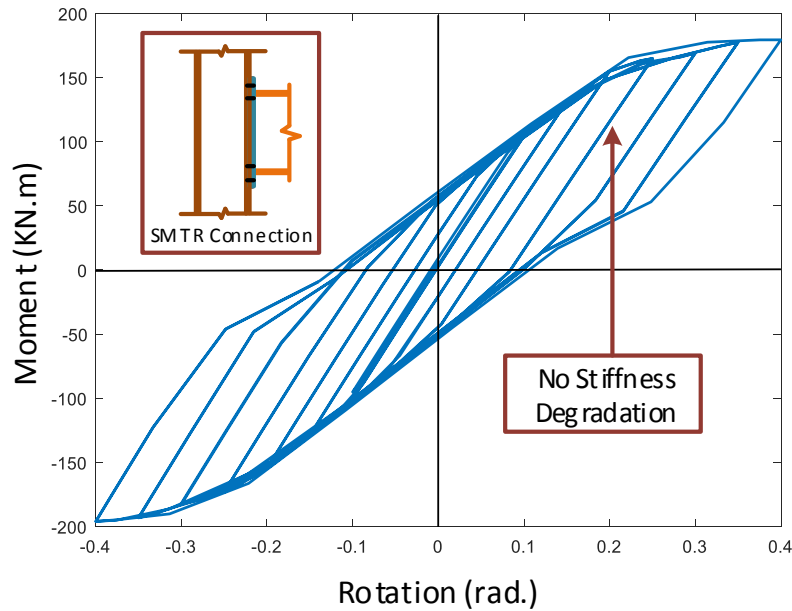


**Figure 3.9 : SMTR hysteretic model**

#### **3.10.4. HFC Model**

The main assumption for this hysteretic flexure model is that under cyclic loading, the connection loses its stiffness where observable degradation can be seen in the cyclic behavior.

Unlike the SMTR model, the connection loads along the moment rotation curve, but unloads at stiffness less than the initial stiffness. In Figure 3.10, it can be seen that the unloading stiffness continues to reduce as the connection undergoes more cycles. Eventually the stiffness of the connection is less than the initial stiffness.

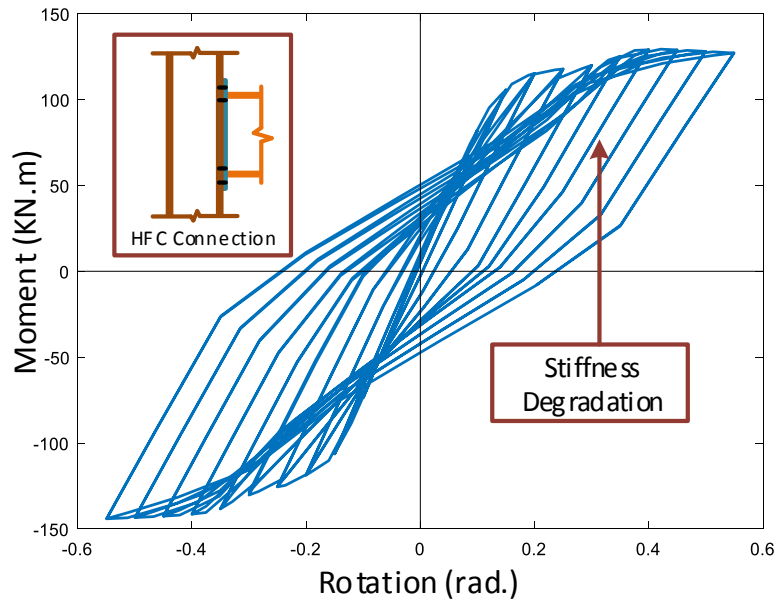


**Figure 3.10 : HFC hysteretic model**

## CHAPTER 4. METHODOLOGY

Recently it has been documented that there should be some changes in the approaches defined in the codes for the seismic design, which are based on the linear elastic behavior of the structure. Non-linear time-history analyses are way too more complex for every day design use. Therefore, to evaluate the performance of the structure, non-linear static analysis is carried out, also known as ‘Pushover Analysis’. In this analysis, the structural behavior is observed under a monotonically increasing lateral load applied on each floor [59].

### 4.1. Pushover Analysis

Pushover is conducted, using predetermined lateral forces, so that particular response parameters can be quantified. These parameters, observed at a predefined deformation level, include ‘global drift’, ‘inter-story drift’, ‘deformations between elements and components’, ‘inelastic element deformation’, ‘connection forces’.

#### 4.1.1. Base Shear Calculation

Lateral forces are the horizontal forces that are made to act on the structure externally, to observe its behavior as the forces increase. Lateral forces are applied on the structure along with the gravity forces (dead and live loads), and are increased monotonically by the scale-factor keeping the forces at the same ratio, until the structure reaches the limit state. To calculate the lateral loads at each story, first ‘Base Shear’ is calculated. In this study Seismic Base Shear is calculated as per *IBC 2006* [60] and *ASCE 7-05* specifications [52].

#### 4.1.1.1. Design Response Spectrum

The maximum considered earthquake (MCE) parameters, the mapped MCE spectral response acceleration at short periods ( $S_s$ ) and the mapped MCE spectral response acceleration at period of 1 second  $S_1$  are determined in accordance with section 11.4.1 from *ASCE 7-05* [52]. Short-period ( $T = 0.2$  sec) and one-second-period parameters are taken as 1.5g and 0.6g respectively.

$$S_s = 1.5g \text{ at } T = 0.2 \text{ seconds (short-period parameter)}$$

$$S_1 = 0.6g \text{ at } T = 1 \text{ second (one-second-parameter)}$$

The estimations of  $S_s$  and  $S_1$  are utilized to create the coefficient  $S_{DS}$  and  $S_{D1}$ , which are then used to construct the response spectrum. The strength is evaluated utilizing the  $S_{DS}$  value since it is higher than the  $S_{D1}$ . Note that one could utilize the  $S_{DS}$  and  $S_{D1}$  that depend on genuine estimations of  $S_s$  and  $S_1$  as contradict to the estimations of 1.5g and 0.6g. In case of Design Earthquake Spectral Response Acceleration parameters at short period ( $S_{DS}$ ) and at period of 1 second ( $S_{D1}$ ) shall be evaluated from the equations 11.4-3 and 11.4-4 from *ASCE 7-05* [52] respectively.

$$S_{DS} = (2/3) S_{MS} = (2/3) * F_a * S_s = 1.0g$$

$$S_{D1} = (2/3) S_{M1} = (2/3) * F_v * S_1 = 0.6g$$

Where  $F_a$  and  $F_v$  are site coefficients used to adjust maximum considered earthquake (MCE) spectral response acceleration parameters (Table 11.4-1 and 11.4-2 from *ASCE 7-05* [52]). The design response spectrum is shown in Figure 4.1 and is built considering the following specifications:

- For periods less than  $T_o$ , the design spectral response acceleration  $S_a$  is calculated as follows:

$$S_a = S_{DS} (0.4 + 0.6 \frac{T}{T_0})$$

- For periods greater than or equal to  $T_0$  and less than or equal to  $T_s$ , the design spectral response acceleration,  $S_a$ , shall be taken equal to  $S_{DS}$ .
- For periods greater than  $T_s$  and less than or equal to  $T_L$  the design spectral response acceleration,  $S_a$ , shall be taken as:

$$S_a = S_{D1}/T$$

- For periods greater than  $T_L$ ,  $S_a$  shall be taken as:

$$S_a = S_{D1} * T_L / T^2$$

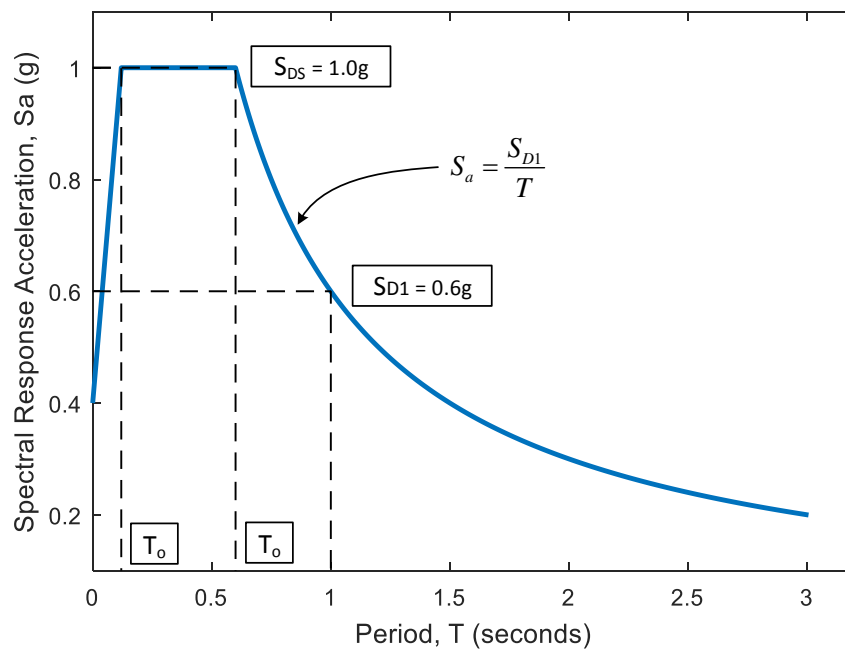


**Figure 4.1 Design response spectrum**

By considering the specifications given in *IBC 2012* and *ASCE 7-10* [53], base shear is calculated and is given in Table 4.1.

**Table 4.1 Calculated Design Base Shear**

<b>Connection Capacity (%)</b>	<b>Base Shear (KN)</b>
70	141.76
60	137.09
50	133.93

**4.1.1.2. Distribution of Lateral Forces**

Lateral loads are applied to represent the inertia force, signifying the 1<sup>st</sup> mode of vibration, at the floor (height). For this, a ‘Triangular Load Distribution’ is utilized (Figure 4.2) to distribute the base shear along the height. The distribution of the lateral load along the height is determined using story height and total weight of the floor, which is summarized in Table 4.2.

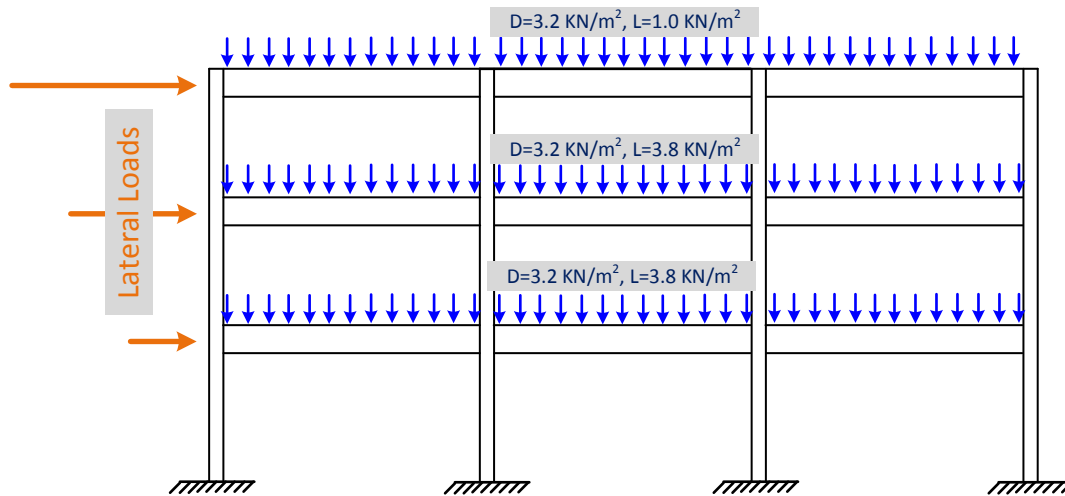


**Figure 4.2 Lateral loads distribution**

**Table 4.2 Floor heights and weights**

<b>Floor</b>	<b>Height</b>	<b>Weight (KN)</b>
3rd Floor	3.6	318.96
2nd Floor	3.6	421.83
1st Floor	4.2	421.83

The base shear is distributed along the height of the structure (at the floor level) in the ratio of the product of the weight of the floor and the total height of the structure until that floor to the sum of the product. Following are the tables for the detailed calculations of the Lateral forces.

**Table 4.3 Lateral load distribution for the model frames**

<b>Connection Capacity = 70%</b>	<b>Floor</b>	<b>W<sub>x</sub> (KN)</b>	<b>h<sub>x</sub> (m)</b>	<b>W<sub>x</sub>.h<sub>x</sub></b>		<b>Lateral Forces (KN)</b>
	3	318.96	11.4	3636.14	0.418	59.262
2	421.83	7.8	3290.27	0.378	53.625	
1	421.83	4.2	1771.69	0.203	28.875	
Total	1162.62		8698.1	1	141.764	
<b>Connection Capacity = 60%</b>	<b>Floor</b>	<b>W<sub>x</sub> (KN)</b>	<b>h<sub>x</sub> (m)</b>	<b>W<sub>x</sub>.h<sub>x</sub></b>		<b>Lateral Forces (KN)</b>
	3	318.96	11.4	3636.14	0.418	57.31
2	421.83	7.8	3290.27	0.378	51.859	
1	421.83	4.2	1771.69	0.203	27.924	
Total	1162.62		8698.1	1	137.094	

Connection Capacity = 50%	Floor	W <sub>x</sub> (KN)	h <sub>x</sub> (m)	Lateral		
				W <sub>x</sub> h <sub>x</sub>	Forces (KN)	
	3	318.96	11.4	3636.14	0.418	55.99
	2	421.83	7.8	3290.27	0.378	50.664
	1	421.83	4.2	1771.69	0.203	27.28
	Total	1162.62		8698.1	1	133.936

#### 4.1.2. Target Displacement

Target displacement represents the global displacement of the structure under the design earthquake corresponding to a specific performance level. Global drift, inter-story drift, inelastic element deformation, deformation between elements and components are few of the important performance parameters. The capacities and demands of these performance parameters play significant role in the evaluation of the lateral load resisting system, and depend upon the performance level to be evaluated.

In this study, the performance parameter considered is ‘Inter-story Drift’. The limit state ‘Complete Collapse’ is ‘8% of inter-story drift based on *Hazus - MH 2.1* [61],. The total height of the structure is 11.4 meters. Therefore, the analysis is performed up to a drift limit that is equal to 8% of the total height i.e. 0.912 meters [62].

#### 4.1.3. Design Parameters

Estimations of the system over-strength factor and deflection amplification factor for seismic-force resisting frames are depicted in Table 12.2-1 of *ASCE/SEI 7-05* [52] . The seismic

performance of the model frames is evaluated and compared by calculating the following design parameters as shown in Figure 4.3 [63].

### **Initial Stiffness**

The term ‘Initial Stiffness’ represents the stiffness of the entire structure if it remained entirely linearly elastic. From the pushover analysis, the initial stiffness is described by the load versus deformation curve, prior to apparent yielding in the structure.

### **Over-strength Factor**

The over-strength factor is the ratio of the maximum strength of the structure ( $V_{\max}$ ) to the design base shear of the structure ( $V_d$ ), defined as shown below.

$$\Omega_0 = \frac{V_{\max}}{V_d}$$

*(Equation 4.1)*

### **Ductility Ratio**

Ductility Ratio is defined as the ratio of the total displacement of the structure to the displacement at the elastic limit i.e. the ratio of the ultimate displacement to the yield displacement.

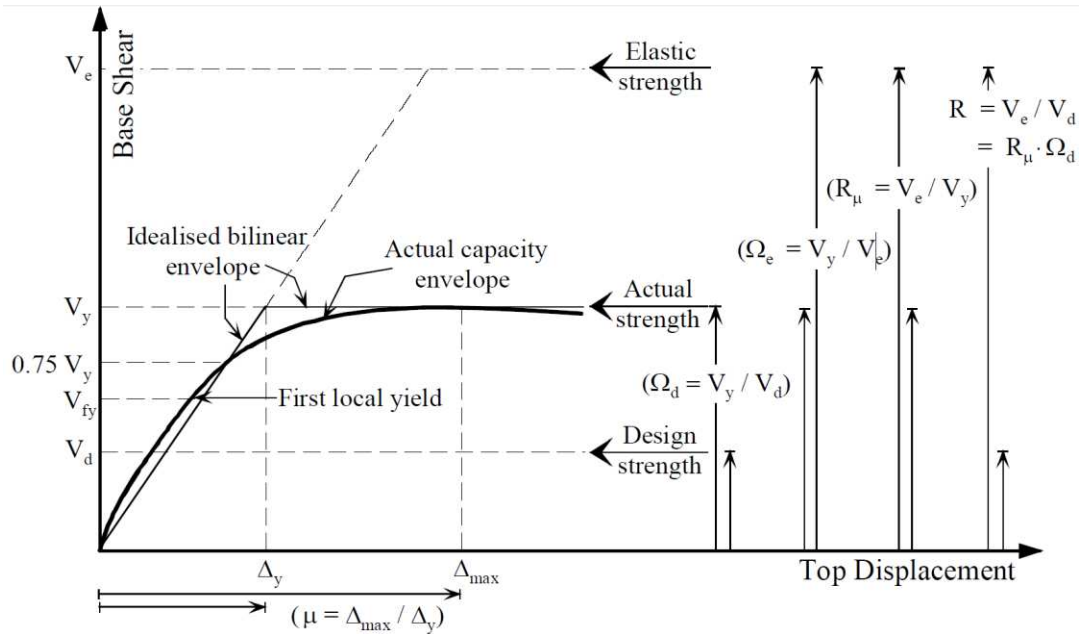


Figure 4.3 Relationship between strength, over-strength and ductility ratio: *after* [63]

#### 4.1.4. Limitations

It must be emphasized that the pushover analysis is based on static loading and is approximate in nature. Therefore, the dynamic response of the structure cannot be calculated using pushover analysis. Being static, the pushover analysis will most likely be unable to foresee the inelastic response of the structure in light of the invariant or adaptive static load patterns, particularly when higher mode effects become noticeably vital as the fundamental period of the structure tend to elongate under large demands.

There are many incentives to advocate the utilization of ‘Inelastic Pushover Analysis’ for response predictions. It provides substantially more important data than ‘Elastic Static’ analysis, yet it is counterproductive to advocate this strategy as a general solution approach for all cases. While pushover analysis is a helpful approach to employ for evaluating inelastic strength and deformation capacity, it cannot be relied upon for uncovering design weakness [62].

## 4.2. Eigenvalue Analysis

Prior to conducting dynamic analysis, it is important to determine the natural frequencies and mode shapes of the structure. There are many reasons to calculate the fundamental frequencies and mode shapes of a structure. One reason is to assess the dynamic interaction between a component and its supporting structure. For example, if a structure has a moving component attached to it and has almost the same fundamental frequency as the structure, it can result in resonance and can lead to extensive performance amplifications and substantial structural damage.

Dynamic analysis such as frequency response, response spectrum analysis and transient response are very much based on the fundamental frequency and mode shapes of the structure. In addition, the eigenvalue analysis results i.e. fundamental frequency and mode shapes can be used in modal transient response analysis and modal frequency analysis. The important modes can be calculated and can be used to figure out the optimum frequency steps to integrate the equations of the motion.

By using fundamental frequency and mode shapes, design changes can also be evaluated. For example, in this study, 3 frames with different connection capacities and ultimately different stiffness are studied. It can be easily observed that as the stiffness of the structure decreases, its fundamental frequency decreases. So, by eigenvalue analysis, we can determine if any particular design change is affecting the dynamic response of the structure.

In some cases, the results from the dynamic analysis has to be compared with the physical results. Therefore, to gather the physical results, eigenvalue analysis results are very helpful. For example, normal mode analysis results can be used to find the best location to attach accelerometers, and the data collected from it can be linked to the dynamic analysis results.

In conclusion, there are number of reasons to go for eigenvalue analysis and calculate the mode shapes and fundamental frequencies of the structure. It can be said that the eigenvalue analysis is beginning of the many types of dynamic analysis. Moreover, to predict and control the behavior of the structure, one must have the complete knowledge of the mode shapes and the fundamental frequencies of the particular structure.

#### **4.3. Dynamic Time History Analysis**

The time-history analysis is a well-ordered, step by step analysis of the dynamic response of the structure where the loading at each time step may vary. To predict the force and deformation response of the various structural components, inelastic time-history analysis is the most accurate method.

To carry out the time history analysis, cyclic load-deformation properties and careful consideration of deterioration characteristics are required. Producing meaningful results from dynamic time-history analysis, careful selection and scaling of earthquake records and the utilization of a suitable integration scheme for time stepping is required. Zeus-NL has two integration schemes – The Newmark integration (default) and the Hilber-Huges-Taylor integration scheme. In this study the Newmark method is utilized with  $\beta = 0.25$  and  $\gamma = 0.5$ .

#### **4.4. Dynamic Analysis using Zeus-NL**

Zeus Nonlinear (Zeus-NL) gives a simple and productive approach to run precise nonlinear dynamic time-history, traditional and adaptive pushover, and eigenvalue analysis. Dissimilar to other comparative design and analysis software, dynamic examination is currently a matter of fundamental straightforward steps, utilizing a totally visual approach. This implies the client can

make an auxiliary model just by point-n-snap and afterward let the program deal with all the investigation subtle elements [57].

Zeus-NL can be utilized to anticipate the vast displacement conduct of plane and space frames under dynamic loading, considering both geometric and material nonlinear conduct. Concrete and steel material models are accessible, together with a huge library of 3D elements that can be utilized with a wide decision of various sections of concrete, predefined steel material and composite section arrangements. The loading can be steady or variable accelerations, forces or displacements [57].

The loading is usually applied at the supports of the structure, and typically is ‘acceleration’ record (in spite of the fact that the forces can also be used instead of acceleration). Asynchronous and synchronous excitations can be used. The integration algorithms used are Huges-Taylor or Newmark integration technique [57].

The analytical model for dynamic analysis is not the same as the one used in pushover analysis. In the ‘dynamic-time-history’ module, the following elements have to be added in order to perform the dynamic analysis (see Figure 4.4).

- Mass elements to represent inertial forces when the model is coupled with the acceleration (earthquake record)
- Damping elements to represent damping forces acting on the structure when it is going through oscillations due to dynamic loads.
- Time-acceleration values (earthquake record) in the format of a text file.

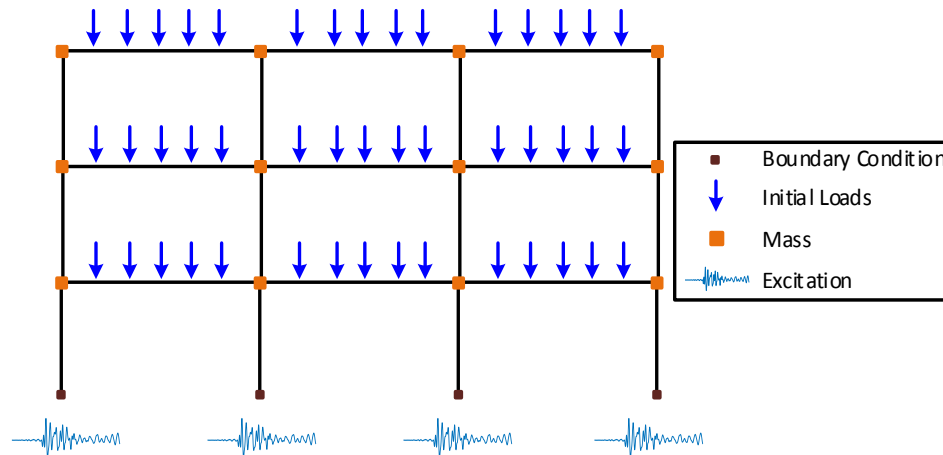


**Figure 4.4 Configuration for dynamic analysis**

#### **4.4.1. Applied loading**

##### **Mass**

‘Lumped mass element (concentrated)’ is been used to model the masses in the structures. The distributed loads acting on the beams is converted into mass elements and assigned them to the ends of each beam along with the distributed loads. The analytical model for dynamic analysis consists of lumped masses assigned on each beam-column intersection. To assign masses, the forces are divided by the acceleration ( $g = 9810 \text{ mm/sec}^2$ ), so the unit of mass used in the model is  $N/(mm/sec^2)$ .

##### **Initial loads**

These are static loads which are assigned before any variable or dynamic load. The can either be displacements or forces applied at the nodes. Initial loads are generally assigned to represent the self-weight, dead load or live loads acting on the structure and in negative Y-direction (acting downward). The initial loads can be applied in the form of distributed loads or point loads as per the user’s requirements.

## Dynamic loads

In this study, the dynamic loads are ‘accelerations’ and are in the units of gravitational acceleration (i.e. ‘g’). Therefore, the scaling factor used in this study is a multiple of ‘g’ i.e. 9810 mm/sec<sup>2</sup>.

## Input format

The finite element program requires that the time and acceleration values be in text format (\*.txt). The column numbers are specified for time and acceleration values, as well as the first and the last line of the sequence. If the acceleration values are in the terms of g (g = 9810 mm/sec<sup>2</sup>), then the scaling factor required is 9810. The time values should be in ascending order.

### 4.4.2. Damping

Structural damping is a measure of energy dissipation in a vibrating structure. The damping limit is defined as the proportion of the energy dispersed in one cycle of oscillation to the most maximum measure of energy. Rayleigh Damping is also known as ‘Mass and Stiffness Proportional Damping’. The undamped modes or established ordinary modes uncouple the equation of motion (equation 4.4) and fulfill an orthogonality relationship over the mass and stiffness matrices. Considering the dynamic system, the equation is given by:

$$[M]\left(\frac{d^2x}{dt^2}\right) + [C]\left(\frac{dx}{dt}\right) + [K](x(t)) = F_{stat} + F_{dyn}$$

(Equation 4.2)

Where:

$X(t)$  = displacement as a function of time

$[M]$  = the mass matrix

$[C]$  = the damping matrix

$[K]$  = the stiffness matrix

In case of Rayleigh damping,  $[C]$  is determined as follows –

$$C = \eta M + \delta K$$

*(Equation 4.3)*

Where  $\eta$  is the mass-proportional damping ( $\alpha_1$ ) and  $\delta$  is the stiffness proportional damping ( $\alpha_2$ ),  $[K]$  is the stiffness matrix of the structure is linear and represents the initial stiffness of the structure. Therefore,  $[C]$  consists of both the mass proportional term and a stiffness proportional term as well.

Relationships between the modal equations and orthogonality conditions allow (Equation 4.3) to be rewritten as:

$$\xi_i = \frac{1}{2\omega_n} \eta + \frac{\omega_n}{2} \delta$$

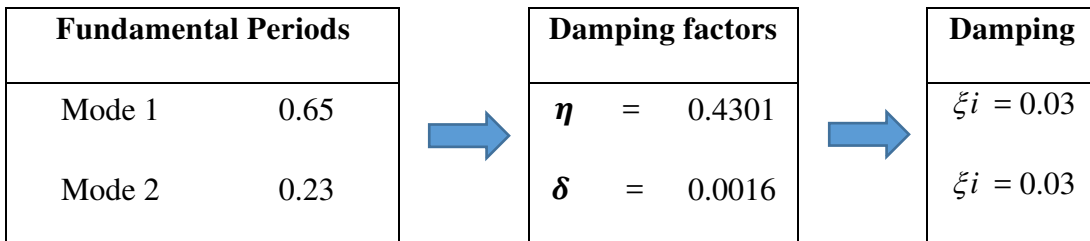
*(Equation 4.4)*

Where  $\xi_i$  is the critical damping ratio equal to 3% i.e. 0.03,  $\omega_n$  is the natural frequency for mode ( $n$ ) where  $\omega_n = 2\pi f_n$ .

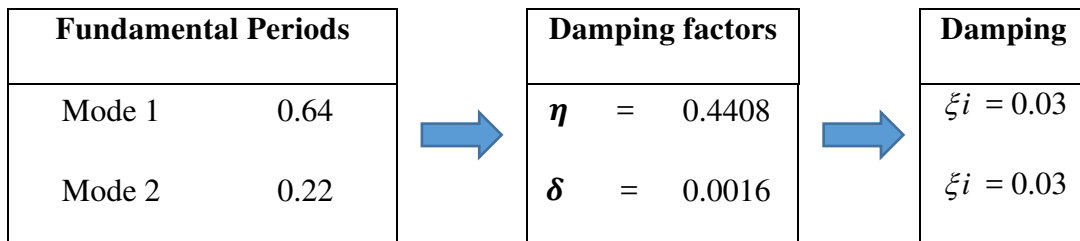
If the damping ratios ( $\xi_i$  and  $\xi_j$ ) associated with two specific frequencies ( $\omega_i$  and  $\omega_j$ ), or modes, are known, the two Rayleigh damping factors ( $\eta$  and  $\delta$ ) can be evaluated by solving a pair

of simultaneous equations. Table 5.4 shows the fundamental periods for mode 1 and mode 2 for all the three sample frames (with 50% $M_{pb}$ , 60% $M_{pb}$  and 70% $M_{pb}$  connection capacities). By solving the simultaneous equations with two modes,  $\eta$  and  $\delta$  are calculated for each model, to make it ready for the dynamic analysis:

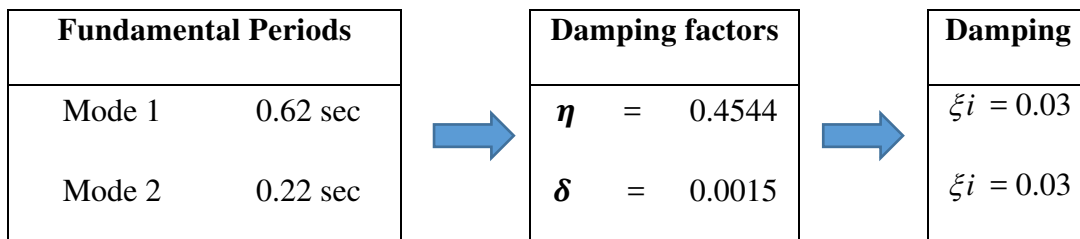
- 50% $M_{pb}$  HFC Model



- 60% $M_{pb}$  HFC Model



- 70% $M_{pb}$  HFC Model



#### **4.5. Ground Motion Record Set and Scaling – FEMA P695**

The Applied Technology Council (ATC) is tasked by the Federal Emergency Management Agency (FEMA) under the ATC-63 Project (FEMA P695) to devise a strategy to determine quantitatively global seismic performance factors that can be used for seismic design. In FEMA P695, two sets of ground motions, only ‘far-field’ record set are provided for use in dynamic analysis. The ground motion record sets incorporate an adequate number of records to allow assessment of record-to-record (RTR) changeability and estimation of median collapse intensity. Table B.1 shows the details of the far-field ground motion record set including the year, magnitude, and recording station. In this set, there are 22 ground motion records from 14 different earthquakes, of which 8 events are from the U.S. (CA) and the remaining ones are from other countries. Table B.2 shows other relevant records details including site distance, source characteristics, site, epicentral distances and various other measures. The site characteristics such as NEHRP site class and shear wave velocity are also given. For the dynamic analysis, FEMA P695 specifies the use of the far-field record set for the structures with the ‘Seismic Design Category’ of B, C or D criteria (which are the structures located away from the active faults) [22].

Table B.3 provides more details of the records, obtained from ‘PEER NGA Database’, including the record sequence number, both the horizontal components, lowest frequency, maximum peak-ground acceleration and peak-ground-velocity. The range for peak-ground-acceleration for the record set is 0.21g to 0.82g, with an average of 0.43g. The maximum shear wave velocity is 115 cm/sec and the minimum is 19 cm/sec, with an average shear wave velocity of 46 cm/sec [22]. Figure 4.5 shows response spectra of the individual 44 records (22 in each direction). The figure also shows the mean response spectrum for all records..

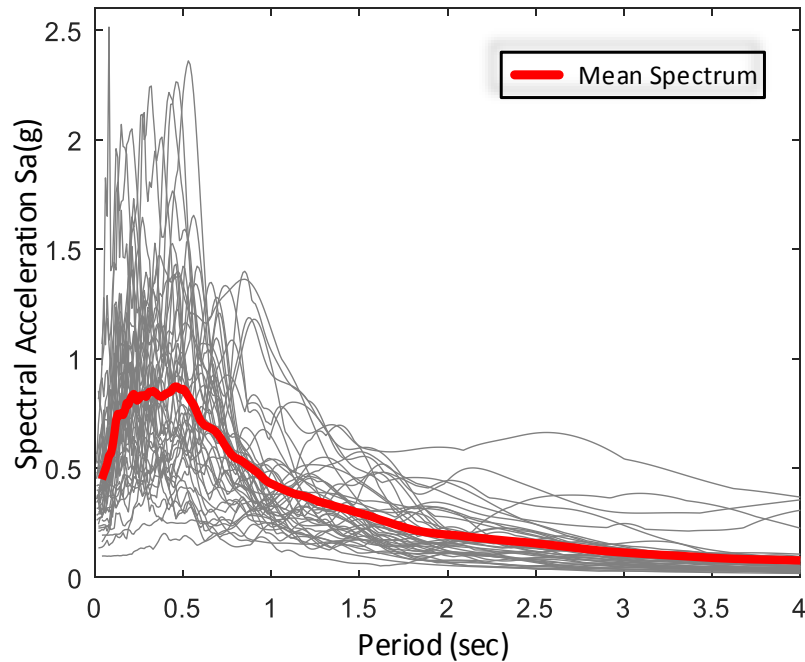


**Figure 4.5 Response spectra for far field ground motion set (44 components)**

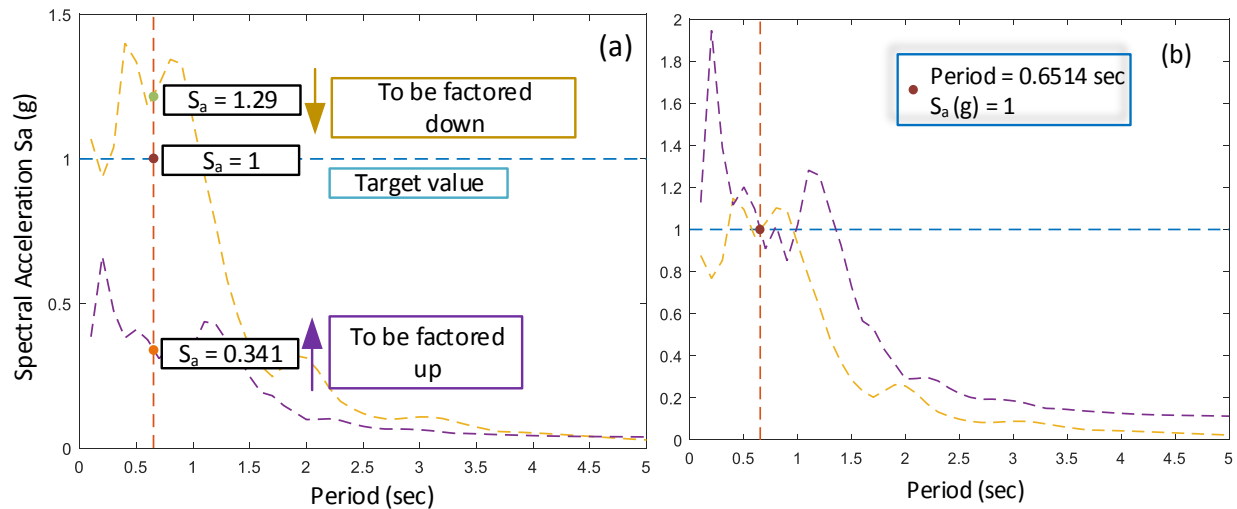
The main purpose of scaling the ground motion records is to represent them with a specific intensity, for example the collapse intensity of the sample frame in the study, or to represent a record with the intensity of ‘0.5g’ or ‘2g’ for a particular structure. Scaling of ground motion records is an essential component of nonlinear dynamic examination, since scarcely any, accessible unscaled records are sufficiently strong enough to collapse present day structures.

For collapse assessment, it is required to scale the ground motion records individually i.e. unlike ‘normalization’, each component of an event is treated as a different ground motion. The methodology requires the normalized ground-motions to be collectively scaled upwards or downwards to a specific level of excitation, for example ‘maximum considered earthquake spectral acceleration’.

This procedure of normalizing and scaling the records to match a particular level of ground-motion is analogous to the scaling requirements described in ASCE/SEI 7-05 [52], section

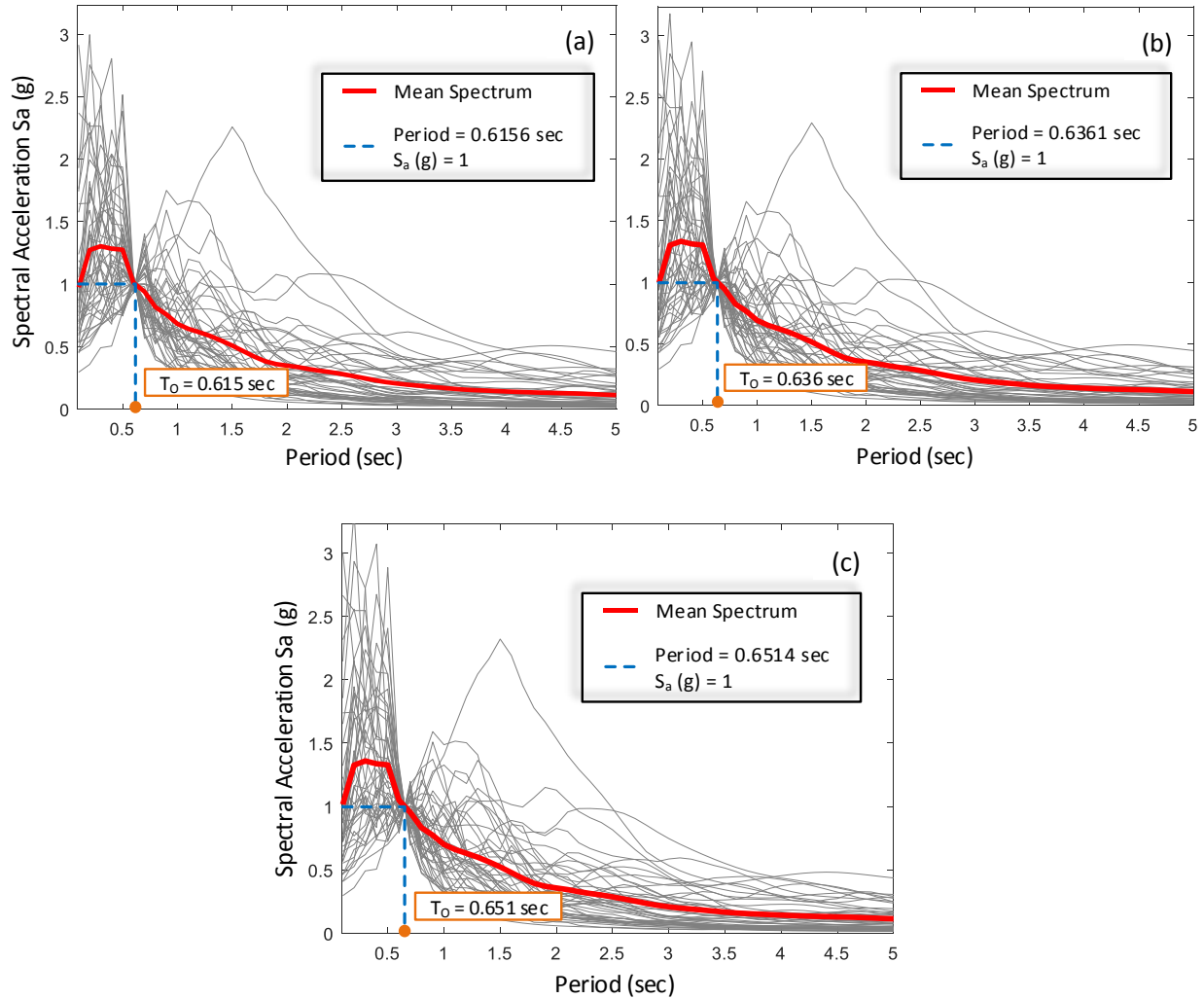
16.1.3.2, with the exception that the median value of the scaled record set should only match the MCE demand at the fundamental period (T) of the structure under the study. This is unlike ASCE/SEI 7-05 [52] which requires the records to be scaled over a range of periods.

Figure 4.6 illustrates the process for two earthquakes to be scaled for analysis model  $50\%M_{pb}$  with the fundamental period of 0.65 seconds (see chapter 4 for more details). Earthquake components ‘DUZCE/BOL090’ & ‘HECTOR/HEC000’ (see Table B.1) are used for the demonstration. The task is to anchor the response spectra of the records and their mean to the fundamental period of the structure with the spectral acceleration value of  $S_a(g) = 1$ . The value of spectral acceleration of the records considered are 1.29g and 0.34g for ‘DUZCE/BOL090’ & ‘HECTOR/HEC000’ components respectively, and after scaling both records are anchored to the fundamental period of the structure and  $S_a(g)$  value equal to 1g.



**Figure 4.6 (a) Normalized ground motion records (before anchoring), (b) Scaled ground motion records (after anchoring)**

Similarly, this process is carried out for all the earthquake records which are to be used for collapse assessment. Following show all scaled response spectra for the analysis model frame  $50\%M_{pb}$  Model,  $60\%M_{pb}$  Model and  $70\%M_{pb}$  Model respectively.



**Figure 4.7** Far-field set Scaled Response Spectra (a) for 70% $M_{pb}$  analysis model, (b) for 60% $M_{pb}$  analysis model, (c) for 50% $M_{pb}$  analysis model

#### 4.5.1. Main-shock and Aftershock Record Sequences

Structures in seismically active areas are damaged by mainshock earthquakes and can be more damaged one or more aftershocks following the main event. Even though progressed computational models have been accomplished for seismic investigation and design techniques for a very long time, current design approaches only consider the impact of mainshocks on structures. For example many earthquakes are followed by a number of strong aftershocks, the Chi-Chi

earthquake in 1999, the Northridge earthquake in 1994, the Christchurch earthquake in 2011 and many more [64].

A set of as-recorded sequences of mainshocks and aftershocks is employed for this investigation. Generally, several aftershocks follow the mainshocks, so the analysis would be accurate if all the aftershocks are used in their natural sequences, but that would be more time consuming. Even if one wishes to subject the structure to many aftershock sequences (assuming the structure has not collapsed) it is way too difficult to obtain the mainshock and aftershock sequences recorded at the same station. Hence, in this study only one aftershock immediately following the mainshock which is recorded at the same station is employed to represent an MS-AS sequence [64].

#### **4.5.1.1. PEER NGA Database**

PEER NGA (Pacific Earthquake Engineering Research Center) database is an online tool for searching, selecting and downloading the ground-motion data from worldwide. In PEER database, all downloaded earthquake records are as-recorded and unscaled. The scaled records are not available online but the tool is capable of calculating and providing the scaling factors, which are made available in the metadata of the downloaded earthquake records [65].

Using PEER NGA database, 34 earthquake records (68 components) are downloaded that were having following characteristics –

- Each event is followed by one or more aftershock sequences.
- The records are selected from such a station at which mainshock and aftershock both have been recorded.

- The aftershock with highest magnitude is considered in case where there are multiple aftershocks. That said, in most cases there is only one aftershock available on PEER NGA database and it is generally recorded at the same station as the mainshock.
- The minimum aftershock magnitude considered is 4.7.
- The stations are selected such that the site-to-source distance categorize the earthquake event as a far-field ground motion.

Refer Table B.4 and Table B.5 for the details about the mainshock and aftershock events, respectively, for the 34 earthquake records (68 components).

#### **4.5.1.2. Relationship between Mainshock and Aftershock Events**

In this study, all 68 earthquake records are not used for the MS-AS collapse assessment. The ground motions have been narrowed down to 11 ground motion events having mainshocks and aftershocks events (22 components of mainshock records and 22 components of aftershock records). To select the proper earthquakes, relationship between the mainshock peak ground acceleration and aftershock acceleration are considered.

#### **4.5.1.3. Relationship between Mainshock Magnitude and Aftershock Magnitude**

The empirical Bath's law allows for the determination of the magnitude of the largest aftershock consequent to the mainshock. However, the analysis observations are valid for only small range of magnitudes and are dependent on the selection of the mainshock-aftershock selection criteria.

In the study by *Zakharova, Hainzl and Bach* [34], the seismic moment of the aftershock events are analyzed in comparison to the seismic moment of the respective mainshock events. Because as an alternative:

- The seismic moment is the physical quantity, which considers all aftershocks and not only the aftershock with the largest magnitude.
- It is possible to correct the cut-off magnitude so that the magnitude range can be widened.
- The background activity is considered, which lessens the effects on the result estimations by the selection criteria.

*Zakharova, Hainzl and Bach* [34] provided a relationship between the magnitude of the mainshock and the mean value of the difference between the mainshock magnitude and the magnitude of the respective largest aftershock as shown in Figure 4.8 (a). The earthquake events considered in [34] occurred between 1973 and 2011 with a cutoff magnitude of 5 and are only shallow earthquake events with depth less than 50 km.

From this data, relationship between the magnitude of the mainshock event and the magnitude of the aftershock event is developed simply by subtracting the difference between the magnitudes of mainshock and aftershock ( $M_m - M_{a,max}$ ) from the mainshock magnitude ( $M_m$ ).

$$M_{a,max} = M_m - (M_m - M_{a,max})$$

*(Equation 4.5)*

After obtaining the mainshock and respective aftershock magnitude, a linear trend-line equation is developed to obtain a direct relationship between the magnitudes of the respective mainshocks and aftershocks (See Figure 4.8 (a) and (b) for the details). The observed values given in Figure 4.8 (a) are for shallow earthquake events. Since the subject structure in this study is situated in southern California, which is prone to shallow earthquake events, the developed equation representing the relationship between the mainshock magnitude and aftershock magnitude is

further incorporated to narrow down mainshock and aftershock ground-motion records so that the selected ground-motions are categorized as a shallow earthquake as the structure would experience in southern California.

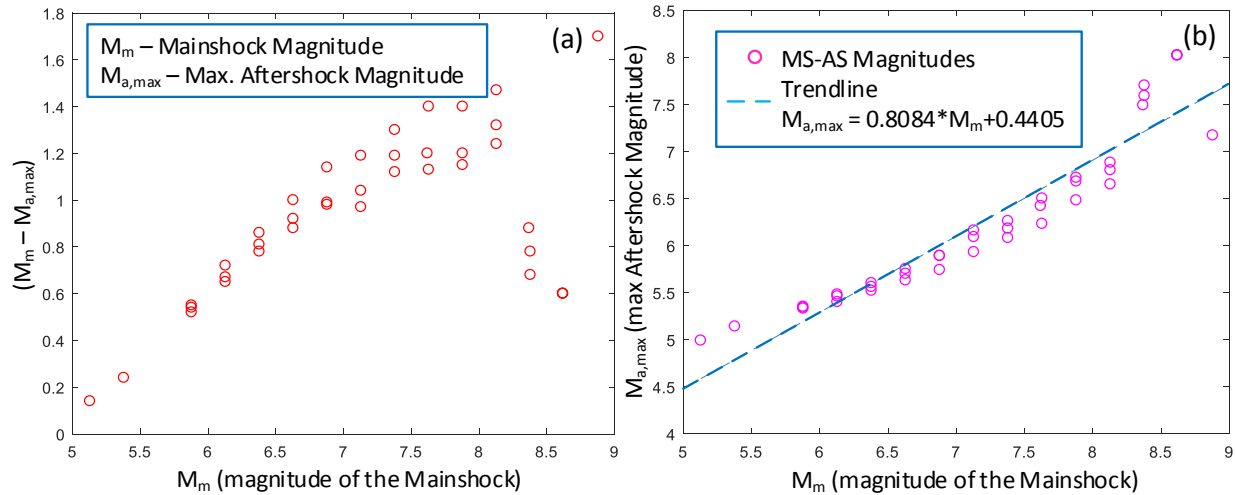


**Figure 4.8 (a) Magnitude of the mainshock versus the mean value of the difference between the mainshock magnitude and the magnitude of the respective largest aftershock, (b) Mainshock magnitude vs. maximum aftershock magnitude and relationship between the magnitudes of the mainshocks and aftershocks with a linear trend-line**

#### 4.5.1.4. Relationship between the Magnitude and the PGA

‘Hazu-MH MR5 technical manual’ [67] provides information and methodology to execute earthquake loss estimations. It depends on multi-year studies to build up a broadly pertinent approach for assessing potential earthquake losses. The main role of the project is to create rules, techniques and develop a methodology for making earthquake loss assessments. These loss assessments would be utilized fundamentally by local, state and regional authorities to design and fortify efforts to lessen losses from earthquakes and to plan for emergency response and recovery. According to ‘Hazu-MH manual’ [67], following data (Table 4.4) is used to convert M to PGA values. Using this data, an equation (Equation 4.6) is developed by using a trend-line as follows (see Figure 4.9).

**Table 4.4 Magnitude to PGA conversion**

M	6	7	8	9	10	11	12
PGA (g)	0.12	0.21	0.36	0.53	0.71	0.86	1.15

$$PGA = 0.0163 * e^{0.6371 * M}$$

(Equation 4.6)

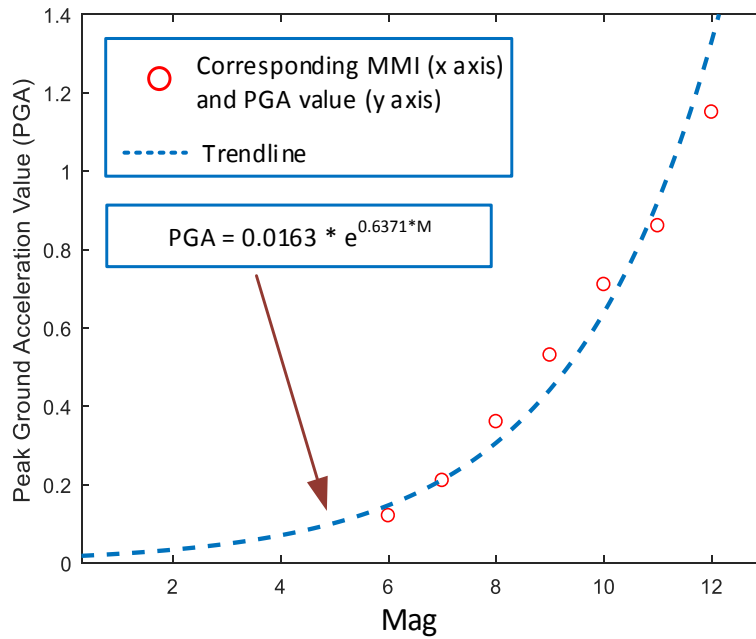


**Figure 4.9 Magnitude to PGA conversion**

Now that magnitudes can directly be converted to the PGA values, the magnitudes of the mainshocks and aftershocks (discussed in 4.5.1.3) are converted into PGA values so that relationship between the mainshock PGA and aftershock PGA is established. This equation (Equation 4.7) plays important role in scaling the aftershocks in relation to the respective

mainshocks. Figure 4.10 shows the required relationship between the mainshock PGAs and corresponding aftershock PGAs and relationship between them by using a trend line.

$$(AS\_PGA) = 0.6372 * (MS\_PGA) + 0.0153$$

(Equation 4.7)

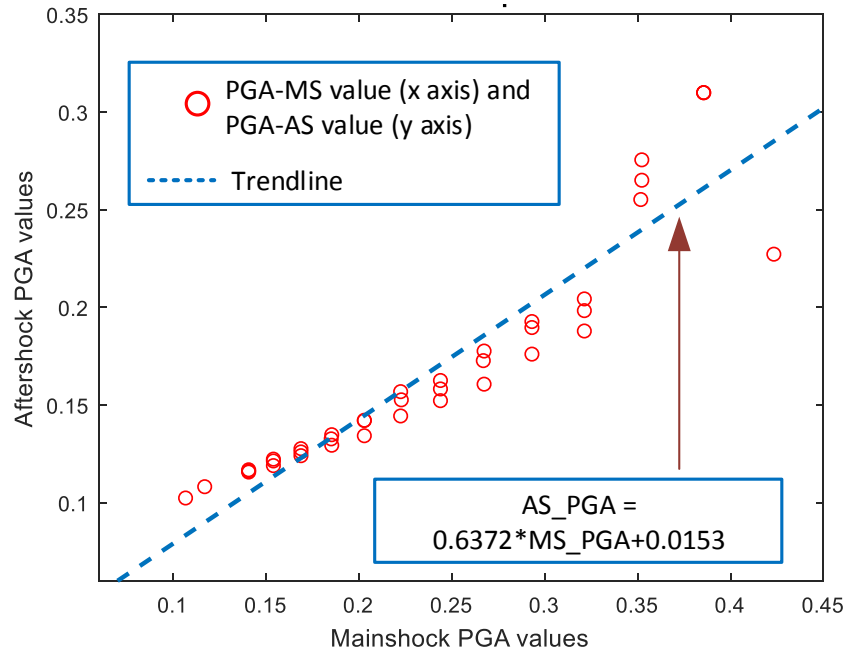


**Figure 4.10 Relationship between mainshock and aftershock PGA values**

#### 4.5.1.5. Mainshock and aftershock ground motion record set

Figure 4.11 shows PGA values of the mainshock and aftershock ground motion records mentioned in Table B.4 and Table B.5 with their current relationship and the required relationship established (Equation 4.7) in 4.5.1.4.

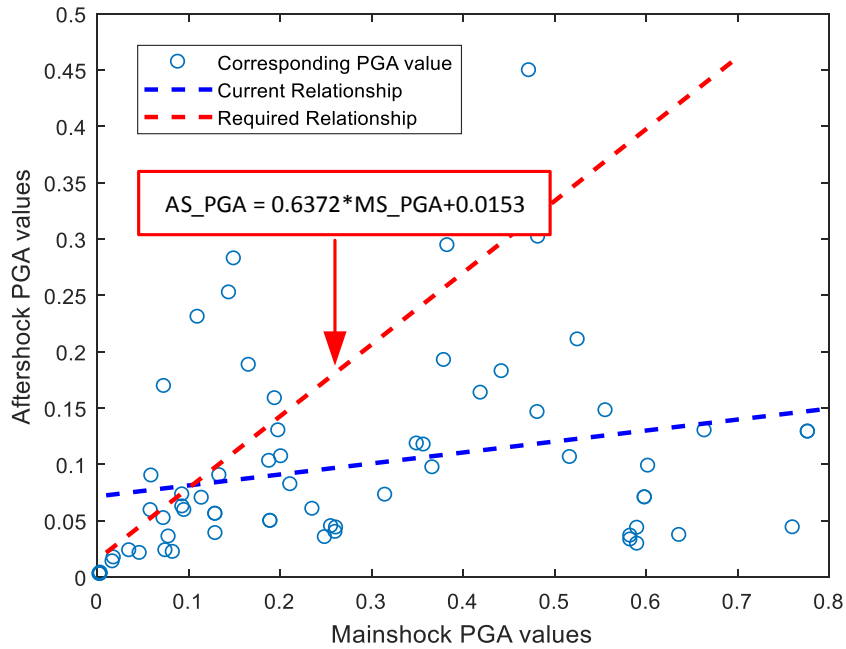


**Figure 4.11 All PGA values with current and required relationship**

Using this relationship, the selected ground motion records from PEER NGA described in Table B.4 and Table B.5 are narrowed down such that their relationship between the PGA values of the mainshocks and aftershocks represent the same relationship established above in 4.5.1.4 so that they could be categorized as a shallow earthquake and also expected to yield similar results in terms of fragility curves as compared to the standard set of ground-motions given by FEMA-P695.

Figure 4.12 (a) shows the PGA values of the selected ground motions for the analysis and Figure 4.12 (b) shows the final relationships between the corresponding PGA values. Therefore, final established corresponding PGA relationship for the mainshocks and aftershocks used for the analysis is given below (Equation 4.8).

$$(AS\_PGA) = 0.4827 * (MS\_PGA) + 0.0276$$

*(Equation 4.8)*

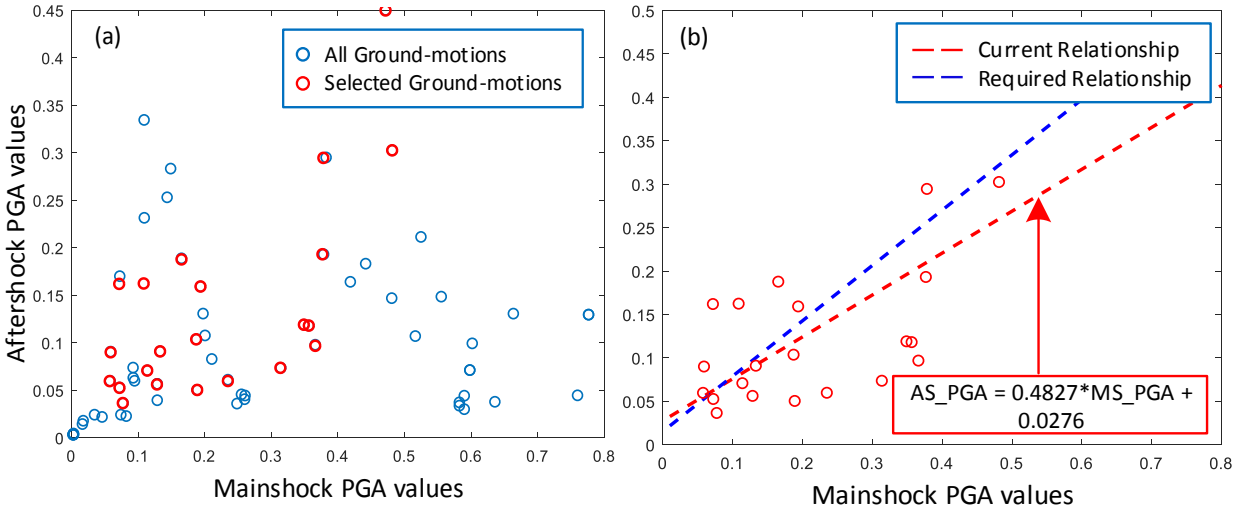


**Figure 4.12 (a) Downloaded ground motion records from PEER NGA database and (b) final relationship between the PGA values of the selected ground motion records**

Table B.6 and Table B.7 shows the details of the selected mainshocks and aftershocks for the analysis for example the record sequence number (the unique number to download the record from PEER NGA database), magnitude, PGA values, site class etc. Table B.8 and *Table B.9* shows the PGA values of all the horizontal components.

#### 4.5.1.6. Scaling - Mainshock and Aftershock Sequences

Unlike the far-field records, the scaling process for the mainshocks and aftershocks is different.

This methodology includes two steps as follows:

##### Step 1:

In this step, only the response spectra of the aftershocks (not mainshocks) are now scaled and anchored to the fundamental period of the structure.

##### Step 2:

The relative intensities of the mainshock and the aftershock are maintained. To represent the damage state of the structure before aftershock starts.

#### 4.5.1.6.1. Aftershock Scaling

The scaling procedure of the aftershocks is the same as described in section 4.5. The response spectra of all the selected aftershocks are anchored at the fundamental period of the structure, as shown in Figure 4.13 (Procedure is same for all three analysis models).

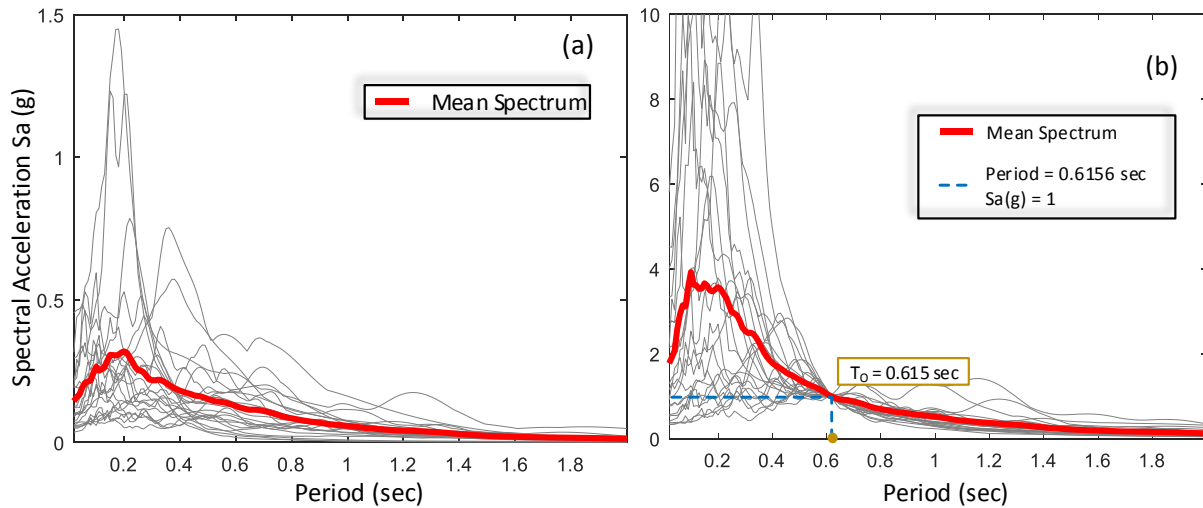


**Figure 4.13 (a) Response spectra of selected unscaled aftershock ground motion records and (b) Response spectra of the scaled aftershock ground motion records for 70%  $M_{pb}$  analysis model**

#### 4.5.1.6.2. Relative scaling between Mainshock and Aftershock

The relative intensities between the mainshocks and aftershocks are maintained to represent the expected real demand on the structures as would naturally occur. If the aftershock ground motion is not scaled properly in relation to its mainshock the structure would not be damaged at all by the aftershock or else there will be a case in which the structure will fail during the mainshock itself. Therefore, the relative scaling is done by considering the peak ground acceleration value of the mainshocks and respective aftershocks.

The relationship between the mainshock PGA and aftershock PGA, as established in 4.5.1.4 and as given below, is used to scale the mainshocks with respect to their aftershocks.

$$(AS\_PGA) = 0.6372 * (MS\_PGA) + 0.0153$$

*(Equation 4.9)*

Now that aftershocks are scaled, the mainshocks are now scaled considering the PGA values. Mainshocks are factored up or down with respect to the aftershocks by using the said relationship through considering the PGA values of the respective aftershocks. In other words, now the aftershock records represent a ground motion with a specific intensity for the structure which are already damaged by the mainshocks where their intensities are given by the above relationship with aftershock intensity. Therefore, in this study, in the dynamic collapse analysis assessment for mainshock-aftershock sequences, when it is said that the ground motion with a particular intensity, that implies, the said intensity is associated with the aftershock intensity and it is presumed that the intensity of the mainshock can be calculated by the relationship above. Figure 4.14 shows the scaled aftershocks in terms of their peak ground acceleration values. The PGA values of the mainshocks are plotted on the X-axis and the adjusted peak ground acceleration values of the aftershocks are plotted on the Y-axis. Table B.10 shows the peak ground acceleration values of each component after the relative scaling. Note that the mainshock and aftershock ground motion sequences are now ready to be used for the dynamic time-history analysis for the collapse risk assessment.

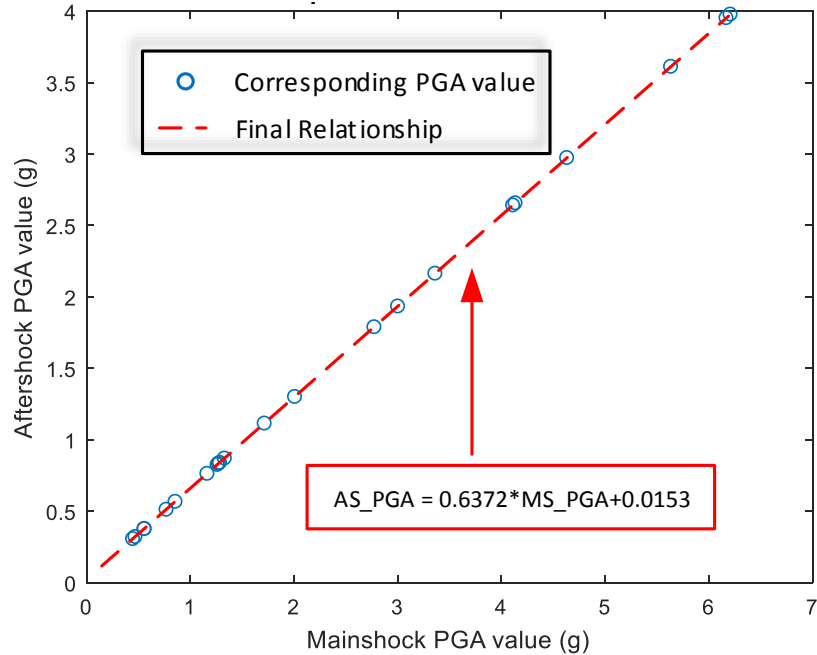


**Figure 4.14 Final PGA relationship for aftershock sequences scaled for 70% $M_{pb}$  model and scaled mainshocks scaled with respect to their aftershocks**

#### 4.6. Incremental Dynamic Analysis

Incremental Dynamic Analysis also known as IDA, is a computational analysis technique used to perform extensive evaluation of the structure and its behavior under seismic loads. In this analysis procedure, the seismic risk faced by the structure is assessed through probabilistic seismic hazard analysis [68]. Incremental Dynamic Analysis consists of carrying out multiple nonlinear time-history analysis on the subject structure using a set of selected ground motion records. In this procedure, each ground motion record is scaled to represent a particular seismic intensity. Nonlinear dynamic analysis is carried out using each ground motion multiple times at different scales. Each ground motion is scaled such that the structure is forced to go through the all-inclusive range of behavior for example from being elastic to inelastic, and again to global dynamic instability where the structure finally crosses the limit state of complete collapse.

#### 4.6.1. Ground-motion record sets and Analysis models

As discussed in this study, for the incremental dynamic analysis all three models (with 50% $M_{pb}$ , 60% $M_{pb}$  and 70% $M_{pb}$  connection capacity) have been used and the results are compared with each other. The three models have fundamental periods of  $T_1 = 0.651$  seconds,  $T_1 = 0.636$  seconds and  $T_1 = 0.615$  seconds, respectively, and include the effects of the gravity columns and global geometric nonlinearities such as P-delta effects.

In addition, for the IDA, properly scaled ground motion record sets are required (see section 4.5 for details about the selection of ground motion record sets). Total of three sets of ground motions are used in this study.

- Ground Motion Record Set – FEMA P695
  - Ground-motion record set given by FEMA-P695 [22].
  - Total of 22 earthquakes with components in each direction (44 total) as listed in Table B.1.
- Selected mainshocks (mainshocks only)
  - Ground-motion set are downloaded from PEER-NGA ground-motion database [65].
  - Total of 11 earthquakes with components in each direction (22 total) as listed in Table B.4.
- Mainshock-aftershock sequences
  - Ground-motion set downloaded from PEER-NGA ground-motion database [65].

- Total of 11 earthquake sequences with components in each direction (22 components of mainshocks and 22 components of aftershocks) as listed in Table B.4 and Table B.5 .

#### 4.6.2. Performing the analysis

The analyses are performed at increasing levels of intensity of the earthquake record until numerical non-convergence occurred, indicating dynamic instability or complete collapse of the. Considering the accuracy of the results, the IDA is conducted for earthquake intensity ranging from 0.1g to 10g at the intervals of 0.1g, i.e. 100 analyses for each earthquake record. Therefore, for the IDA, total of three sets of ground-motions (44 components, 22 and 22 components respectively) are used for three different analysis models. The total number analyses performed to obtain the IDA results for every set of earthquakes is **26400** analyses. It is important to note that while the analysis is performed up to an intensity of 10g, the occurrence of such magnitude of spectral acceleration is practically impossible.

Figure 4.15 shows the procedure for one earthquake record. The record is scaled from intensity being  $S_a = 0.1g$  to  $S_a = 0.8g$ . The engineering demand parameter considered in this analysis is inter-story drift ratio (maximum of the inter-story drift ratios among every floor). At each scale of the ground-motion, the maximum absolute displacement of the structure is observed and is plotted on X-axis against the intensity of the respective ground-motion on the Y-axis.

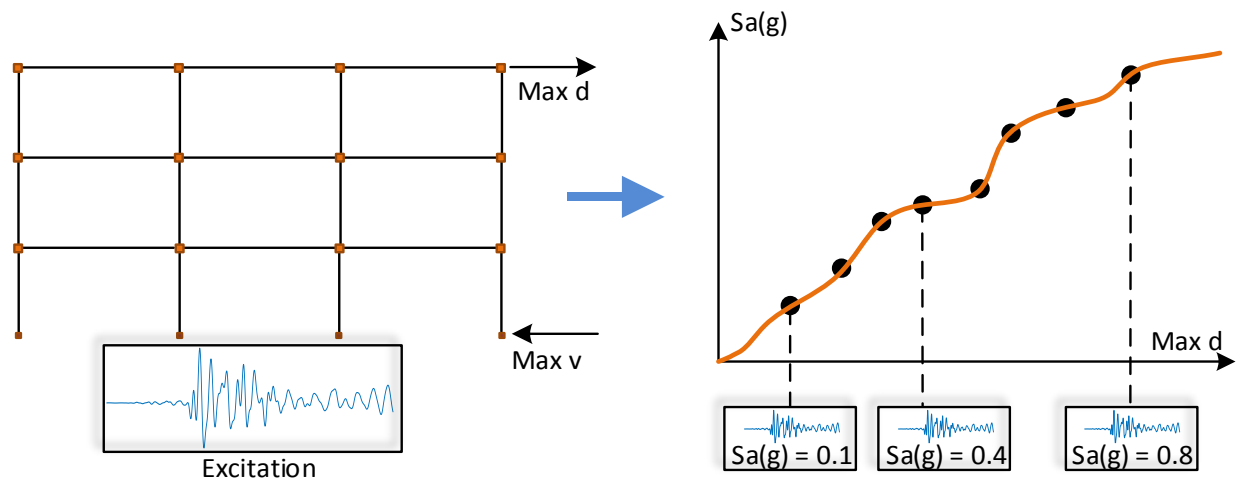


Figure 4.15 Incremental dynamic analysis procedure for one earthquake record

### 4.6.3. Damage States on IDA curves

#### 4.6.3.1. Damage States

Damage states for the structural and non-structural components are different. While in reality the damage state of a structure is a continuous variable that is function of the earthquake demand, ranges have been defined to represent a particular damage state as having a continuous scale is not practical. In general, structural damage states are described by four categories that represent the various physical condition of the building. These include slight, moderate, extensive, and complete damages as listed in Table 4.5 .

Table 4.5 Example Damage States from Hazus [61]

Damage State	Description
	<p><b>Slight</b></p> <p>Cracks visible not wider than 1/8 inch (i.e. small cracks). Small cracks in plaster at the corner of the door</p>

		and wall-window intersections. Small cracks in masonry chimneys.
	<b>Moderate</b>	Large cracks (wider than 1/8 inches) at wall-ceiling, wall-window intersections and door corners. Diagonal cracks across shear walls, also large cracks in masonry chimneys.
	<b>Extensive</b>	Large cracks in plywood intersections, at shear wall panels, even in foundations. Permanent lateral displacement of the roofs and floors. Slippage over foundations.
	<b>Complete</b>	Structure being in danger of collapse, or permanent lateral displacement of floors and roofs. At least 3% of the area of the structure is expected to be collapsed. Some structure may slip over and fall the foundations.

**4.6.3.2. Model Building Types**

Model building types are classified into several categories according to their total height, number of floors, frame materials, type of the frame (e.g., moment resisting or braced), among others. The same classification system is used in FEMA P695 [22]. Table 4.6 describes the model building type based on their height and frame type.

**Table 4.6 Model building type from Hazus [61]**

No.	Label	Description	Height			
			Range		Typical	
			Name	Stories	Stories	Feet
3	S1L	Steel Moment Frame	Low Rise	1 - 3	2	24

The structure in this study is a moment-resisting steel frame, with three-story and three bays. Therefore, as described in Table 4.6, the structure in this study falls under the category of ‘S1L’, since it is a low rise, three story building with total height of 37.4 feet (11.4 meters).

#### 4.6.3.3. Inter-story Drift Ratio

The inter-story drift ratios representing structural damage of standard buildings are in ‘Hazus-MH 2.1 Technical Manual’ [61]. These tables show the inter-story drift ratios for the standard buildings for High Code, Moderate Code, Low Code and Pre-code seismic design levels. The structure in this study falls under the category ‘S1L’. Therefore, by using the High code design level the inter-story drift ratios for the corresponding damage states are decided (given in Table 4.7).

**Table 4.7 Inter-story drift ratio of structural damage states considered in this study**

Model Building Type	Structural Damage States			
	Slight	Moderate	Extensive	Complete
S1	0.006	0.012	0.030	0.080

#### 4.6.4. Development of Fragility Curves

Fragility curves are lognormal capacities that depict the likelihood of reaching or surpassing, structural and nonstructural damage states, provided median estimates of spectral response, for instance spectral displacement. These curves consider the fluctuation and vulnerability related with the capacity curve properties, damage states and ground shakings.

Figure 4.17 shows a depiction for the fragility curves for the given damage states as per the methodology stated in FEMA P695 [22]. The figure provides information about the damage probabilities for three different levels of ground motions described as weak, medium and strong shaking for simplicity. In the actual methodology, instead of using words like 'weak', 'medium' or 'strong', actual numerical values of spectral accelerations are used to describe the ground motion intensity.

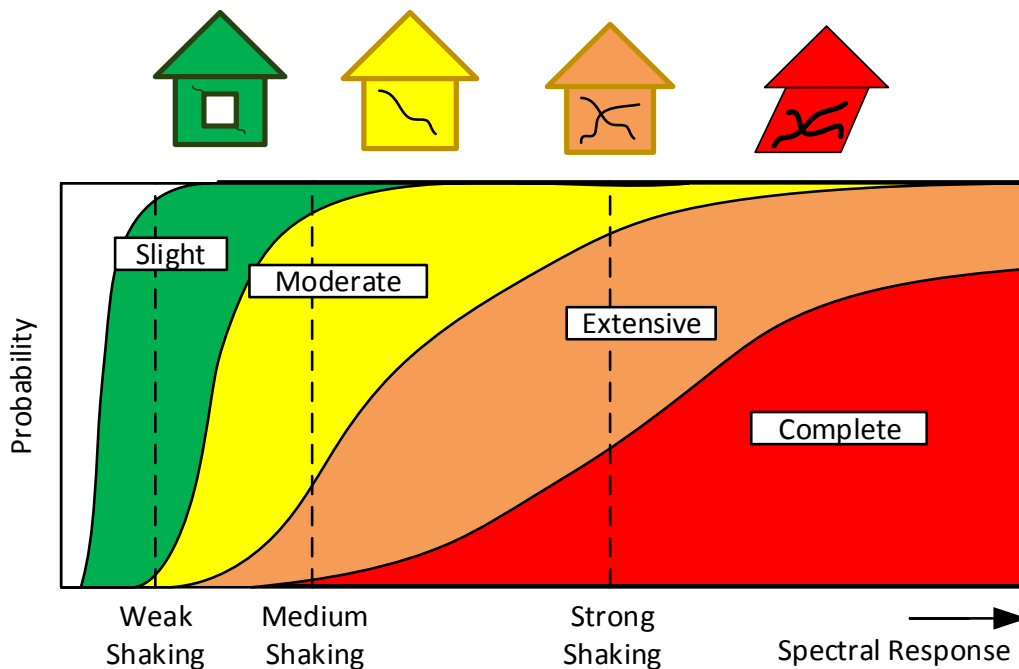


Figure 4.16 Schematic of fragility functions and their associated damage states: *after* [61]

For a particular value of spectral response, the respective damage state probabilities are calculated as the difference of the collective probabilities of reaching or exceeding a particular damage state. The fragility curves distribute the damage among the said damage states - slight, moderate, extensive and complete. Hence, the probability of a structure reaching or exceeding a specific damage state at specific response level comes to the sum of 100%. These damage state probabilities can later be used as an input to calculate several types of building related losses.

The following equation (Equation 4.10) gives the spectral displacement ( $S_d$ ), which defines the threshold of a specific damage state (ds).

$$S_d = \bar{S}_{d,ds} \epsilon_{ds}$$

(Equation 4.10)

Where,  $\bar{S}_{d,ds}$  is the median value of spectral displacement and  $\epsilon_{ds}$  is a lognormal variable with median value equal to one, and standard deviation  $\beta_{ds}$ .

The following equation (Equation 4.11) gives the conditional probability of being in or exceeding a damage state (ds) at a particular spectral displacement ( $S_d$ ) or any other demand parameter.

$$P[ds|S_d] = \phi \left[ \frac{1}{\beta_{ds}} \ln\left(\frac{S_d}{\bar{S}_{d,ds}}\right) \right]$$

(Equation 4.11)

Where,  $S_{d,ds}$  is the median value of spectral displacement,  $\beta_{ds}$  is the standard deviation of the natural logarithm of spectral displacement and  $\phi$  is the standard normal cumulative distribution function.

## **4.7. Period Elongation**

### **4.7.1. Discrete Fourier Transformation**

A musical note can be expressed in terms of the frequencies of its integral notes. In a similar way, the ‘Fourier Transformation’ (FT) deteriorates a function of time (an earthquake signal or structural response to an earthquake) into the frequencies of which the function is made up of. Therefore, ‘Fourier Transformation’ can also be called a ‘Frequency Domain Representation’ of an original signal.

The Fourier Transformation of a signal, which is function of time, is a complex-valued function of frequencies. The said frequencies are the frequencies present in the original signal. The absolute value in the transformed function represents the frequency content in the original signal and the complex argument of these transformed signal represents the phase offset of the basic sinusoid in that frequency.

For time dependent functions, Fourier Transformation is used widely to evaluate the inelastic period or frequency of the structure. Fourier transformation decomposes the signal into the oscillatory functions and represents the amplitude in a mathematical form.

The following equation [69] shows a Discrete Fourier Transformation (DFT) of the sampled values ( $X_n$ ) of N number of samples into ( $X_p$ ) values. In other words, the Discrete Fourier

Transformation is the process of transforming a series of complex numbers say  $(X_0, X_1, X_2, \dots, X_{N-1})$  into a series of complex numbers by using equation given as below.

$$X_p = \sum_{n=0}^{N-1} x_n e^{-j \frac{2\pi}{N} np}, p \in \{0, 1, \dots, (N-1)\}$$

(Equation 4.12)

Where:  $j = \sqrt{-1}$

$$x_n = x_{real} + j * x_{imag} \text{ (Complex number)}$$

Since it manages a limited measure of information, it can be actualized in computers by numerical calculation or even a committed equipment. There usage, for the most part, utilize productive fast Fourier transform (FFT) algorithms.

#### 4.7.2. Fast Fourier Transformation

Analogous to DFT, fast Fourier transformation of a time-dependent function is nothing but the extraction of the sine and cosine functions for which the said function is comprised by overlapping the sines and cosines. Fast Fourier Transformation (FFT) is a process of transforming a signal from the time domain into a representation in the frequency domain and vice versa.

In Fast Fourier Transformation, the complexity of the computation is reduced from  $O(n^2)$  to  $O(n \log n)$  (where n is the number of samples) simply by factorizing the DFT matrix to products of sparse factors (mostly zero).

FFT are generally utilized in engineering, mathematics and science and is an efficient way to evaluate the DFT and its inverse. A time-dependent real function  $x(t)$ , say  $(-L < t < L)$  can be communicated as whole of trigonometric arrangement [69] as given below:

$$x(t) = \frac{1}{2}a_0 + \sum_{n=1}^{\infty} \left( a_n \cos \frac{\pi n}{L}t + b_n \sin \frac{\pi n}{L}t \right)$$

(Equation 4.13)

Where: 
$$a_n = \frac{1}{L} \int_{-L}^L x(t) \cos \frac{\pi n}{L}t dt$$

(Equation 4.14)

$$b_n = \frac{1}{L} \int_{-L}^L x(t) \sin \frac{\pi n}{L}t dt$$

(Equation 4.15)

Therefore, after generalization, for infinite domains, the continuous Fourier transformations is expressed by the equation given below:

$$x(t) = \int_{-\infty}^{\infty} F(f) e^{-2\pi ift} df$$

(Equation 4.16)

At the point when FFT is completed on the function over, the outcome is the complex and real terms for  $F(f)$  characterized at all frequencies that demonstrates how big should the sine wave be factored up or down to make the said function  $x(t)$ , the subsequent  $F(f)$  is characterized as.

$$F(f) = \int_{-\infty}^{\infty} x(t) e^{-2\pi ift} dt$$

(Equation 4.17)

In this study, to investigate the elongated period of the structure, the FFT algorithm is carried out on the structural response in terms of top story displacement relative to the ground by using a high-level technical computing language MATLAB. The results are in the form of the frequencies contained by the structural response on the X-axis and the respective magnitude of the frequencies on the Y-axis.

Figure 4.17 illustrates an example of Fast Fourier transformation of a sample signal. The said signal is nothing but a simple sine wave with frequency equal to 2Hz. As can be seen in Figure 4.17(a), the signal contains only one frequency equal to 2Hz, therefore, the Fourier transformation of the signal, Figure 4.17(b), shows the peak value of period 0.5 seconds with power magnitude 436.4. Hence, it is confirmed that the dominating frequency in the given signal is 2Hz i.e. period of 0.5 seconds.

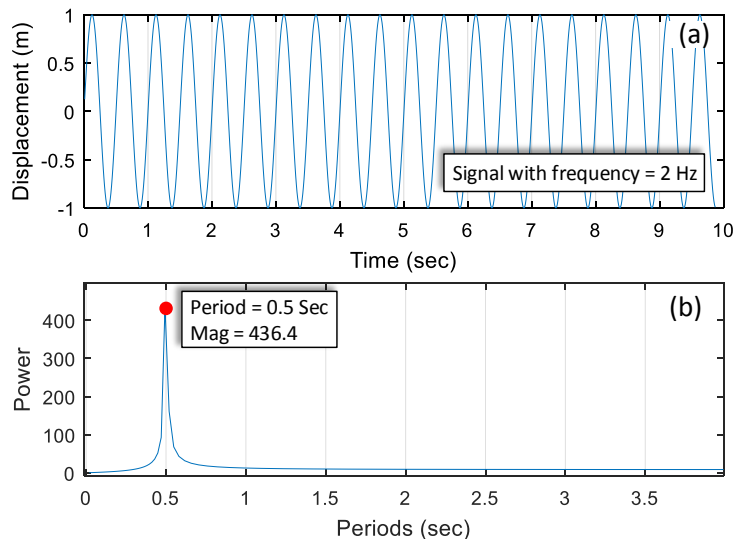


**Figure 4.17 (a) Sample sinusoidal wave with frequency equal to 2Hz, (b) FFT analysis of a simple sine wave with frequency 2Hz i.e. period of 0.5 seconds**

Similarly, the same analysis procedure is carried out on the structural response i.e. the roof displacement relative to ground in order to calculate the dominating period or frequency at which the structure is vibrating during the earthquakes.

In Figure 4.18, the response of the model frame with connection capacity equal to 50% is analyzed for Fourier Transformation. The response for the earthquake ‘DUZCE/BOL090’ (see Table B.1 for more details) is considered as an example (Figure 4.18 (a)). As discussed in chapter 4, the fundamental period of the frame with connection capacity equal to 50% is 0.6515 seconds, but as shown in Figure 4.18 (b), the dominating period in the considered signal is equal to 1.667 seconds, which is greater than the fundamental period of the structure. Therefore, it is concluded that, the inelastic period of the structure is 1.667 seconds i.e. elongated period.

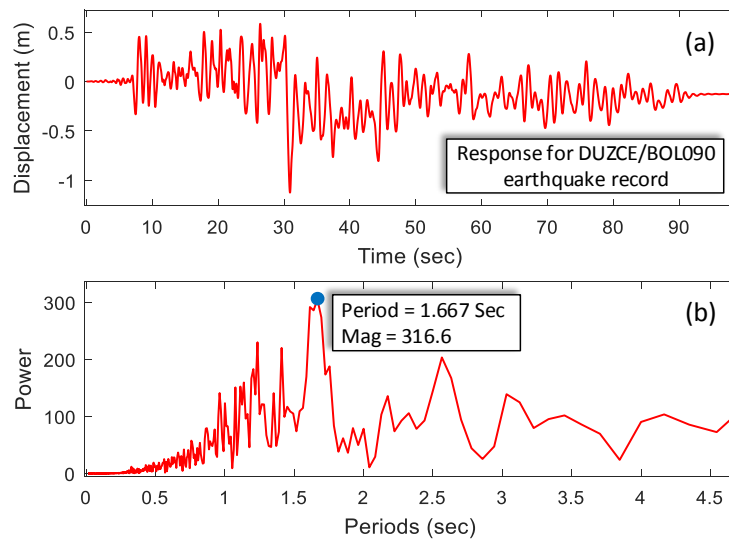


**Figure 4.18 (a) Structural response of the 50% Mpb model frame for the earthquake ‘DUZCE/BOL090’, (b) FFT analysis of the signal**

#### 4.7.2.1. Limitations

Fourier transformation is viewed as an essential tool for signal processing and understanding the structural response. However, Fourier transformation provides insight on the inelastic period of the structure, which is sufficient when the response is governed by the first mode of the structure [69].

Nonetheless, for higher modal participation, the data accumulated from conducting the FFT seems, by all accounts, to be washed away by the unpredictability of the response.

The failure of the FFT to catch the time-fluctuating response of the structure inspired the utilization of time-recurrence change for dissecting the high transient content of the signal [69].

### 4.7.3. Short-time Fourier Transformation

Short-time or Short-term Fourier Transformation, ‘STFT’ is a signal processing tool used to assess the phase content along with the sinusoidal frequencies of the short-time sections of the signal in the time domain [49]. In the STFT computation, a signal is divided into small overlapping sections where each section is analyzed and transformed separately. This uncovers the Fourier range on each shorter portion. Then the changing range of the Fourier spectrum can be plotted in time domain i.e. as a function of time. Therefore, by including the time scale into the Fourier Transformation investigation empowers for the measurement of the modular cooperation at a given instance of time [69].

Similar to FFT, STFT is also carried out in two ways - Discrete and Continuous Fourier Transformation. In this study, the discrete time case is implemented to process the behavior of the structure and ultimately to investigate the elongated periods of the model frames. By using the following equation, the series is divided into small sections of overlapping segments where each segment is transformed and the matrix recording the phase and the magnitude is updated by the results which are complex numbers. As each of the segment is going through the transformation, the matrix is updated at each point in time and frequency [69].

$$STFT\{x[n]\} \equiv X(m, \omega) = \sum_{n=-\infty}^{\infty} x[n]\omega[n - mR]e^{-j\omega n}$$

(Equation 4.18)

Where  $x[n]$  is the signal input at time  $n$ ,  $\omega[n]$  is the window length of the small segments,  $m$  is a window function such as ‘hamming’ and  $R$  is the step size between the samples during the successive DTFT.

The transformation of the signal by using STFT yields results in terms of frequencies, amplitude of the frequencies and time. The analysis is been conducted by using a technical computing language called MATLAB as discussed above, and the results are obtained in the form of a spectrogram.

#### 4.7.3.1. Spectrogram

The spectrogram is the visual representation of the results from STFT in terms of a three-dimensional matrix. In its most common format, it has two geometric axis, one being frequency axis (vertical) and the horizontal axis represents time. The third dimension is denoted by the color bars to represent the amplitude of the frequency through the intensity of the colors. The following formulation is used to calculate the spectrogram by squaring the magnitude of the STFT of the given signal.

$$spectrogram(t, \omega) \equiv |STFT\{x[n]\}|^2$$

(Equation 4.19)

To demonstrate an example, a sample signal is analyzed for STFT and the results are plotted in the form of a spectrogram. The said signal is a simple sinusoidal wave with changing frequency over time. It has three frequencies as 3Hz, 2Hz and 1Hz changing along with time.

As discussed above, the frequencies of the signal change from 3Hz to 2Hz and then to 1Hz. Similarly, in the respective spectrogram, the X-axis being the time domain, Y-axis representing the frequencies, the third dimension (Z-axis) which is been represented by the color bars to denote the intensities, the intensities of the frequencies 3Hz, 2Hz and 1Hz are the highest in the respective time domain. Therefore, it can be said that at a particular time instance, the frequency with highest amplitude is the most dominating frequency.

Figure 4.19(a) shows a sample signal used for illustration and Figure 4.19(b) gives the spectrogram of the same signal, only showing frequency range till 4Hz along with color bar stating the values of the amplitudes for the colors used in the spectrogram.

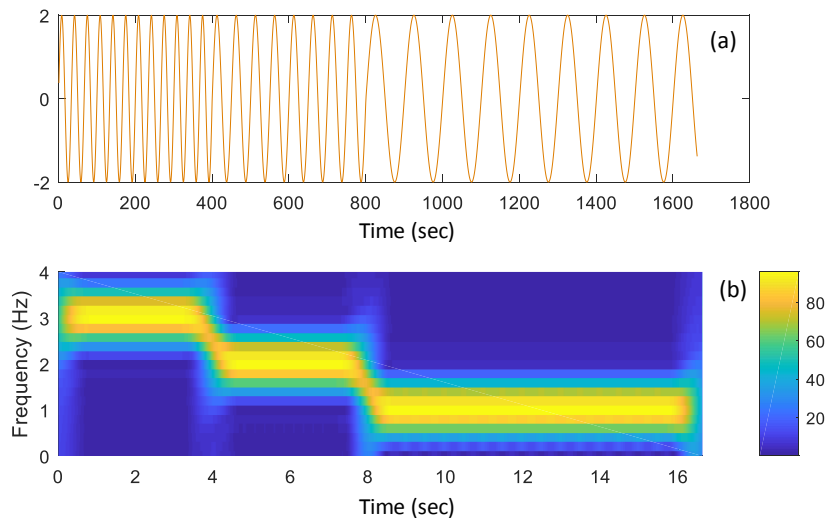


**Figure 4.19 (a) Sample sinusoidal wave with frequency equal to 3Hz, 2Hz and 1Hz, (b) Spectrogram of the Simple sinusoidal wave with three different frequencies**

As discussed above, spectrogram is nothing but a visual representation of the frequencies along with their amplitudes presented in the time domain. However, the usefulness of the results in this form not of much use. Therefore, from the spectrogram the specific values of the frequencies at each time instance has to be calculated, so that the structural behavior in terms of its changing periods of the vibration can be assessed.

Figure 4.19 (b) is a spectrogram comprised of pixels, each of which have specific color and each color has specific value, say weight of the frequency. Therefore, to calculate the exact frequency at a particular time a weighted average of all frequencies at that time is calculated, provided that the intensities or amplitudes, which are on the Z-axis and are represented by the colors are the weights of the respective frequency at the respective time. The following equation is used to calculate frequency at time t:

$$freq[t] = \frac{\sum_{freq_n=0}^N (freq_n)(weight_n)}{\sum_{n=0}^N (weight_n)}$$

(Equation 4.20)

Where -  $\sum_{freq_n=0}^N (freq_n)(weight_n)$  = Sum of the products of the frequency and the respective

$$\sum_{n=0}^N (weight_n) = \text{Sum of all the weights at time = t}$$

After calculating the weighted average at each point of time, the calculated frequency is plotted on the Y-axis while keeping the time values on the X-axis. In this way, the changing frequency of the signal is tracked along with the time scale. Figure 4.20 shows the spectrogram and the tracked changing frequency of the signal in the same time domain. The same process is carried out on the structural responses where the top frame drift is the signal being processed.

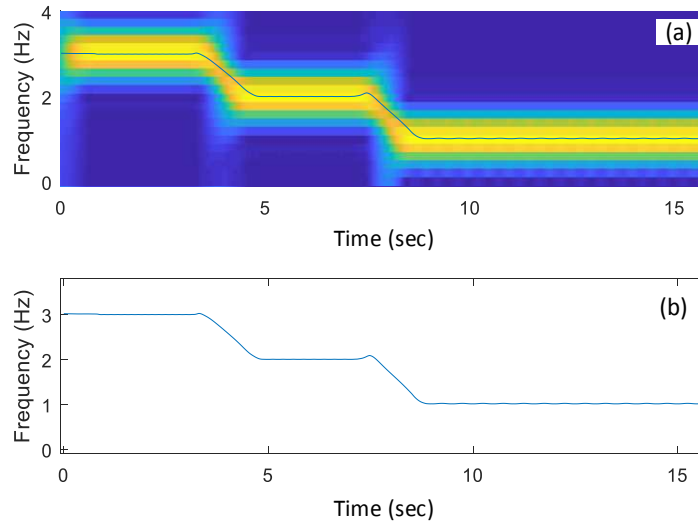


**Figure 4.20 (a) Spectrogram of the sample signal and (b) Tracked frequency of the sample signal in the same time domain**

The response of the structure in terms of ‘top-story drift’ versus time under a specific earthquake, is treated as a signal as it has been processed above. Under the earthquake structural response changes as the structure undergoes the damage. As the frame is damaged, the flexibility of the system changes and it affects the period of vibration, which elongates as the frame continues to undergo damage. Therefore, by tracking the changing period of the vibration the damage state of the structure and the inelastic period of the structure can be calculated.

#### **4.7.4. Data Collection**

The top-story displacement history of the structures are collected from the incremental dynamic analysis. For period elongation, the top-story displacement history from all the 22 mainshock earthquake records, at spectral intensity of  $S_a = 1g$  and  $S_a = 2g$ , are transformed to evaluate the elongated period. In the case of aftershocks, instead of the whole displacement history from the mainshock-aftershock sequences, the top-story displacement history of the structure under only aftershock has been processed at the spectral intensity of  $S_a = 1g$  and  $S_a = 2g$ .

To represent the elongated period of the structure, only the average of the changing period along the time is documented as the elongated period of the structure for that particular earthquake at that particular spectral intensity. Therefore, for mainshocks there a total of 22 values of elongated periods at  $S_a = 1g$  and  $S_a = 2g$  and the same for the aftershocks.

The observations from the results are presented in the form of an equation, which is developed by evaluating period elongation of as a function of connection capacity. The results are displayed in two ways. First the relationship is displayed between the elongated period of the structure and its connection capacity for the selected mainshock records. Second, the same relationship is plotted for the aftershocks from the record set of mainshock-aftershock sequences. It can be observed that as the connection capacity decreases, the extent of period elongation increases for all observations as will be shown in the Chapter 5.

## CHAPTER 5. RESULTS AND OBSERVATIONS

Three model frames with different connection capacities, equal to 50%, 60% and 70% of the plastic moment capacities of the respective beams, are analyzed in this study. The assessment is conducted using static pushover analyses, and eigenvalue analyses, and non-linear incremental dynamic analysis. In addition, the structural behavior is assessed in terms of period elongation by making use of Short-term Fourier Transformation analysis. In this chapter, all analysis results are summarized, interpreted, and discussed.

### 5.1. Pushover Analysis

Figure 5.1 (a) shows the pushover curves for the models with connection capacity equal to 70%, 60% and 50% respectively of the plastic moment capacity of the respective beams. To check the authenticity of the design and modeling of the frames, the results of the pushover analysis are compared with the work of Aksoylar, Elnashai, & Mahmoud [13] as shown in Figure 5.1(b). The comparison shows very good agreement between the behavior of the frames modeled in this study and those modeled by Aksoylar et al. [13].

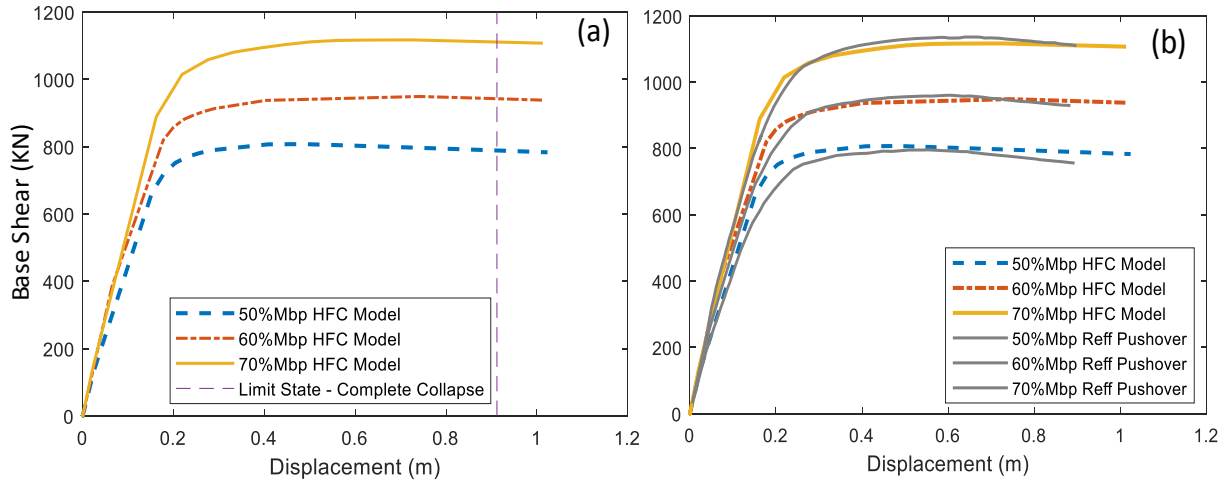


**Figure 5.1 (a) Pushover curves of the sample frames, (b) Pushover curves compared to the reference frame in [13]**

### 5.1.1. Initial Stiffness

In this study, the model frames have different connection capacities. As the connection capacities change the structural behavior changes, which can be observed in the pushover curves. As the connection capacity decreases, the stiffness of the entire structure decreases. Table 5.1 shows the initial stiffness of the model frames and the connection capacities. It is observed that as the connection capacity in the frame decreases, the initial stiffness is reduced as well. As the units of the base shear is ‘kN’ and the displacements are in ‘m’, the units of the said stiffness is ‘kN/m’.

**Table 5.1 Initial stiffness and the connection capacities of the model frames**

<b>Connection Capacity</b> <b>(M<sub>pb</sub>)</b>	<b>Initial Stiffness</b> <b>(kN/m)</b>
50%	4,347
60%	4,702
70%	5,484

### 5.1.2. Over-strength factor

Table 3.1 depicts the design base shear values for each of the model frames. Figure 5.2 shows the pushover curve of the model frames with connection capacity 50% $M_{pb}$ , 60% $M_{pb}$ , and 70% $M_{pb}$ , respectively. Design parameters such as maximum strength, design strength, and over-strength factor are also shown in the Figure 5.2. Table 5.2 shows the over-strength factors of the model frames with their maximum strengths along with their connection capacities and the design base shear.

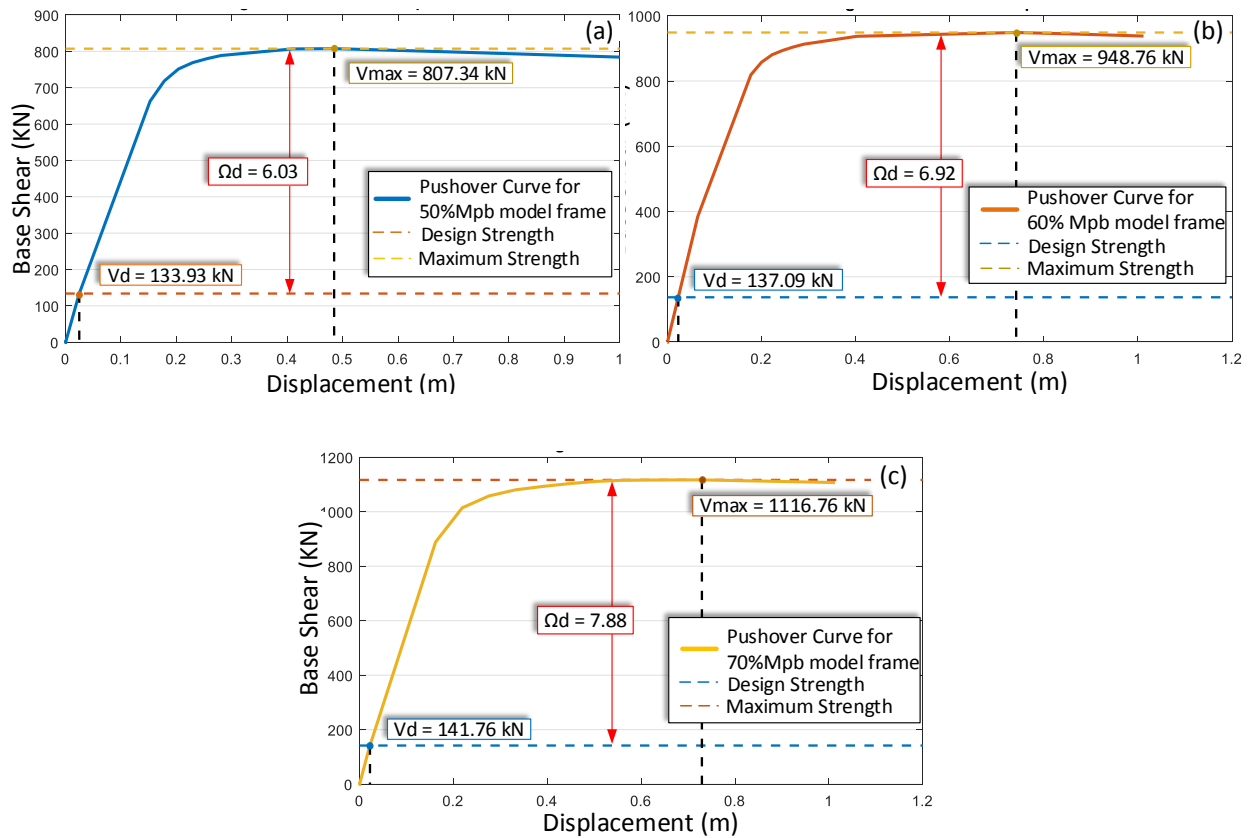


Figure 5.2 Design strength, maximum strength and over-strength factor (a) 50% $M_{pb}$  model frame, (b) 60% $M_{pb}$  model frame, (c) 70% $M_{pb}$  model frame

**Table 5.2 Maximum strength, design strength and over-strength factor of the model frames with their respective connection capacities**

<b>Connection Capacity (<math>M_{pb}</math>)</b>	<b>Maximum Strength (KN)</b>	<b>Design Strength (KN)</b>	<b>Over-strength Factor</b>
50%	807.34	133.93	6.03
60%	948.76	137.09	6.92
70%	1116.76	141.76	7.88

### **5.1.3. Ductility Ratio**

The yield displacement is calculated by evaluating the displacement at 75% of the base shear and taking an equivalent displacement at the maximum shear [63] as shown in Figure 5.3. Table 5.3 show the relationship between yield and ultimate displacements and ductility ratio for the model frames with their connection capacities.

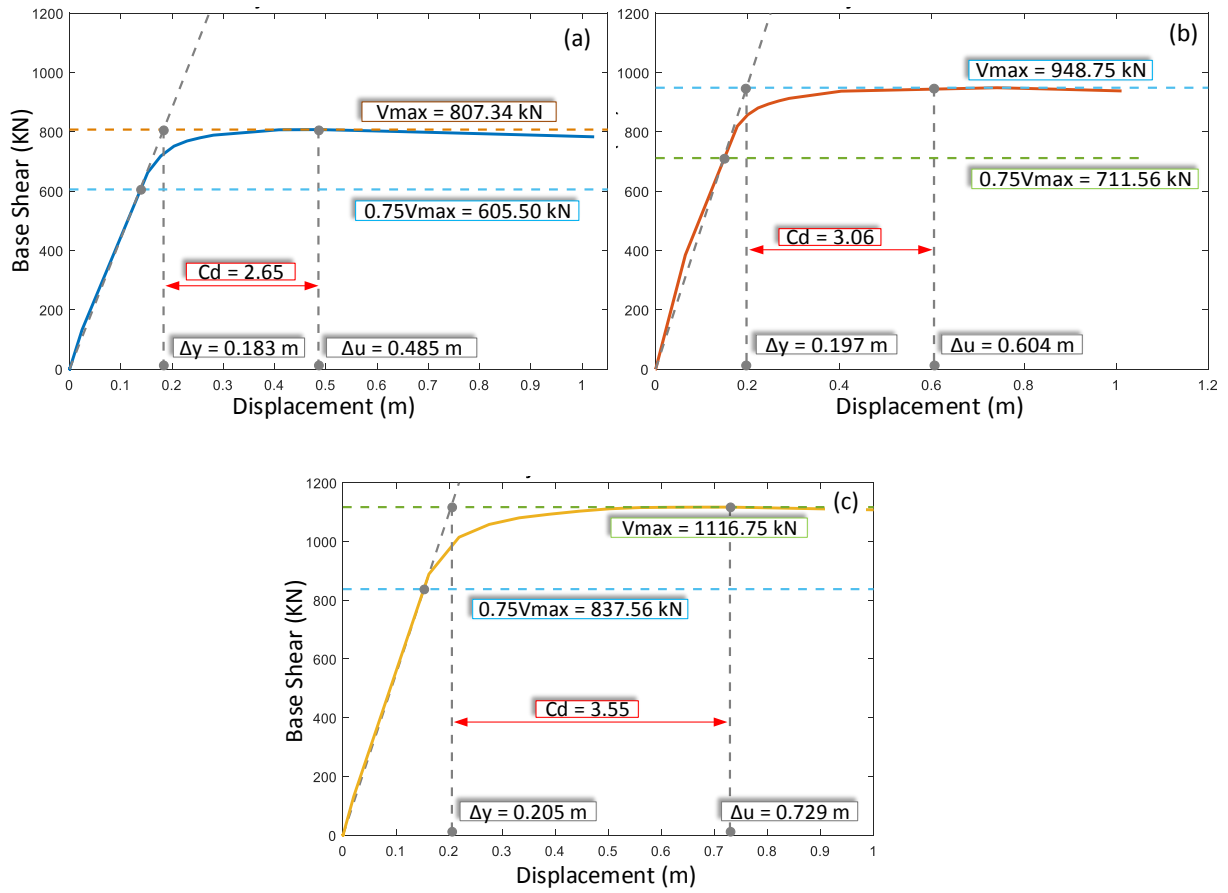


Figure 5.3 Relationship between the ultimate and yield displacement to the ductility ratio, (a) 50% $M_{pb}$  model frame, (b) 60% $M_{pb}$  model frame, (c) 70% $M_{pb}$  model frame

Table 5.3 Yield displacement, ultimate displacement and ductility ratio of the model frames with their respective connection capacities

Connection Capacity ( $M_{pb}$ )	Yield Displacement	Ultimate Displacement	Ductility Ratio
50%	0.18	0.49	2.65
60%	0.20	0.60	3.06
70%	0.21	0.73	3.55

## 5.2. Eigenvalue Analysis

### 5.2.1. Fundamental Periods

Three model frames with different connection capacities are analyzed. As we know, the connection capacities are  $50\%M_{pb}$ ,  $60\%M_{pb}$  and  $70\%M_{pb}$ , where capacities are represented in terms of percentage of the plastic moment capacity of the respective connected beam.

As discussed earlier, it is observed that the fundamental period increases as the structure becomes more flexible. In other words, as the connection capacity decreases, the fundamental period increases (see Figure 5.4 for details). Zeus-NL, for eigenvalue analysis, gives ten mode shapes and respective frequencies as results. Table 5.4 (a), (b) and (c) show the period for the first two modes of the frames.

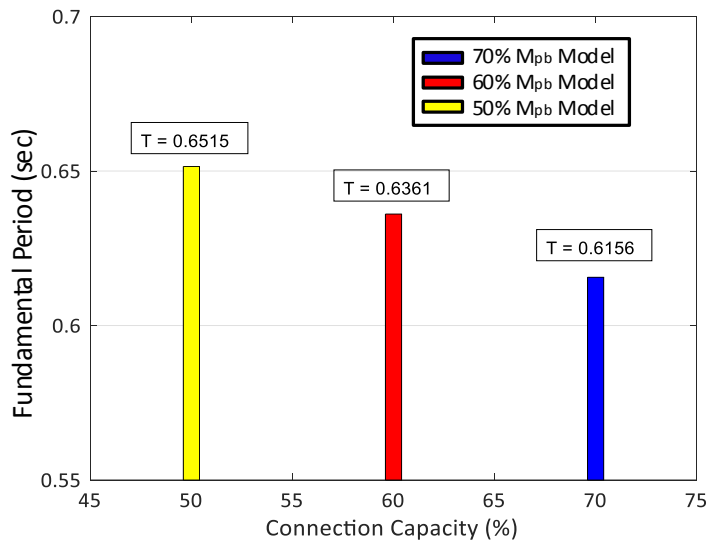


Figure 5.4 Fundamental periods and connection capacities

**Table 5.4 Modes and fundamental periods**

<b>(a)</b>		<b>(b)</b>		<b>(c)</b>	
<b>50%<math>M_{pb}</math> Model Frame</b>		<b>60%<math>M_{pb}</math> Model Frame</b>		<b>70%<math>M_{pb}</math> Model Frame</b>	
Fundamental		Fundamental		Fundamental	
Mode	Period (sec)	Mode	Period (sec)	Mode	Period (sec)
Mode 1	0.6514	Mode 1	0.6361	Mode 1	0.6156
Mode 2	0.2251	Mode 2	0.2193	Mode 2	0.2138

### **5.3. Incremental Dynamic Analysis**

Incremental dynamic analysis is carried out using three different sets of ground motions for the model frames in the study as per the procedure described in section 4.6.2.

#### **5.3.1. Ground Motion Record Set – FEMA P695**

The IDA results obtained using the ground motion set given by FEMA-695 [22] are shown in Figure 5.5. In this ground motion set, 44 earthquake records (components of 22 earthquakes in each direction) are used. Therefore, there are total 44 IDA curves as can be seen in the figure.

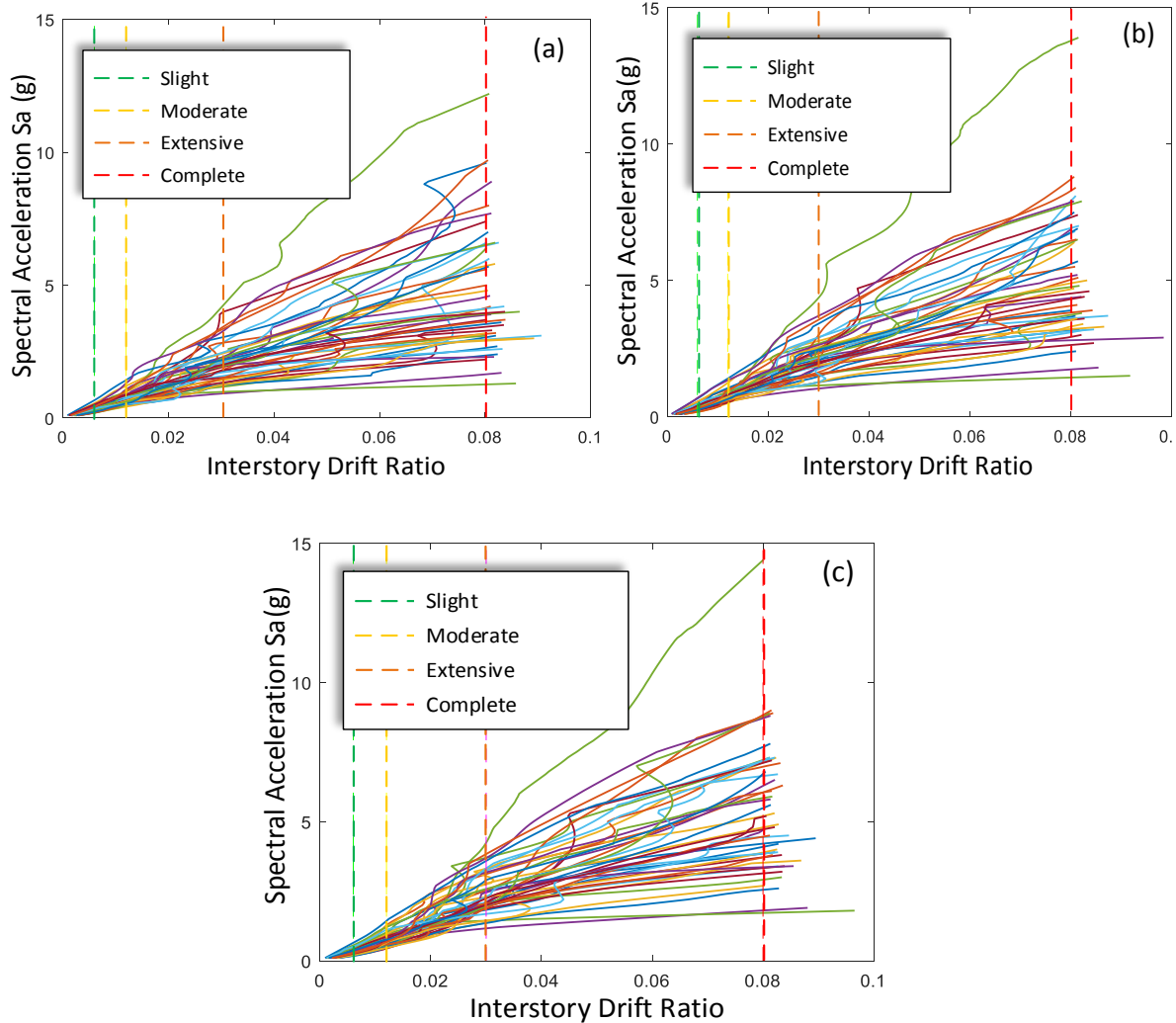


**Figure 5.5 Incremental dynamic analysis results for FEMA-P695 records set, (a) 50% $M_{pb}$  model frame, (b) 60% $M_{pb}$  model frame, (c) 70% $M_{pb}$  model frame**

### 5.3.2. Selected Mainshocks

As described in section 4.5.1.5, total 22 mainshock-aftershock sequences are selected. Now the incremental dynamic analysis procedure is carried out using only the mainshocks. The scaling process of the mainshocks is exactly the same as described in section 4.5 (Ground Motion Record Scaling). Figure 5.6 shows the IDA results for the three sample frames using the selected mainshocks.

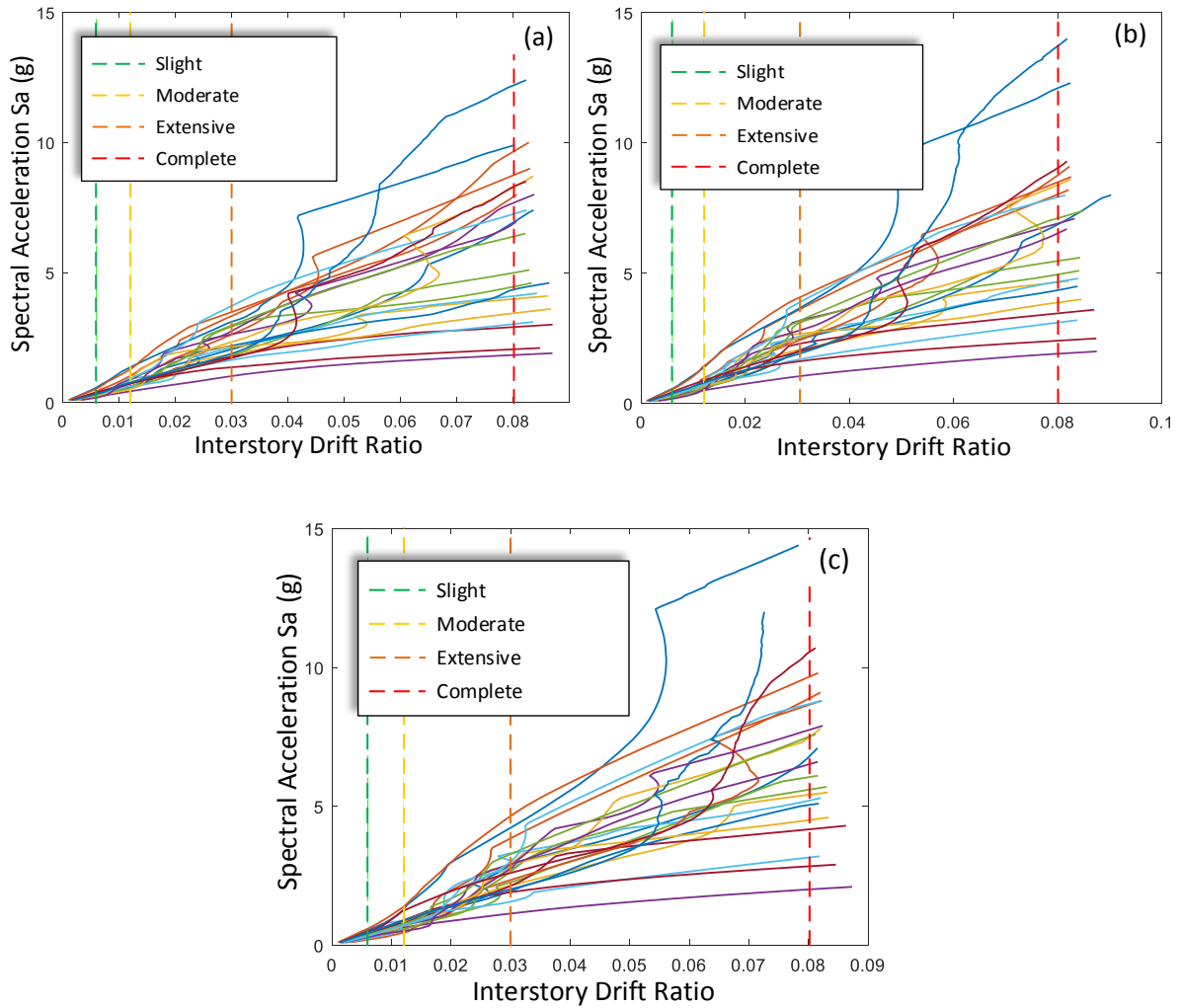


**Figure 5.6 Incremental dynamic analysis results for selected mainshocks only (a) 50% $M_{pb}$  model frame, (b) 60% $M_{pb}$  model frame, (c) 70% $M_{pb}$  model frame**

### 5.3.3. Mainshock - Aftershock Sequences

The third set of ground motions i.e. the mainshock-aftershock sequences (section 4.5.1.5) is now used to obtain the IDA results. In this analysis, the model frames are subjected to dynamic loading using the entire ground motion sequences i.e. aftershocks immediately after mainshocks when the structure has stopped oscillating after the mainshock shaking.

The IDA analysis results for only the aftershocks are plotted in Figure 5.7 since the behavior of the structure through the aftershocks is of main interest of the study. It is observed that the inter-

story drift ratio for each earthquake does not start from zero for some earthquakes. This is because the presence of residual drift of the structure when it was subjected to the mainshock. There are a total of 22 earthquake records (11 earthquake events, 22 components in each direction i.e. 22 mainshocks and 22 aftershocks).

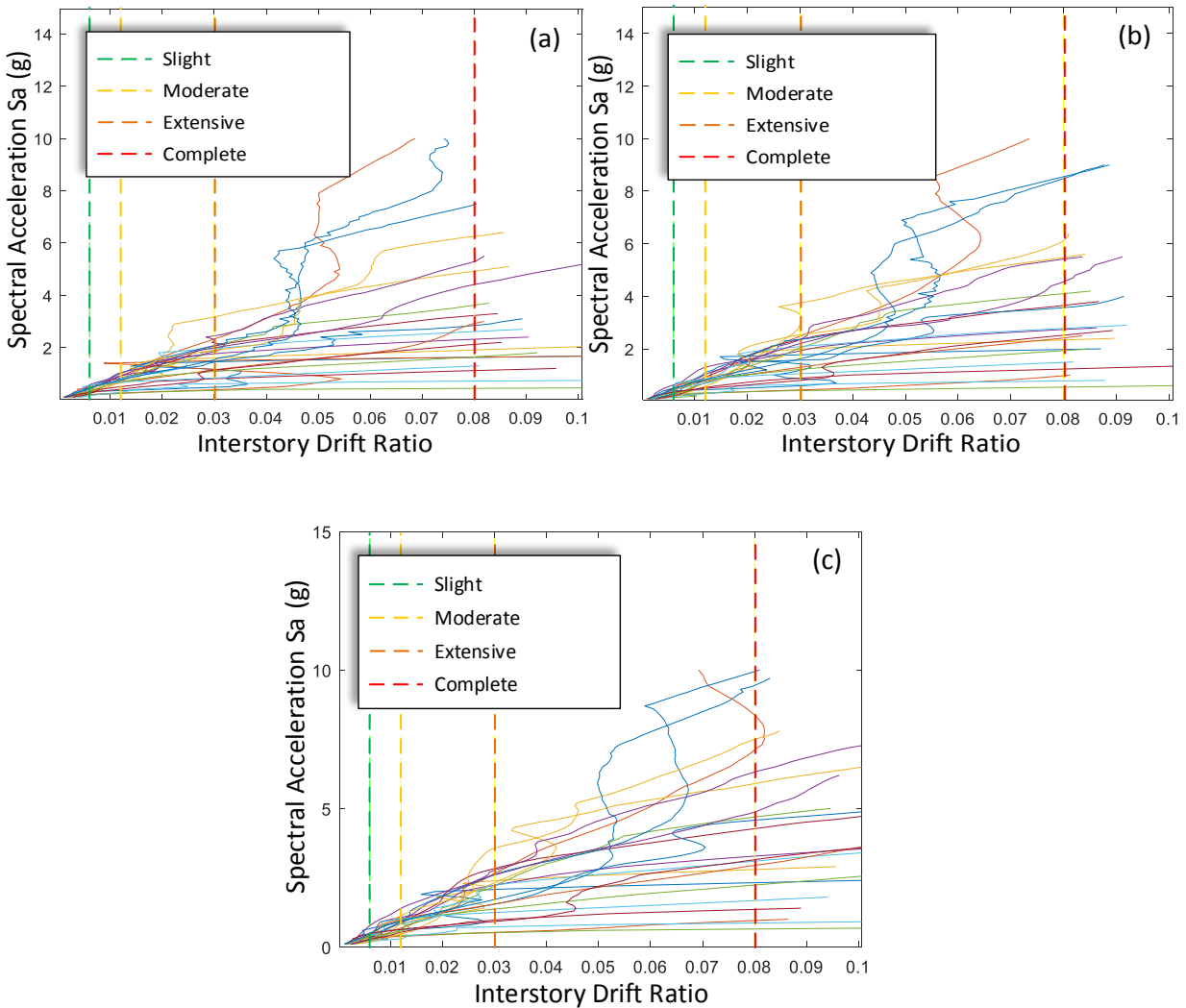


**Figure 5.7 Incremental dynamic analysis results for mainshock-aftershock sequences (a) 50% $M_{pb}$  model frame, (b) 60% $M_{pb}$  model frame, (c) 70% $M_{pb}$  model frame**

### **5.3.4. Fragility Curves**

For the three sets of earthquake records used (i.e. 44, 22 and 22), the probability of exceeding each damage state at a particular spectral intensity is calculated simply by dividing the number of failures (i.e. number of times the structure exceeded the damage state limit) by the total number of earthquakes used. Using the calculated probabilities, the fragility curves are developed (as described in section 4.6.4) to provide the final results in terms of probability of exceedance a particular damage state on Y-axis versus the intensity of ground-motions in terms of ‘spectral acceleration’ on X-axis.

#### **5.3.4.1. Ground Motion Record Set – FEMA P695**

Figure 5.8 show the fragility curves for the three models subjected to the 44 individual earthquake records given in FEMA-P695. Figure 5.9 contains all the fragility curves for all three models for comparisons.

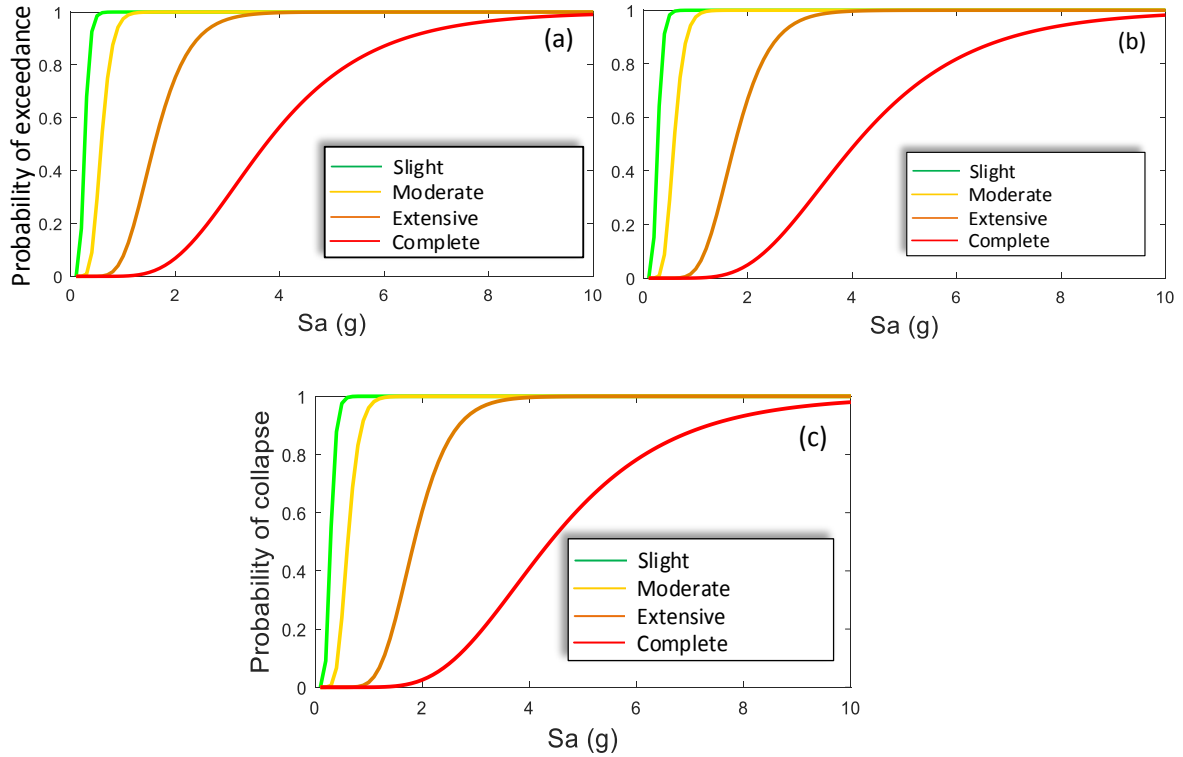


**Figure 5.8 Fragility curves for FEMA-P695 ground-motion record set (a) 50% $M_{pb}$  model frame, (b) 60% $M_{pb}$  model frame, (c) 70% $M_{pb}$  model frame**

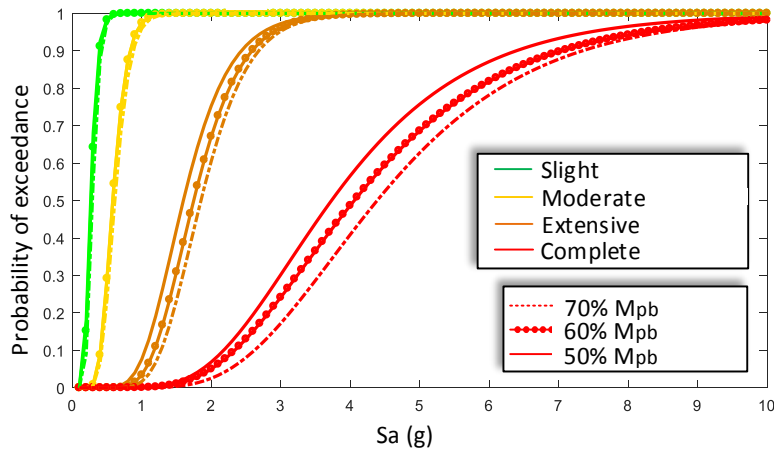


**Figure 5.9 Fragility curves for FEMA-P695 ground-motion record set for all the analysis models**

### 5.3.4.2. Selected Mainshocks

The results from the set of selected mainshocks (only mainshocks) i.e. total 22 earthquake records are compared with the fragility curves developed from the ground-motion record set given

by FEMA-P695 [22]. Acceptable agreements are shown between the fragility curves produced using both set of records as will be shown later. Based on these results, the fragility curves developed using the selected mainshocks can be considered as the benchmark results (similar to the fragility curves developed using the FEMA-P695 records) and can be compared with the fragility curves developed for the mainshock-aftershock sequences later. Figure 5.10 show the fragility curves for all three frame models while Figure 5.11 show the fragility comparisons for all three models.

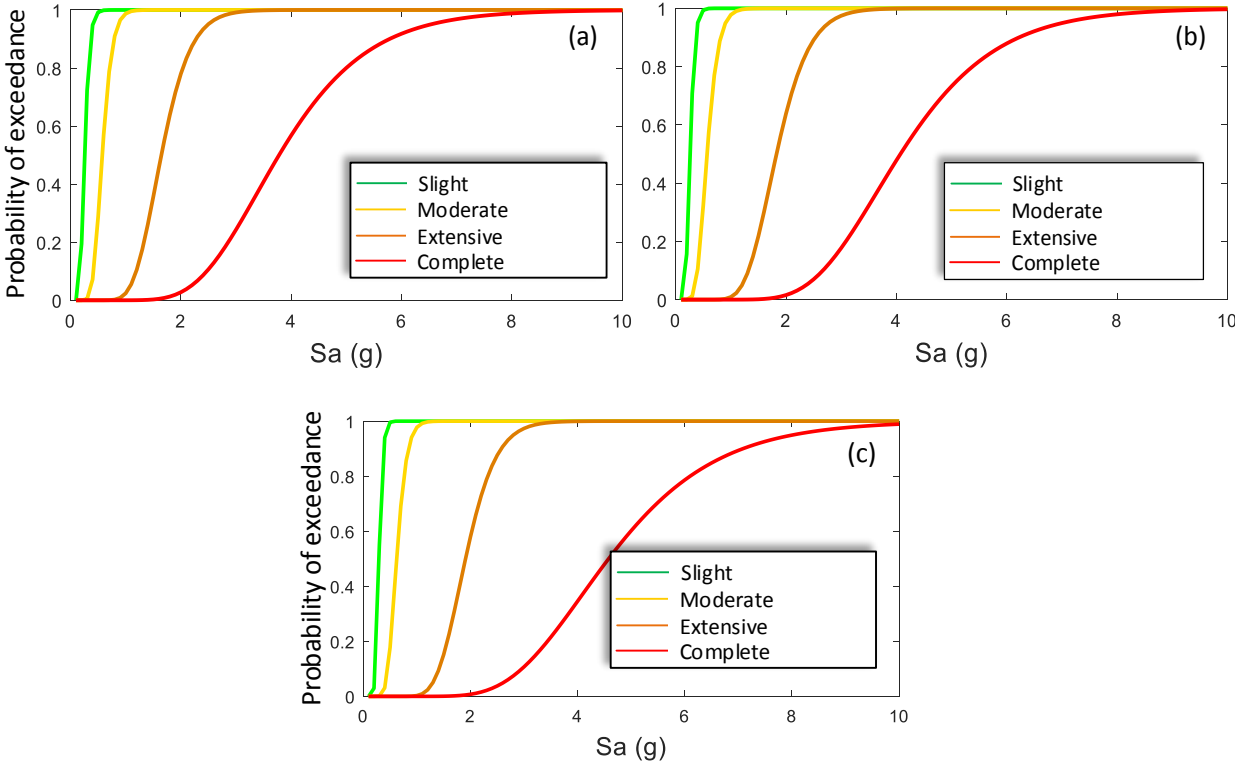


**Figure 5.10 Fragility curves for selected mainshocks (a) 50% $M_{pb}$  Model Frame, (b) 60% $M_{pb}$  model frame, (c) 70% $M_{pb}$  model frame**

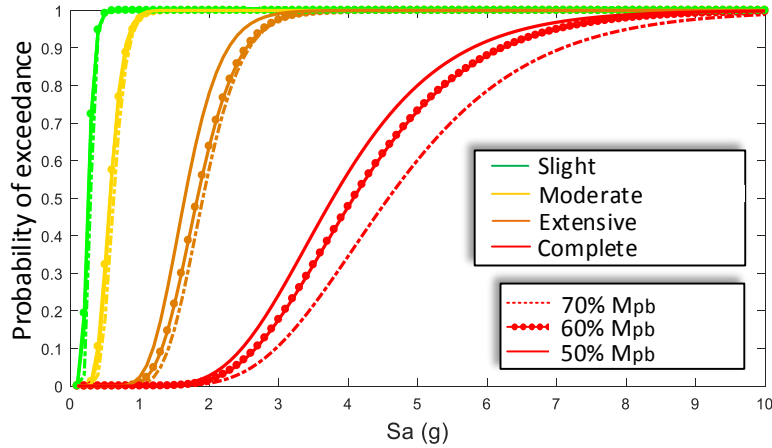


**Figure 5.11 Fragility curves for selected mainshocks for all the analysis models**

### 5.3.4.3. Mainshock – Aftershock sequences

In this record set, the consecutive aftershocks after the mainshocks (selected mainshocks record set) are also employed. The details of the ground-motion set and the scaling procedure is described in section 4.5.1. In the analysis using the mainshock-aftershock sequences, the mainshocks damage the structure up-to a particular damage state. Then with a gap of 40 seconds in the input ground motion, the structure is brought to steady state (after the conclusion of the mainshock when the structure stops oscillating). Only when the structure stops oscillating, the aftershocks excitations are then applied to the structure.

The behavior of the structures only due to the aftershocks is monitored in the IDA and from those results, the fragility curves are developed. Therefore, the results presented below show the structural behavior only in the aftershocks i.e. if the displacement of the structure is greater in mainshock than that of the aftershock, then the maximum displacement of the structure in the aftershocks is considered to assess the results. Figure 5.12 show the fragility curves for the models with connection capacity  $50\%M_{pb}$ ,  $60\%M_{pb}$  and  $70\%M_{pb}$ , respectively.

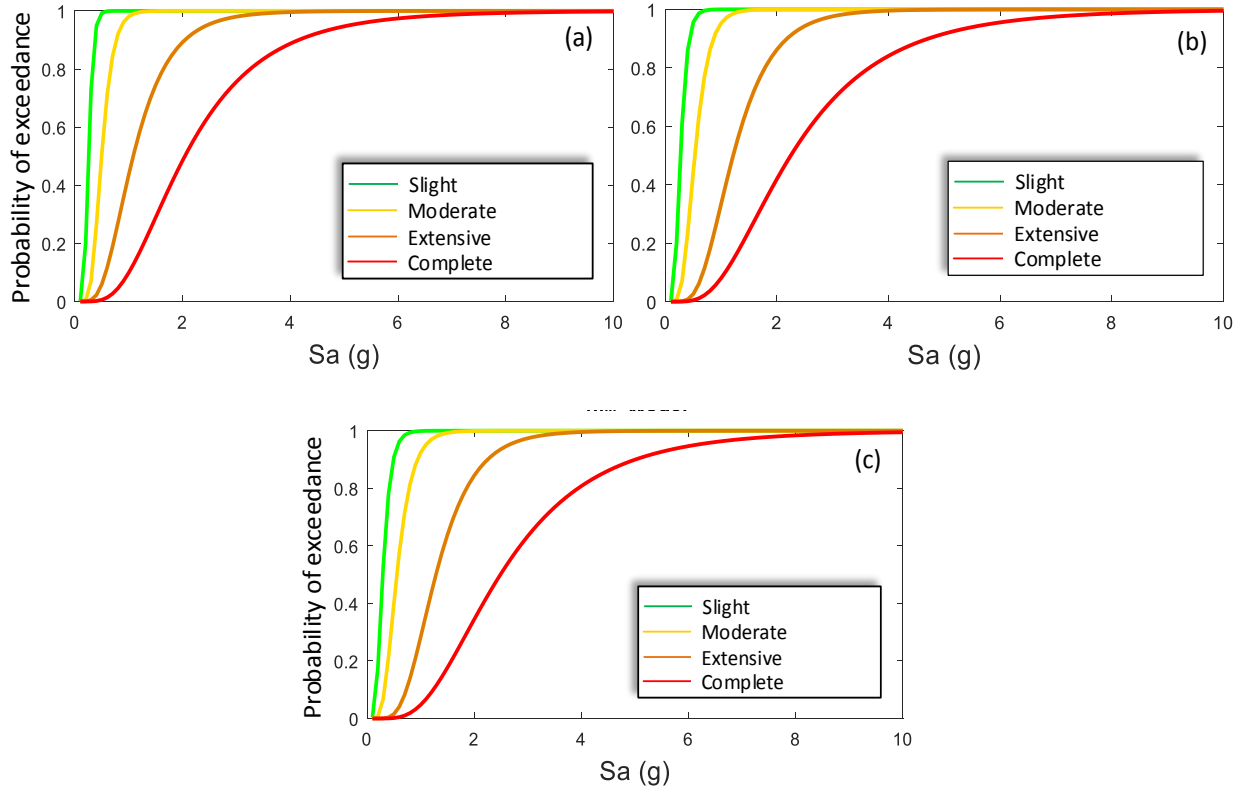


Figure 5.12 Fragility curves for mainshock-aftershock sequences (a) 50%  $M_{pb}$  Model Frame, (b) 60%  $M_{pb}$  Model Frame, (c) 70%  $M_{pb}$  Model Frame

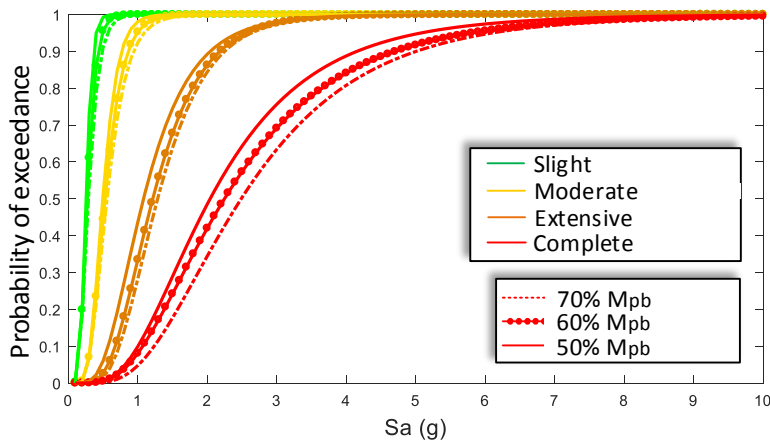


Figure 5.13 Fragility Curves for mainshock-aftershock sequences for all analysis models

#### 5.4. Assessment of Fragility Function Parameters

The fragility curve, also known as the Lognormal Collapse Fragility Function is defined using two parameters. The first parameter is the median ' $S_a$ ', which is the ' $S_a$ ' at which 50% of ground

motions causes collapse. This is called the ‘Median Collapse Intensity’ or ‘Median Collapse Capacity’. The second parameter is the standard deviation of the natural logarithm ( $\log(S_a)$ ), which is known as ‘ $\beta_{RTR}$ ’. The standard deviation ( $\beta_{RTR}$ ) is used to measure the slope of the lognormal distribution and to assess the distribution of the results because of the variability in the records i.e. record-to-record (RTR) variability.

#### **5.4.1. FEMA-P695 Ground Motion Record Set**

Figure 5.14 (a), (b) and (c) show the fragility curves for this set of ground-motions for the model frame with connection capacity equal to  $70\%M_{pb}$ ,  $60\%M_{pb}$  and  $50\%M_{pb}$ , respectively, along with the fragility function parameters. Table 5.5 summarizes the fragility function parameters i.e. Median Collapse capacity and Standard deviation together for all the model frames.

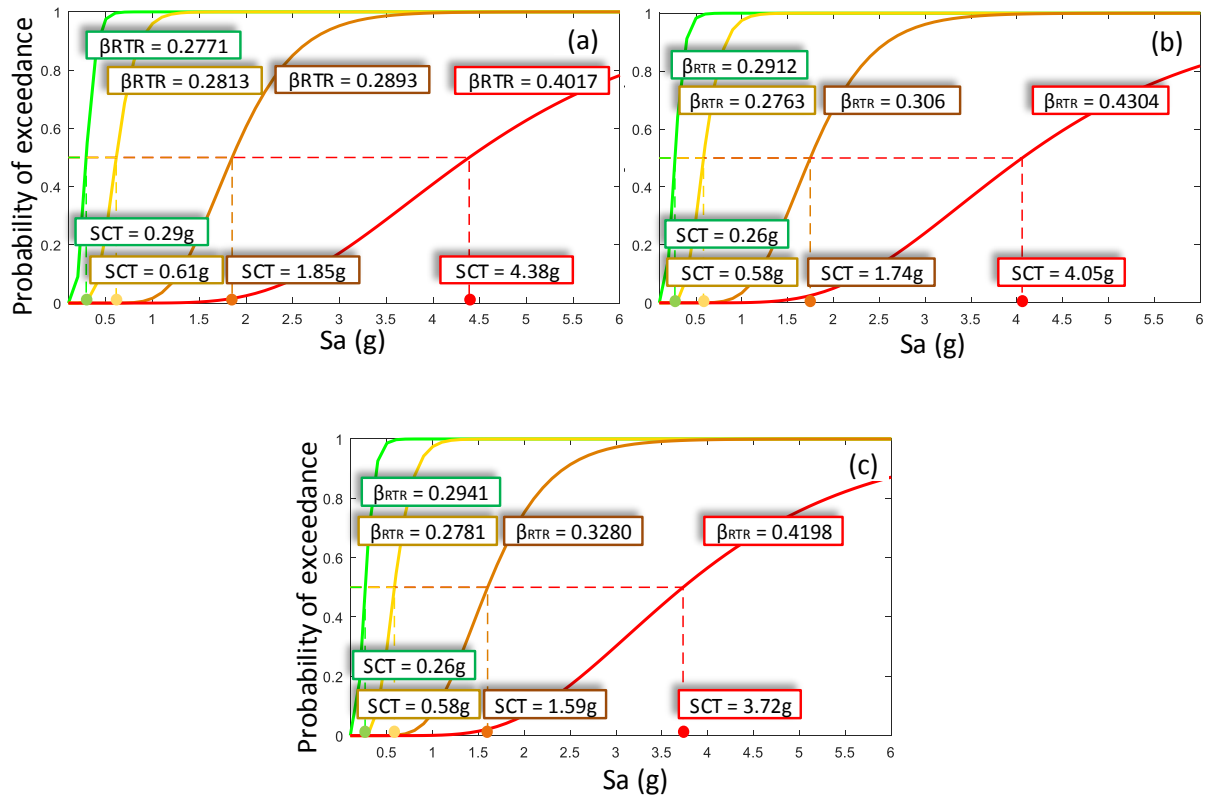


Figure 5.14 Fragility curves and fragility function parameters for FEMA-P965 ground-motions record set (a) 70% $M_{pb}$  model frame, (b) 60% $M_{pb}$  model frame and (c) 50% $M_{pb}$  model frame

Table 5.5 Fragility Function Parameters for model frames under FEMA-P965 Ground-motions Record Set

Damage State	Median Collapse Capacity			Standard Deviation ( $\beta_{RTR}$ )		
	70% $M_{pb}$	60% $M_{pb}$	50% $M_{pb}$	70% $M_{pb}$	60% $M_{pb}$	50% $M_{pb}$
Slight	0.2896	0.2697	0.2614	0.2771	0.2912	0.2941
Moderate	0.6107	0.5817	0.5808	0.2813	0.2763	0.2781
Extensive	1.8508	1.7462	1.5977	0.2893	0.3060	0.3280
Complete	4.3872	4.0580	3.7298	0.4017	0.4304	0.4198

### 5.4.2. Selected Mainshocks Ground-motion Records

Figure 5.15 (a), (b) and (c) show the fragility curves for this set of ground-motions for the model frame with connection capacity equal to  $70\%M_{pb}$ ,  $60\%M_{pb}$  and  $50\%M_{pb}$  along with the fragility function parameters. Table 5.6 summarizes the fragility function parameters i.e. Median Collapse Capacity and Standard deviation together for all the model frames.

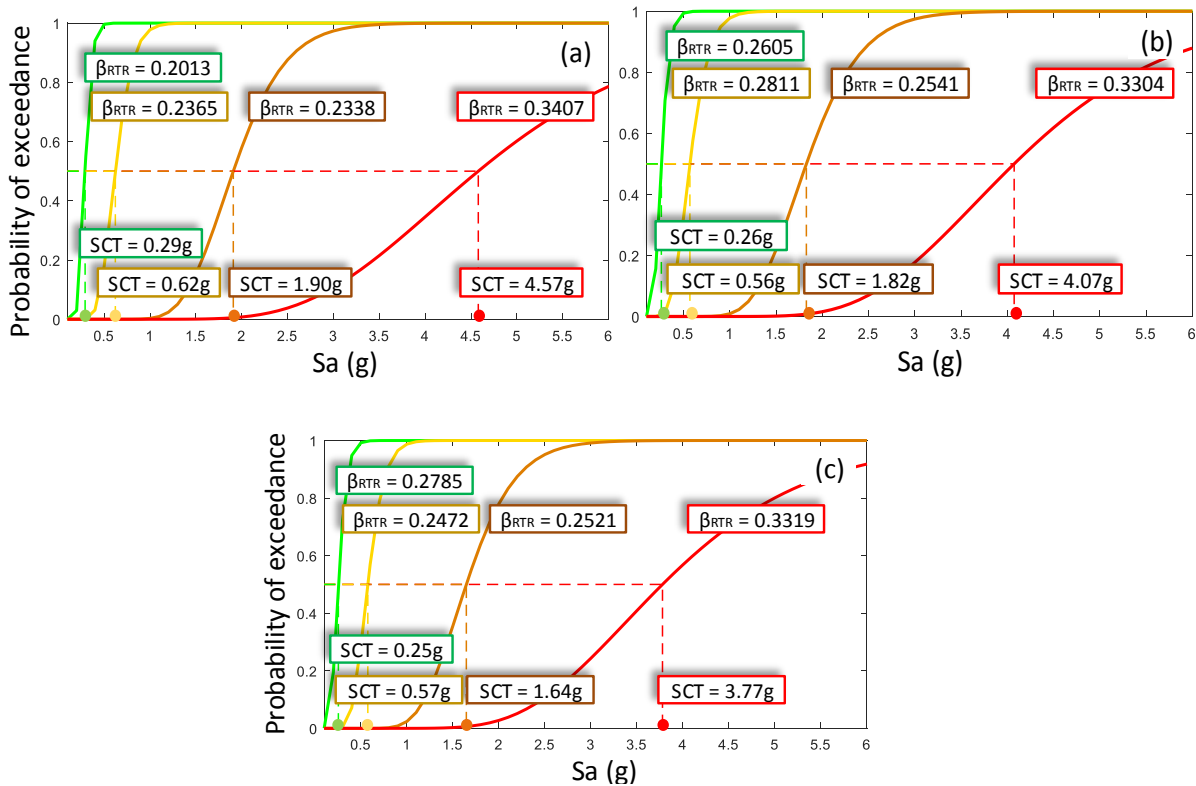


Figure 5.15 Fragility curves and fragility function parameters for selected mainshocks ground-motion record set (a)  $70\%M_{pb}$  model frame, (b)  $60\%M_{pb}$  model frame and (c)  $50\%M_{pb}$  model frame

Table 5.6 Fragility function parameters for model frames under selected mainshocks ground-motion record set

Damage State	Median Collapse Capacity			Standard Deviation ( $\beta_{RTR}$ )		
	70% $M_{pb}$	60% $M_{pb}$	50% $M_{pb}$	70% $M_{pb}$	60% $M_{pb}$	50% $M_{pb}$

Slight	0.2925	0.2601	0.2543	0.2013	0.2605	0.2785
Moderate	0.6220	0.5688	0.5745	0.2365	0.2811	0.2472
Extensive	1.9079	1.8280	1.6456	0.2338	0.2541	0.2521
Complete	4.5784	4.0746	3.7782	0.3407	0.3304	0.3319

### 5.4.3. Mainshock-Aftershock Sequences

Figure 5.16 (a), (b) and (c) show the fragility curves for this set of ground-motions for the model frame with connection capacity equal to  $70\%M_{pb}$ ,  $60\%M_{pb}$  and  $50\%M_{pb}$  along with the fragility function parameters. Table 5.7 summarizes the fragility function parameters i.e. Median Collapse capacity and Standard deviation together for all the model frames.

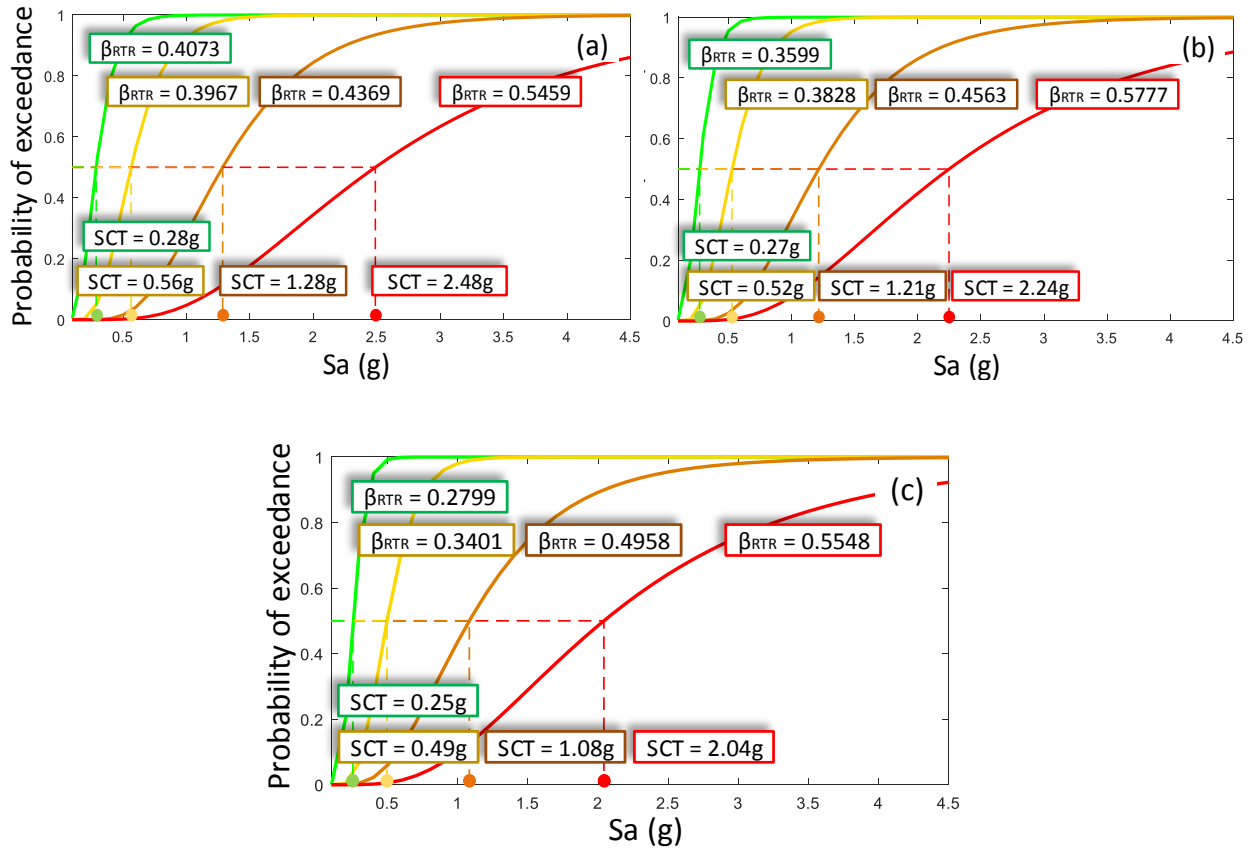


Figure 5.16 Fragility curves and fragility function parameters for mainshock-aftershock sequences (a) 70%  $M_{pb}$  model frame, (b) 60%  $M_{pb}$  model frame and (c) 50%  $M_{pb}$  model frame

Table 5.7 Fragility Parameters for model frames under selected Mainshock-Aftershock Sequences

Damage State	Median Collapse Capacity (SCT)			Standard Deviation ( $\beta_{RTR}$ )		
	70% $M_{pb}$	60% $M_{pb}$	50% $M_{pb}$	70% $M_{pb}$	60% $M_{pb}$	50% $M_{pb}$
Slight	0.2885	0.2711	0.2528	0.4073	0.3599	0.2799
Moderate	0.5637	0.5274	0.4956	0.3967	0.3828	0.3401
Extensive	1.2853	1.2148	1.0822	0.4369	0.4563	0.4958
Complete	2.4886	2.2473	2.0411	0.5459	0.5777	0.5548

## 5.4.4. Comparison of Fragility Curves

### 5.4.4.1. FEMA-P695 Ground-motion Set and Selected Mainshocks Record Set

In this study, a new set of ground-motions is proposed, consisting of only 11 earthquake events (22 components) where every earthquake event has at least one aftershock (see Table B.4 to Table B.9). The sequence of mainshock and aftershock events allow for the evaluation of frame response under the mainshock then under the mainshock-aftershock sequences. However, the validity of these records needs to be established. Therefore, the fragilities produced using the mainshocks of the 11 earthquake events should be weighed against the fragilities developed using the FEMA P695 set. Following set of figures show such comparison for each damage state along with the ‘Median Collapse Intensity’. Figure 5.17, Figure 5.18, Figure 5.19 show the comparison between the fragility results for the three model frames. As observed, acceptable agreement between the two sets of fragilities is shown.

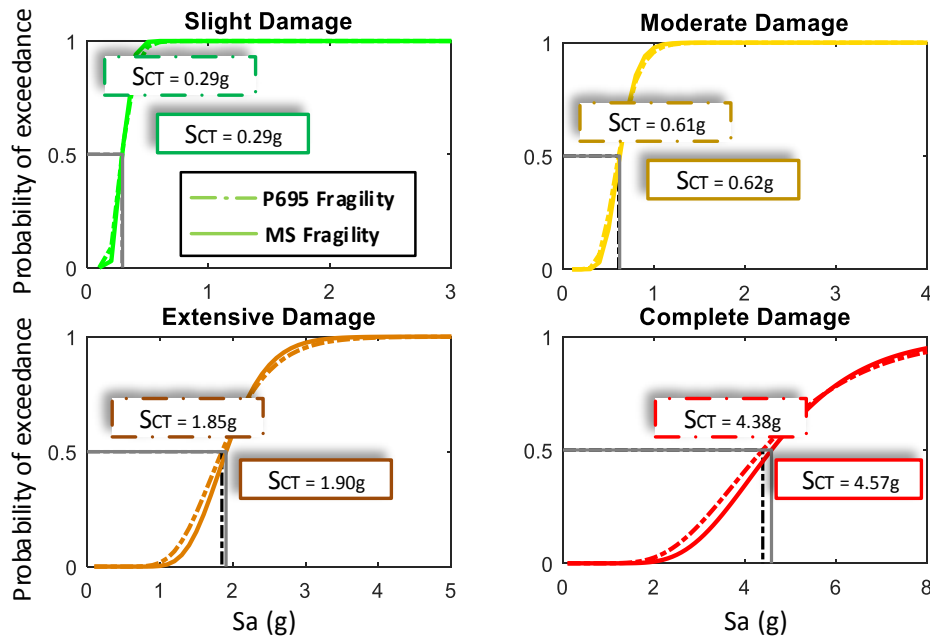


Figure 5.17 Comparison of fragility curves for 70% Model frame under FEMA-P695 ground-motion set and selected mainshocks record Set

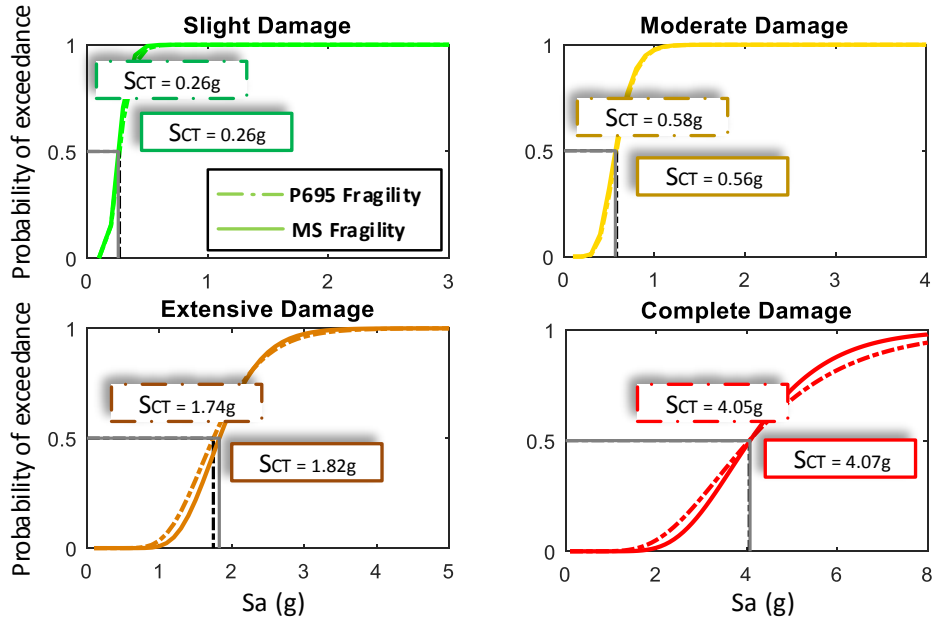


Figure 5.18 Comparison of fragility curves for 60% Model frame under FEMA-P695 ground-motion set and selected mainshocks record Set

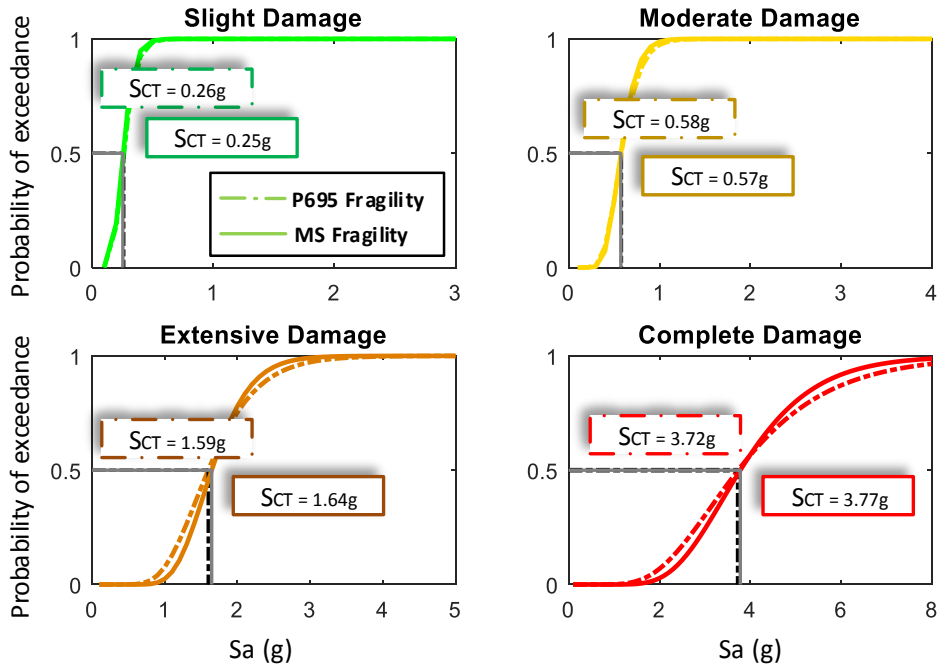


Figure 5.19 Comparison of fragility curves for 50% Model frame under FEMA-P695 ground-motion set and selected mainshocks record Set

#### **5.4.4.2. Selected Mainshock record set and Set of Mainshock-Aftershock Sequences**

From the above comparison between the fragility results from standard set of earthquakes and the new proposed set of earthquakes, it can be said that the new proposed set of earthquakes gives not exactly the same but approximate results as the standard set of earthquakes in FEMA P695. After comparing the fragility results for two ground-motion record sets i.e. FEMA-P695 Ground-motions record set and the record set of selected mainshocks, the results from the later ground-motion set (selected mainshocks) is now compared with the fragility results from the record set of mainshock-aftershock sequences.

In the fragility results from the mainshock-aftershock sequences, it is observed that the probability of exceedance for each damage state is increased, particularly for extensive and complete limit states. This is because of the residual drift experienced by the structure due to the initial mainshock which makes the structure more vulnerable to damage or collapse when subjected to the aftershock. Figure 5.20, Figure 5.21 and Figure 5.22 show comparison between the fragility results for the model frames under the two said ground-motion sets in terms of the respective Median Collapse Intensity for each damage state.

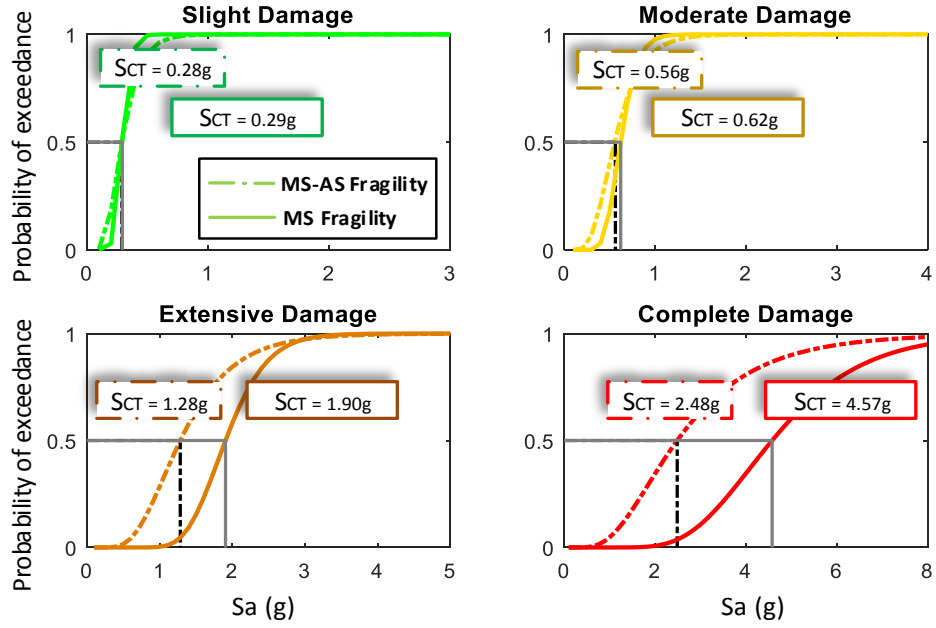


Figure 5.20 Comparison of fragility curves for 70% model frame under selected mainshocks record set and record set of mainshock-aftershock Sequences

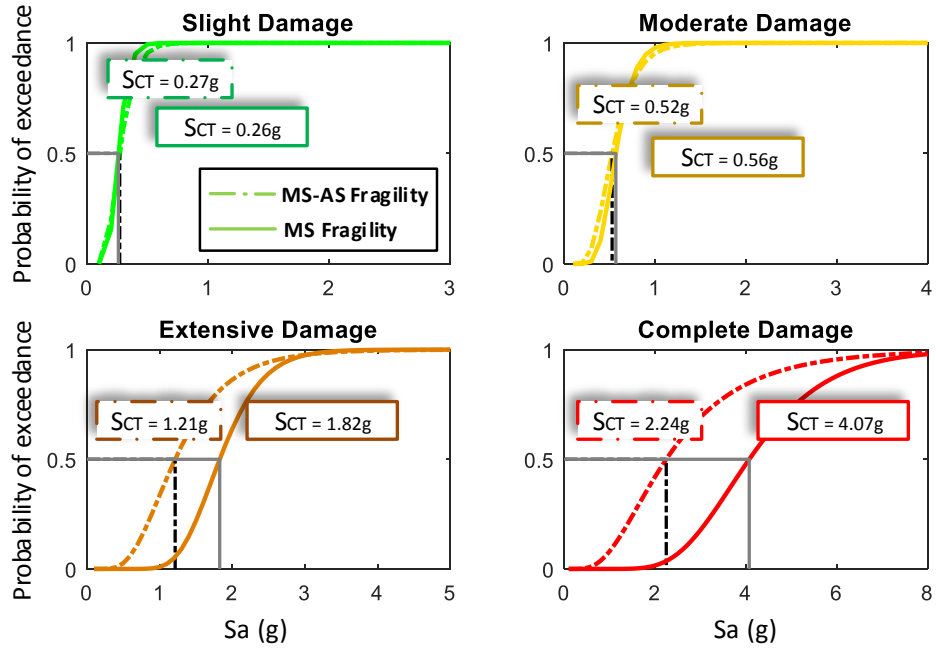
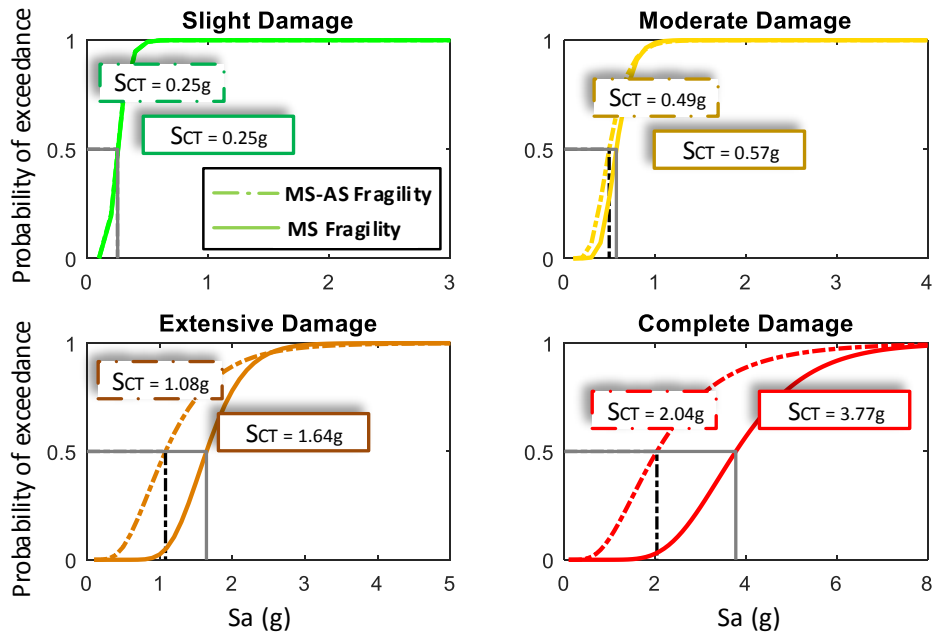


Figure 5.21 Comparison of fragility curves for 60% model frame under selected mainshocks Record Set and record set of mainshock-aftershock Sequences



**Figure 5.22 Comparison of fragility curves for 50% model frame under selected mainshocks record Set and record set of mainshock-aftershock sequences**

## 5.5. Period Elongation

Using Short-term Fourier Transformations on the top-story displacement history of the structure under the three sets of earthquakes, the changing fundamental period of the structure is evaluated. Figure 5.23 (a) shows the response of the model frame with connection capacity equal to  $70\%M_{pb}$  under the earthquake ‘Umbria Marche\_ Italy’ at the spectral intensity ( $S_a$ ) equal to ‘0.5g’ (see Table B.1 for details). Figure 5.23 (b) shows the spectrogram and the calculated frequency along the time and Figure 5.23(c) shows the calculated period along the time simply by inverting the frequency values. The figures show that when the structure is undamaged i.e. before the mainshock starts at  $t = 0$  seconds, the observed period is equal to the calculated fundamental period using the eigenvalue analysis which is 0.615 seconds. The period then fluctuates as shown in Figure 5.23 (c) as time progresses. The mean elongated period of the structure is calculated to be 0.70 seconds.

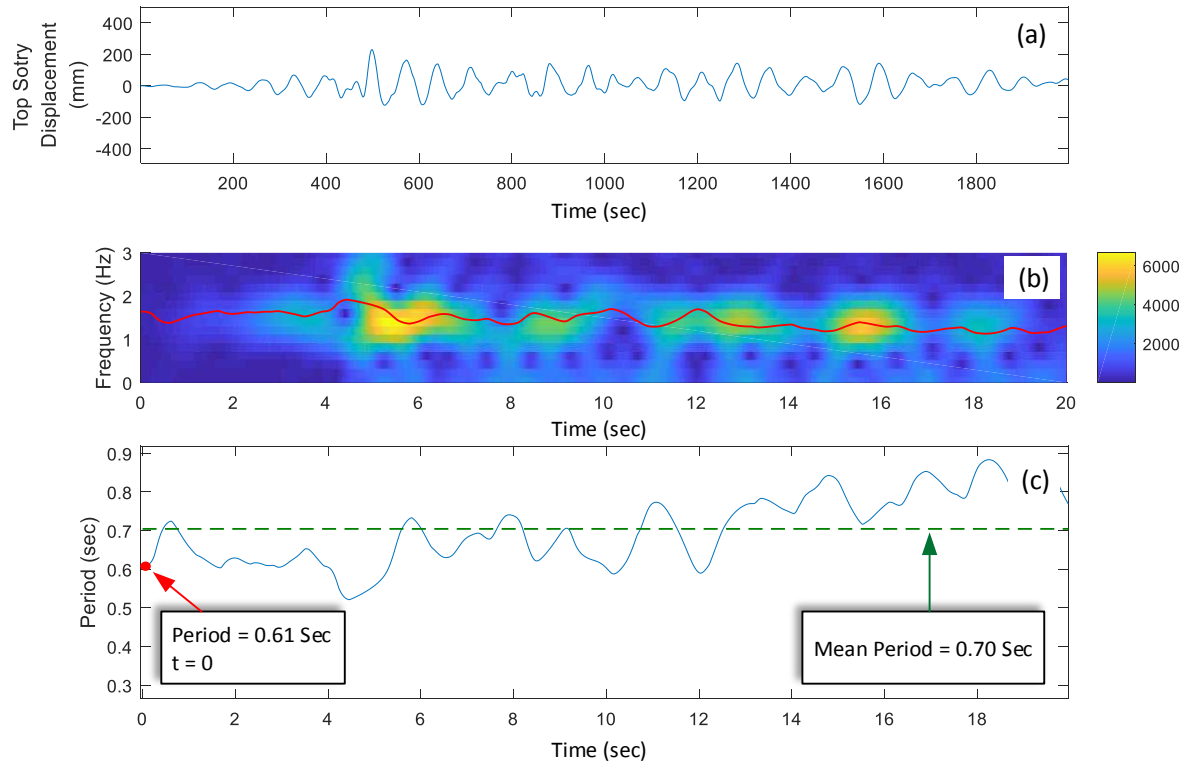


**Figure 5.23 (a) Structural response of 70% $M_{pb}$  model frame in terms of ‘top-story displacement’, (b) Spectrogram of the response with the tracked frequency of the structure and (c) Changing period of the structure and the mean elongated period**

Following illustrate the same procedure with the remaining model frames i.e. the frames with the connection capacity equal to 60% $M_{pb}$  and 50% $M_{pb}$ , respectively. Figure 5.24 (a) shows the response of the frame with connection capacity equal to 60% $M_{pb}$  and Figure 5.24 (b) shows the spectrogram of the same and the period content along the time. Figure 5.24 (c) shows the changing period of the structure as a function of time. It can be observed that at time  $t = 0$ , the period of the frame is equal to the fundamental period, which is 0.63 seconds (see Figure 5.4), and the average inelastic period or elongated period of the structure is calculated as 1.24 seconds.

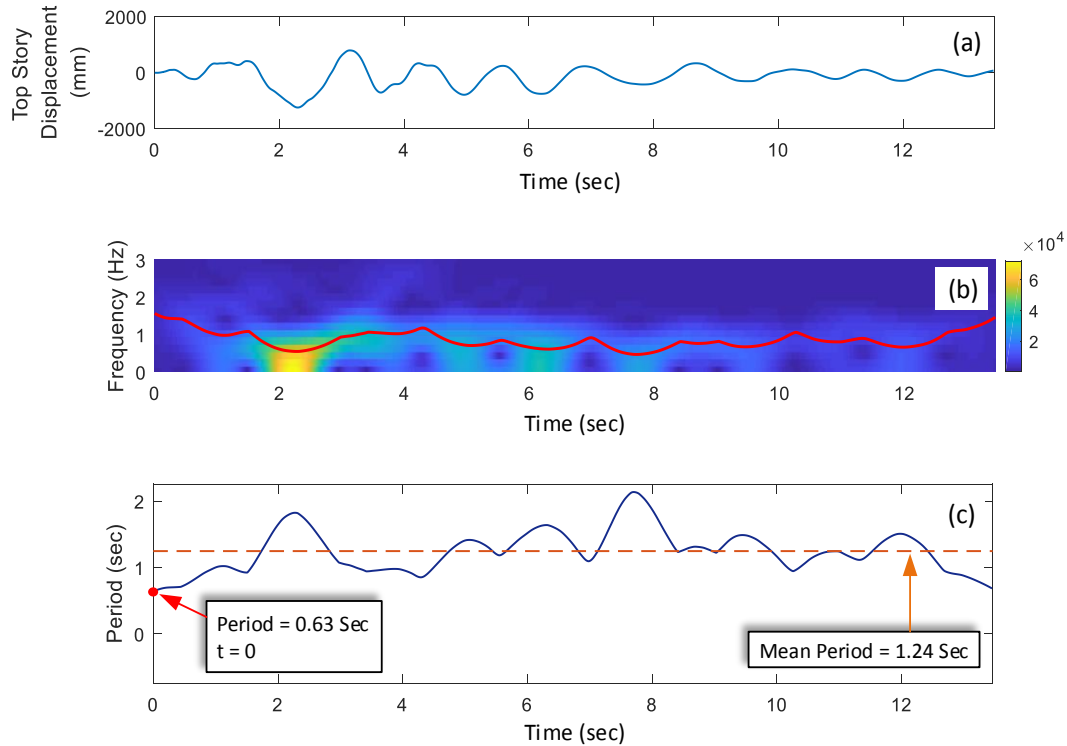


**Figure 5.24 (a) Structural response of 60% $M_{pb}$  model frame in terms of ‘top-story displacement’, (b) Spectrogram of the response with the tracked frequency of the structure and (c) Changing period of the structure and the mean elongated period**

Similarly, Figure 5.25 shows the results for the model frame with connection capacity equal to 50% $M_{pb}$ . In Figure 5.25 (c), it is also observed that the period of the frame when  $t = 0$ , is equal to the fundamental period of the structure i.e. 0.65 seconds, and the elongated period is 1.26 seconds which is an average value of the periods.

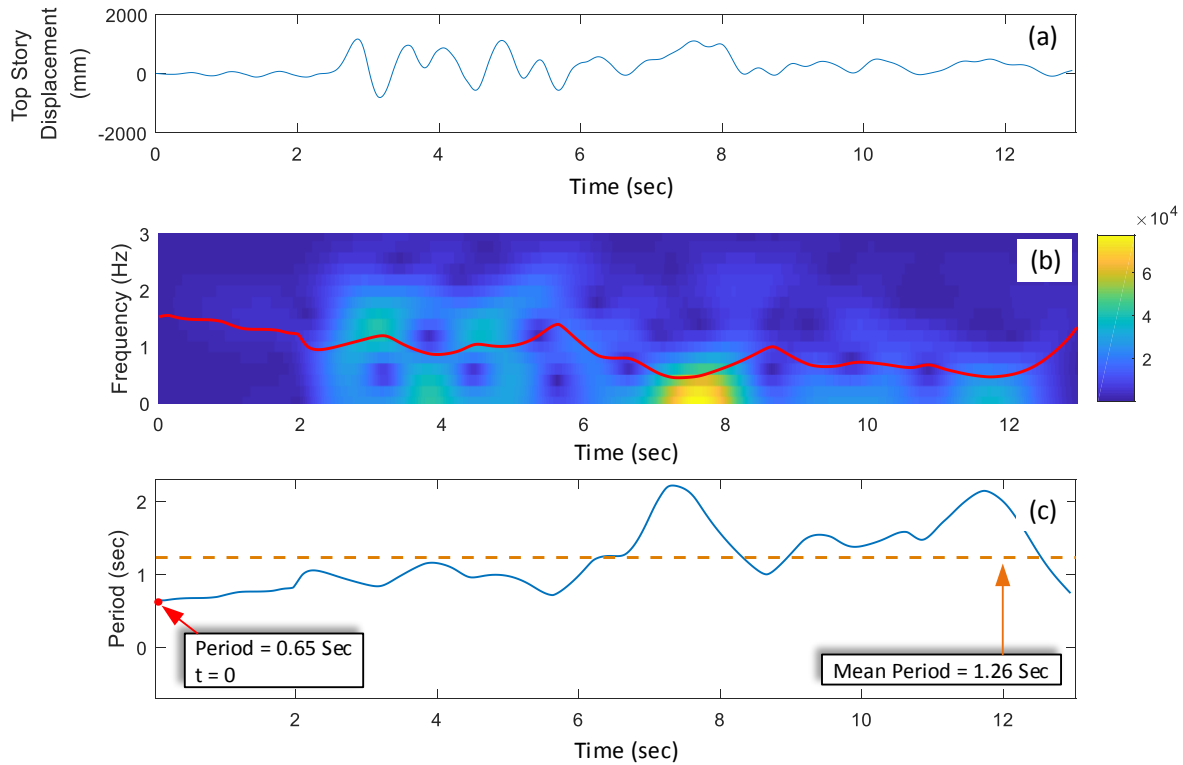


**Figure 5.25 (a) Structural response of 50% $M_{pb}$  model frame in terms of ‘top-story displacement’, (b) Spectrogram of the response with the tracked frequency of the structure and (c) Changing period of the structure and the mean elongated period**

Figure 5.26 and Figure 5.27 show the actual variability of the elongated period with the respective connection capacity and the relationship between the period elongation and the connection capacities of the structure for the mainshocks and the aftershocks at the spectral intensity  $S_a = 1g$  and  $2g$ . The relationship between the elongated period and the connection capacity is developed and represented by trend-line just and also analyzed by computing the mean and standard deviation of the distribution just to develop an idea or a trend of the variation of the period-elongation and the respective connection capacity.

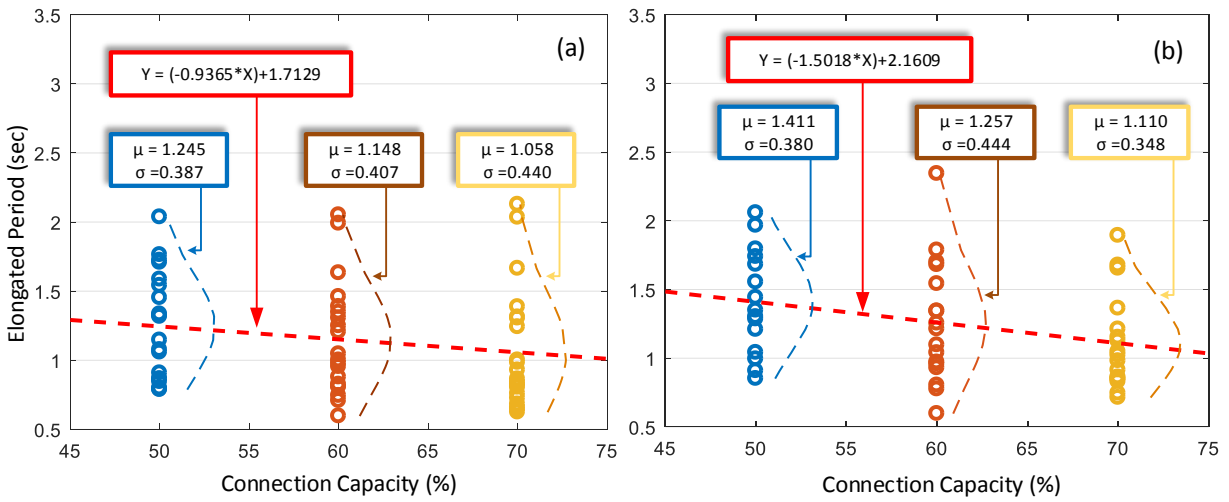


**Figure 5.26 Elongated period and the respective connection capacity and the relationship between them for mainshocks at (a) spectral acceleration  $S_a = 1g$  and (b) spectral acceleration  $S_a = 2g$**

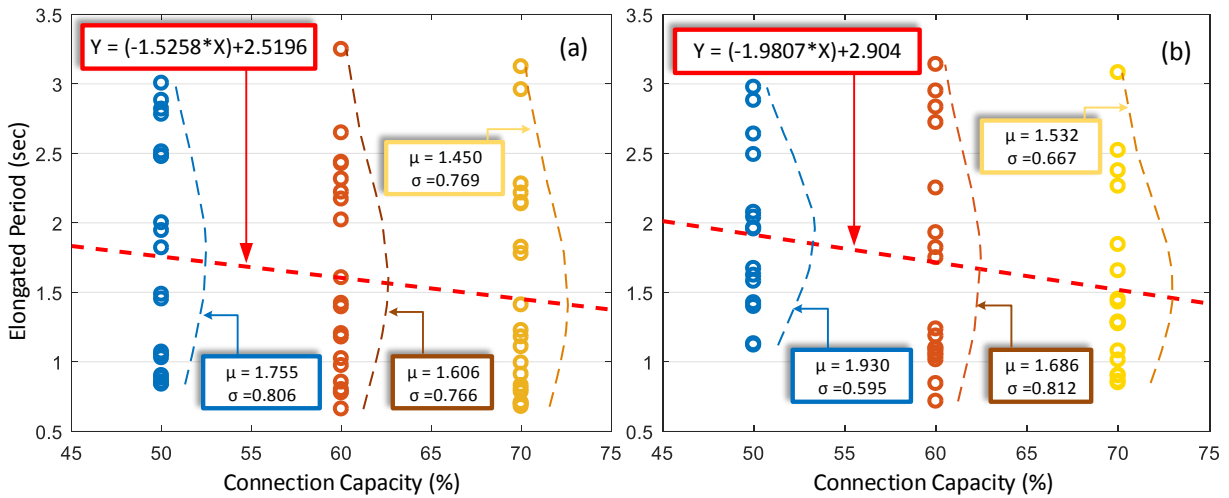


**Figure 5.27 Elongated period and the respective connection capacity and the relationship between them for aftershocks at (a) spectral acceleration  $S_a = 1g$  and (b) spectral acceleration  $S_a = 2g$**

## CHAPTER 6. SUMMARY AND CONCLUSIONS

### 6.1. Summary of current work

Semi-rigid steel moment frames were modeled using 1D line elements to represent beam and column sections and zero length spring elements to represent extended end-plate connections. Three 2D models were developed with three different connection capacities by incorporating different moment rotation curves. Seismic assessment of the semi-rigid steel moment frames were assessed using pushover, eigenvalue, incremental dynamic analysis, and frequency domain analysis. The pushover analysis was performed to evaluate essential seismic performance characteristics including design base shear, ductility ratio, and the over-strength factor. The eigenvalue analysis was conducted to calculate the fundamental period of the structure. The incremental dynamic analysis was used to develop fragility functions representing the various damage limits in the structures subjected to mainshock-aftershock sequences. The results of the non-linear dynamic analysis were also used to investigate the extent and progression of period elongation in the frames when subjected to the seismic loads.

The mainshock-aftershock sequence ground motions used in the dynamic analysis were selected based on a newly devised methodology for both the selection and the scaling process. The standard set of earthquakes given comprise of 44 mainshock records only. The new set of earthquakes consists of only of 22 earthquake records along with their naturally recorded aftershocks (available on PEER-NGA database). Some of these records are part of the standard 44 records given in FEMA-P695 while the remainder are not. The validity of the new record set was

ensured through comparing the fragility function produced using this new set to those produced exclusively using the 44 records in FEMA-P695.

In this study, the inelastic period of the structures, including period elongation, was also investigated by using ‘Short Term Fourier Transformation’. In incremental dynamic analysis (IDA) different intensities of earthquake are incorporated, causing various levels of damage and deterioration in the connections and, reduction in the overall system stiffness, and increase in the fundamental period of the structure. The elongated period of the frames was obtained at spectral intensities equal to 1g and 2g for each mainshock and for each aftershock separately to develop a relationship between the connection capacity and elongated period at two said spectral intensities.

## **6.2. Conclusions**

The following are the main conclusions in the study:

- The use of non-linear behavior of the connections instead of using fully-restrained of pinned behavior resulted into more accurate response of the frames.
- A methodology to create and scale a sequence of mainshock and aftershock was discussed and a relationship was developed in terms of the PGA values to scale the aftershock with respect to its mainshock.
- After comparison of the fragility curves from the two sets of earthquake records i.e. standard set given in FEMA-P695 and new proposed set, it was observed that the new set yields considerably the same results. Therefore the fragility curves from the latter set can be compared to the fragility curves obtained from the aftershocks records.

- Being consisted of only 22 earthquake records, the new proposed set takes less time (than standard set with 44 earthquake records) to perform incremental dynamic analysis and to develop fragility curves.
- By comparing the mainshock fragilities to the aftershock fragilities, it can be concluded that probability of exceeding 'slight' and 'moderate' damages states was not increased when frames which were damaged slightly and moderately in mainshocks were analyzed in corresponding aftershocks.
- The probability of exceeding the 'extensive' and 'complete' damage states due to the aftershocks was substantially increased.
- A methodology was developed to track the changing period of the structure by transforming its top-story response using 'Short-Term Fourier Transformation (STFT)' and is shown to yielding accurate results by obtaining period of the frame at  $t = 0$  sec that is equal to the fundamental period of the frame.
- A relationship between the connection capacities and the elongated period of the frame at different spectral intensities was developed and the distribution of the elongated period for respective frame (i.e. respective connection capacity) was further analyzed and compared by calculating its mean and standard deviation.

## REFERENCES

- [1] H. Krawinkler 2000 System performance of steel moment resisting frame structures 1–8
- [2] Roeder C W PERFORMANCE OF MOMENT-RESISTING CONNECTIONS 1–8
- [3] Rodgers J E and Mahin S A 2004 Effects of Connection Hysteretic Degradation on the Seismic Behavior of Steel Moment-Resisting Frames Effects of Connection Hysteretic Degradation on the Seismic Behavior of Steel Moment-Resisting Frames
- [4] Luco N and Cornell C A 1998 Effects of random connection fractures on the demands and reliability for a 3-story pre-Northridge SMRF structure *6th U.S. Natl. Conf. Earthq. Eng.* 1–12
- [5] Kanvinde A M and Deierlein G G 2004 Prediction of ductile fracture in steel moment connections during earthquakes using micromechanical fracture models *Proc. 13th World Conf. Earthq. Eng.*
- [6] Peng C 2005 Effect of weld on design of steel moment-resisting connection reinforced with steel plates © 12 274–7
- [7] Goel S, Lee K and Stojadinovic B 2000 Development of Post-Northridge Steel Moment Connections *Proc. 12th World Conf. Earthq. Eng. Auckland, New Zeal. Paper No.* 1–8
- [8] Mahmoud H N, Elnashai A S, Spencer B F, Kwon O-S and Bennier D J 2013 Hybrid Simulation for Earthquake Response of Semirigid Partial-Strength Steel Frames *J. Struct.*

*Eng.* **139** 1134–48

- [9] Elnashai AS D S L Fundamentals of earthquake engineering, UK *John Wiley Sons*; 2008.
- [10] Faridmehr I, Tahir M M, Lahmer T and Osman M H 2012 Seismic Performance of Steel Frames with Semi-Rigid Connections *15th World Conf. Earthq. Eng.* **2017** 1–10
- [11] Elnashai A S and Elghazouli A Y 1994 Seismic behaviour of semi-rigid steel frames *J. Constr. Steel Res.* **29** 149–74
- [12] Dogramaci Aksoylar N, Elnashai A S and Mahmoud H 2012 Seismic Performance of Semirigid Moment-Resisting Frames under Far and Near Field Records *J. Struct. Eng.* **138** 157–69
- [13] Aksoylar N D, Elnashai A S and Mahmoud H 2011 The design and seismic performance of low-rise long-span frames with semi-rigid connections *J. Constr. Steel Res.* **67** 114–26
- [14] Ruiz-García J and Negrete-Manriquez J C 2011 Evaluation of drift demands in existing steel frames under as-recorded far-field and near-fault mainshock-aftershock seismic sequences *Eng. Struct.* **33** 621–34
- [15] Li Q and Ellingwood B R Performance Evaluation and Damage Assessment of Steel Frame Buildings under Mainshock-Aftershock Sequences *Earthq. Eng. Struct. Dyn.* **36** 405–27
- [16] Hatzigeorgiou G D and Liolios A A 2010 Nonlinear behaviour of RC frames under repeated strong ground motions *Soil Dyn. Earthq. Eng.* **30** 1010–25
- [17] Ruiz-Garcia J, Moreno J Y and Maldonado I a 2008 Evaluation of existing Mexican

- Highway Bridges Under Mainshock-Aftershock Seismic Sequences *Proc. 14th World Conf. Earthq. Eng.*
- [18] Mahin S A 1980 Effects of duration and aftershocks on inelastic design earthquakes *Proc. 7th world Conf. Earthq. Eng.* **5** 677–80
- [19] Kiremidjian A S and Sunasaka Y 1993 *A METHOD FOR STRUCTURAL SAFETY EVALUATION UNDER MAINSHOCK -AFTERSHOCK EARTHQUAKE SEQUENCES*
- [20] Qian J, Huang W and Fu Q S 2012 Damage Assessment of RC Frame Structures under Mainshock-Aftershock Seismic Sequences *15th World Conf. Earthq. Eng.* **449** 739–44
- [21] Ghobarah A 2001 Performance-based design in earthquake engineering: State of development *Eng. Struct.* **23** 878–84
- [22] ATC 2009 Quantification of building seismic performance factors *Fema P695* 421
- [23] Clough, Ray W. J P *Dynamics of Structures* (Computers and Structures, Inc)
- [24] Tsompanakis Y 2014 *Earthquake Return Period and Its Incorporation into Seismic Actions* vol 9
- [25] Frye M J and Morris G A 1975 Analysis of Flexibly Connected Steel Frames *Can. J. Civ. Eng.* **2** 280–91
- [26] Picard A, Giroux Y M and Brun P 1976 Discussion of analysis of flexibly connected steel frames *Can. J. Civ. Eng.* **3(2)**
- [27] Prabha P, Marimuthu V, Saravanan M, Surendran M and Palani G S 2007 Effect of Air

Gap on the Behavior of Double Web Angle Connections 30–5

- [28] Ramberg W and Osgood W R Description of stress-strain curves by three parameters  
(*Technical Note No. 902*) *Natl. Advis. Comm. Aeronaut. Washingt. DC.*
- [29] Ang K M and Morris G A 1984 Analysis of three-dimensional frames with flexible beam-column connections *Can. J. Civ. Eng.* **11** 245–54
- [30] Stein R S 1999 The role of stress transfer in earthquake occurrence : Abstract : *Nature*  
*Nature* **402** 605–9
- [31] Yamanaka Y and Shimazaki K 1990 Scaling relationship between the number of aftershocks and the size of the main shock *J. Phys. Earth* **38** 305–24
- [32] Båth M 1965 Lateral inhomogeneities of the upper mantle *Tectonophysics* **2** 483–514
- [33] Felzer K R, Becker T W, Abercrombie R E, Ekström G and Rice J R 2002 Triggering of the 1999  $M_w$  7.1 Hector Mine earthquake by aftershocks of the 1992  $M_w$  7.3 Landers earthquake *J. Geophys. Res. Solid Earth* **107**ESE 6-1-ESE 6-13
- [34] Zakharova O, Hainzl S and Bach C 2013 Seismic moment ratio of aftershocks with respect to main shocks *J. Geophys. Res. Solid Earth* **118** 5856–64
- [35] Song R, Li Y and Van De Lindt J W 2016 Loss estimation of steel buildings to earthquake mainshock-aftershock sequences *Struct. Saf.* **61** 1–11
- [36] Yin Y-J and Li Y 2011 Loss Estimation of Light-Frame Wood Construction Subjected to Mainshock-Aftershock Sequences *J. Perform. Constr. Facil.* **25** 504–13

- [37] Gutenberg B R C Seismicity of the earth and associated phenomena *Princeton, NJ Princet. Univ. Press. 1949*
- [38] EERI Learning from earthquakes: the Mw 6.4 and Mw 6.3 Iran Earthquakes of August 11, 2012. *EERI Spec. Earthq. Report. Earthq. Eng. Res. Institute; 2012.*
- [39] Parker M and Steenkamp D 2012 The economic impact of the Canterbury earthquakes major earthquakes *Reserv. Bank New Zeal. Bull. 75* 13–25
- [40] Risk Management Solutions 2010 The 2010 Maule, Chile Earthquake: Lessons and Future Challenges *Risk Manag. Solut. Inc.* 1–46
- [41] Song R, Li Y and van de Lindt J W 2014 Impact of earthquake ground motion characteristics on collapse risk of post-mainshock buildings considering aftershocks *Eng. Struct. 81* 349–61
- [42] Liek Yeo G and Allin Cornell C 2009 Building life-cycle cost analysis due to mainshock and aftershock occurrences *Struct. Saf. 31* 396–408
- [43] Naumoski N and Heidebrecht A 2000 Periods of Reinforced Concrete Frames During Nonlinear Earthquake Response *Proc. 12th World Conf. Earthq. Eng. Auckland, New Zeal. Paper No.* 1–8
- [44] Drive T D 1984 ATC-3-06 Amended Tentative Provisions for the Development of Seismic Regulations for Buildings *Management*
- [45] International Code Council 1997 UBC 1997 Vol 2 - Structural Engineering Design Provisions **2**

- [46] FEMA 2009 NEHRP Recommended Seismic Provisions 383
- [47] Housner G W and A. G. Brady 1963 Natural Periods of Vibration of Buildings *J. Eng. Mech. Div.* **Vol. 89** Pg. 31-68
- [48] Goel R K and Chopra A K 1997 Period Formulas for Moment-Resisting Frame Buildings *J. Struct. Eng.* **123** 1454–61
- [49] Sejdić E, Djurović I and Jiang J 2009 Time-frequency feature representation using energy concentration: An overview of recent advances *Digit. Signal Process. A Rev. J.* **19** 153–83
- [50] Oppenheim A and Schafer R Discrete-Time Signal Processing *Englewood Cliffs, NJ Prentice Hall*
- [51] Fourier J-B-J 1822 *Théorie analytique de la chaleur*
- [52] Anon 2013 ASCE 7-05 Minimum Design Loads for Buildings and Other Structures
- [53] Anon 2012 Seismic Loads Based on IBC 2012 / ASCE 7-10 160–79
- [54] American Institut for Steel Constructions 2005 Specification for Structural Steel Buildings
- [55] Anon 2005 BS EN 1993-1-8:2005 - Eurocode 3: Design of steel structures - Part 1-8: Design of joints *Eurocode 3* **8** 135
- [56] ASCE STANDARD ASCEISEI 7-05 2013 Minimum Design Loads for Buildings and Other Structures
- [57] Elnashai A S, Papanikolaou V K and Lee D H 2006 ZEUS-NL - User Manual

- [58] Geschwindner L F and Disque R O 2006 Flexible moment connections for unbraced frames subjected to lateral forces - A return to simplicity *Eng. J.* **43** 231
- [59] Kilar V and Fajfar P 1996 Simplified push-over analysis of building structures *Elev. World Conf. Earthq. Eng.*
- [60] Anon *International Building Code (2006)*
- [61] FEMA 2011 Hazus-MH 2.1 Hurricane Model User Manual 1–275
- [62] Krawinkler H 1996 Pushover Analysis: Why, How, When, and When Not to Use It 1996 *Conv. Struct. Eng. Assoc. Calif.* 17–36
- [63] Elnashai, Amr S. L D S 2008 INTRODUCTION TO EARTHQUAKE STRUCTURAL ENGINEERING 119
- [64] Seo J, Hu J W and Lee J 2012 Assessment of Seismic Performance of Buildings with Incorporation of Aftershocks *J. Perform. Constr. Facil.* **26** 371–6
- [65] Anon PEER - Pacific Earthquake Engineering Research Center
- [66] Tahir M, Grasso J R and Amorose D 2012 The largest aftershock: How strong, how far away, how delayed? *Geophys. Res. Lett.* **39** 1–5
- [67] Federal Emergency Management Agency 2011 Hazus-MH MR5 Technical Manual. Multi-hazard Loss Estimation Methodology: Earthquake Model 736
- [68] Vamvatsikos D and Cornell C A 2002 The Incremental Dynamic Analysis and Its Application To Performance-Based Earthquake Engineering *Eur. Conf. Earthq. Eng.* 10

- [69] Mahmoud H 2011 Seismic behavior of semi-rigid steel frames *Ph.D. thesis, Dept. Civ. Environ. Eng. Univ. Illinois Urbana-Champaign, Urbana, Illinois.*

## APPENDIX A. STEEL CONNECTION DESIGN

### General

Connection type	Frame bolted
Connection geometry	Single-sided
calculation type	Internal forces
Lc/Combi	1.2D + 1.6L

### Connected beams

Name	CrossSection	Length[m]	Beg. Node	End node	Type
Column	CS3 - W10X100	6.000	N3	N1	Column(100)
Column0	CS3 - W10X100	6.000	N1	N4	Column(100)
beam	CS1 - W21X50	6.000	N1	N2	Beam (80)

### Parts of connection: Side [beam]

#### Bolts

<b>Bolts</b>			
Name		Bolt pattern	2 bolts/row
Internal bolts distance [mm]	127.311700	External bolts distance [mm]	
Length [mm]	75.000000	Reference	Bottom of the beam
1.Location [mm]	566.896000	2.Location [mm]	481.394000
9.Location [mm]	46.927000	10.Location [mm]	-38.576000

## End-plate

EP			
Material	EndPlate	Left Extension [mm]	18.000000
Thickness [mm]	20.000000	Right extension [mm ]	18.000000
Input	Top/Bottom/Left/Right	Total width [mm]	201.862000
Top extension [mm]	76.200000	Total height [mm]	680.720000
bottom extension [mm]	76.200000		

## Strong-axis Calculation

### Connection analysis: Side [beam]

According to EN 1993-1-8

National annex: Standard EN

Partial safety factors	
Gamma M0	1.00
Gamma M1	1.00
Gamma M2	1.25
Gamma M3	1.25

## Internal forces

LC1		
NED	0.00	N
Vz,Ed	4382.05	N
My,Ed	-13146.14	Nm

Vy,Ed	0.00	N
Mz,Ed	0.00	Nm

Tension top

Note:  $NED \leq 0.05 * N_{pl,Rd,Beam}$ .

### Design moment resistance $M_{j,y,Rd}$

### Design resistance of basic components

#### Column web panel in shear

According to En 1993-1-8 Article 6.2.6.1

<b>Vwp,Rd data</b>		
Column web in shear (Vwp,Rd)	962861.51	N
Beta	1.00	
Avc	5371.10	mm <sup>2</sup>

#### Column web in compression

According to EN 1993-1-8 Article 6.2.6.2

<b>Fc,Wc,Rd data</b>		
beff,c,wc	299.84	mm
twc	17.27	mm
$\omega_1$	0.67	
$\omega_2$	0.41	
$\omega$	0.67	
dwc	194.75	mm

$\lambda_{p,rel}$	0.54	
$\rho$	1.00	
k <sub>wc</sub>	1.00	
F <sub>c,Wc,Rd</sub>	1202238.94	N

### Beam flange and web in compression

According to EN 1993-1-8 Article 6.2.6.7

F <sub>c,fb,Rd</sub> data		
Section class	1	
M <sub>c,Rd</sub>	621890.1	Nm
h <sub>b</sub> -t <sub>fb</sub>	514.73	mm
F <sub>c,fb,Rd</sub>	1208184.66	N

### Design tension resistance of bolt-row

According to EN 1993-1-8 Article 3.6

F <sub>t,Rd</sub> data		
f <sub>ub</sub>	1035000.000	KN/m <sup>2</sup>
A <sub>s</sub>	390.97	mm <sup>2</sup>
K <sub>2</sub>	0.90	-
F <sub>t,Rd</sub>	291348.61	N
L <sub>b</sub>	72.59	mm

Note: The bolt-rows are numbered starting from the bolt-row farthest from the center of compression as specified in EN 1993-1-8 Article 6.2.7.2(1).

## Column flange

According to EN 1993-1-8 Article 6.2.6.3, 6.2.6.4

(Effective lengths in mm, resistance in N)

row	m2U	m2L	limit	near stiff, U	near stiff. L	Classification
1	-	-	-	-	-	Other end bolt-row at end of column
2	-	-	-	-	-	Other inner bolt row
3	-	-	-	-	-	Other inner bolt row
4	-	-	-	-	-	Other end bolt-row at end of column

row	p(p1+p2)	e	e1	m	n	$\lambda_{1U}$	$\lambda_{1U}$	$\alpha_U$	$\lambda_{1L}$	$\lambda_{1L}$	$\alpha_L$
1	0.00+42.75	67.15	5697.26	42.9	37.28	-	-	-	-	-	-
2	42.75+217.23	67.15	-	42.9	37.28	-	-	-	-	-	-
3	217.23+42.75	67.15	-	42.9	37.28	-	-	-	-	-	-
4	42.75+00.00	67.15	5697.26	42.9	37.28	-	-	-	-	-	-

row	leff,cp,i	leff,nc,i
1	269.57	255.56
2	269.57	255.56
3	269.57	255.56
4	269.57	255.56

row	leff,cp,g,Inner	leff,nc,g,Inner	leff,cp,g,end	leff,nc,g,end	leff,cp,g,start	leff,nc,g,start
1		-	-	-	220.29	170.53

2	519.97	259.98	220.29	170.53	569.25	345.01
3	519.97	259.99	569.25	345.01	220.29	170.53
4	-	-	220.29	170.53	-	-

group	leff,cp,g	leff,nc,g
1-2	440.58	341.06
1-3	1309.51	775.53
1-4	1480.52	861.03
2-3	1138.51	690.03
2-4	1309.51	775.53
3-4	440.58	341.06

Note: The Alternative method for  $FT,1 < R_d$  according to EN 1993-1-8 Article 6.2.4, Table 6.2 is used.

For individual bolt-row:

row	leff,1	leff,2	Lb*	Prying forces	FT,1,Rd	FT,2,Rd	FT,3,Rd	Ft,fc,Rd,i
1	255.56	255.56	46.18	x	831543.83	831543.83	582697.22	582697.22
2	255.56	255.56	46.18	x	831543.83	831543.83	582697.22	582697.22
3	255.56	255.56	46.18	x	831543.83	831543.83	582697.22	582697.22
4	255.56	255.56	46.18	x	831543.83	831543.83	582697.22	582697.22

row	beff,t,wc	twc	$\omega_1$	$\omega_2$	$\omega$	Ft,wc,Rd,i
1	255.56	17.27	0.73	0.47	0.73	1111238.59
2	255.56	17.27	0.73	0.47	0.73	1111238.59

3	255.56	17.27	0.73	0.47	0.73	1111238.59
4	255.56	17.27	0.73	0.47	0.73	1111238.59

For group of bolt-rows:

group	leff,1	leff,2	Lb*	Prying forces	FT,1,Rd	FT,2,Rd	FT,3,Rd	Ft,fc,Rd,g
1-2	341.06	341.06	69.21	□	1109753.80	1109753.80	1165394.43	1109753.80
1-3	775.53	775.53	45.65	□	2523432.38	2523432.38	1748091.65	1748091.65
1-4	861.03	861.03	54.83	□	2801643.98	2801643.98	2330788.87	2330788.87
2-3	690.03	690.03	34.21	□	2245222.41	2245222.41	1165394.43	1165394.43
2-4	775.53	775.53	45.65	□	2523434.01	2523434.01	1748091.65	1748091.65
3-4	341.06	341.06	69.21	□	1109755.43	1109755.43	1165394.43	1109755.43

group	beff,t,wc	$\omega_1$	$\omega_2$	$\omega$	Ft,wc,Rd,g
1-2	341.06	0.62	0.37	0.62	1269276.70
1-3	775.53	0.33	0.17	0.33	1533164.77
1-4	861.03	0.30	0.16	0.3	1549342.76
2-3	690.03	0.37	0.19	0.37	1511430.00
2-4	775.53	0.33	0.17	0.33	1533164.88
3-4	341.06	0.62	0.37	0.62	1269277.43

## Endplate

According to EN 1993-1-8 Article 6.2.6.5, 6.2.6.8

(effective lengths in mm, resistance in N)

row	m2U	m2L	limit	near flange U	near flange L	Classification
1	-	-	-	-	-	Bolt-row outside of beam
2	22.02	-	146.86	□	-	Bolt-row adjacent to beam flange
3	-	22.02	146.86	-	□	Bolt-row adjacent to beam flange
4	-	-	-	-	-	Bolt-row outside of beam

row	p(p1+p2)	e	ex	m	mx	n	$\lambda 1U$	$\lambda 1U$	$\alpha U$	$\lambda 1L$	$\lambda 1L$	$\alpha L$
1	0.00+0.00	37.28	37.62	-	27.26	34.08	-	-	-	-	-	-
2	0.00+217.23	37.28	-	50.91	-	37.28	0.58	0.25	6.18	-	-	-
3	217.23+0.00	37.28	-	50.91	-	37.28	-	-	-	0.58	0.25	6.18
4	0.00+0.00	37.28	37.62	-	27.26	34.08	-	-	-	-	-	-

row	leff,cp,i	leff,nc,i
1	160.90	100.93
2	319.88	314.57
3	319.88	314.57
4	160.90	100.93

row	leff,cp,g,Inner	leff,nc,g,Inner	leff,cp,g,end	leff,nc,g,end	leff,cp,g,start	leff,nc,g,start
1	-	-	-	-	-	-
2	-	-	-	-	594.41	406.68
3	-	-	594.41	406.68	-	-

4	-	-	-	-	-	-
---	---	---	---	---	---	---

group	leff,cp,g	leff,nc,g
2-3	1188.81	813.37

Note: The Alternative method for FT, 1, Rd according to EN 1993-1-8 Article 6.2.4, Table 6.2 is used.

For individual of bolt-row:

row	leff,1	leff,2	Lb*	Prying forces	FT,1,Rd	FT,2,Rd	FT,3,Rd	Ft,ep,Rd,i
1	100.93	100.93	86.34	<input type="checkbox"/>	534397.16	405990.72	582697.22	405990.72
2	314.57	314.57	180.4	<input type="checkbox"/>	768791.36	424656.07	582697.22	424656.07
3	314.57	314.57	180.4	<input type="checkbox"/>	768791.36	424656.07	582697.22	424656.07
4	100.93	100.93	86.34	<input type="checkbox"/>	534411.69	405992.23	582697.22	405992.23

row	beff,t,wb	Ft,wb,Rd,i
1	-	-
2	314.57	1047488.65
3	314.57	1047488.65
4	-	-

For group of bolt-rows:

group	leff,1	leff,2	Lb*	Prying forces	FT,1,Rd	FT,2,Rd	FT,3,Rd
2-3	813.37	813.37	139.54	□	1987840.02	953769.37	1165394.43

group	b <sub>eff,t,wb</sub>	F <sub>t,wb,Rd,g</sub>
2-3	813.37	2708458.96

### Force Distribution in Bolt-rows

### Potential Tension Resistance

According to EN 1993-1-8 Article 6.2.7.2 (6),(8)

row	F <sub>t,fc,Rd,i</sub>	F <sub>t,fc,Rd,g</sub>	F <sub>t,wc,Rd,i</sub>	F <sub>t,wc,Rd,g</sub>	F <sub>t,ep,Rd,i</sub>	F <sub>t,ep,Rd,g</sub>	F <sub>t,wb,Rd,i</sub>	F <sub>t,wb,Rd,g</sub>	F <sub>t,r,Rd</sub>
1	582697.22	-	1111238.59	-	405990.72	-	-	-	405990.72
2	582697.22	703763.08	1111238.59	863285.98	424656.07	-	1047488.65	-	424656.07
3	582697.22	740738.36	1111238.59	702517.97	424656.07	529113.29	1047488.65	2283802.88	424656.07
4	582697.22	685099.36	1111238.59	294039.90	405992.23	-	-	-	294039.90

$$\sum F_t, Rd = 1549342.76 \text{ N}$$

### Assessment of the Shear and Compression Zone

According to EN 1993-1-8 Article 6.2.7.2(7)

column web in shear (V <sub>wp,Rd</sub> /Beta)	962861.51	N
Column web in compression (F <sub>c</sub> , W <sub>c,Rd</sub> )	1202238.94	N
Beam flange and web in compression ( F <sub>c,fb,Rd</sub> )	1208184.66	N

Limiting resistance = 962861.51 N

row	Ft,r,Rd	Decrease	Ft,r,Rd
1	405990.72	0	405990.72
2	424656.07	0	424656.07
3	424656.07	292441.36	132214.72
4	294039.90	294039.90	0

### Triangular Limit

According to EN 1993-1-8 Article 6.2.7.2(9)

Limit:  $1.9 \cdot Ft,Rd = 553562.36 \text{ N}$

row	Ft,r,Rd	>Limit	Decrease	Ft,r,Rd
1	405990.72	<input type="checkbox"/>	-	405990.7
2	424656.07	<input type="checkbox"/>	-	424656.1
3	132214.72	<input type="checkbox"/>	-	132214.7
4	0	<input type="checkbox"/>	-	0

### Determination of $M_j, y, Rd$

According to EN 1993-1-8 Article 6.2.7.2(1)

row	hr[mm]	Ft,r,Rd[N]
1	560.10	405990.72
2	474.60	424656.07
3	40.13	132214.72
4	-45.37	0

$M_j, y, Rd = 434243.88 \text{ Nm}$

## Determination of $N_{j,Rd}$

According to EN 1993-1-8 Article 6.2.7.1(3)

data		
Column Web in tension ( $F_{t,wc,Rd}$ )	1549342.76	N
Beam Web in tension ( $F_{t,wb,Rd}$ )	2094977.29	N
Endplate in bending ( $F_{t,ep,Rd}$ )	1661295.1	N
Column flange in bending ( $F_{t,fc,Rd}$ )	2219509.23	N

$N_{j,Rd} = 1549342.76 \text{ N}$

## Design Shear Resistance $V_{z,Rd}$

$V_{z,Rd}$ data		
$F_{v,Rd}$	161860.34	N
nb,full	2	
nb,reduced	6	
$e_{1,ep}$	37.62	mm
$p_1$	85.5	mm
$k_1$ plate	2.17	
$k_1$ beam	2.5	
$\alpha_b$ plate	0.46	
$\alpha_b$ column	0.46	
$\alpha_d$ plate	0.46	
$\alpha_d$ column	0.46	
$F_{b,ep,Rd}$	110515.73	N
$F_{b,cf,Rd}$	261911.97	N

Avz	5528.31	m m <sup>2</sup>
I1 (tension)	1	
I2 (compression)	0	
Vz,Rd beam	550580.5	N
Vz,Rd	550580.5	N

## Stiffness calculation

### Design rotational stiffness

According to EN 1993-1-8 Article 6.3.4

row	k3[mm]	k4[mm]	k5[mm]	k10[mm]	keff[mm]
1	10.59	44.74	35.86	8.62	3.84
2	10.59	44.74	17.16	8.62	3.44
3	10.59	44.74	17.16	8.62	3.44

Sj data		
Sj	118908448099.22	Nmm/rad
Sj,ini	118908448099.22	Nmm/rad
z	506.21	mm
mu	1	
k1	4.03	mm
k2	18.61	mm
keq	7.74	mm

## Stiffness Classification

Stiffness data		
E	200000000.00	kN/ m <sup>2</sup>
I <sub>b</sub>	409572000.00	mm <sup>4</sup>
L <sub>b</sub>	6000.00	mm
frame type	Unbraced	
S <sub>j,rigid</sub>	341310000000.00	Nmm/rad
S <sub>j,pinned</sub>	6826200000.00	Nmm/rad

System SEMI RIGID

## Stiffness Check

Stiffness data		
F <sub>i y</sub>	68623673330.80	Nmm/rad
Stiffness modification coef.	2.00	
S <sub>j,app</sub>	137247346661.61	Nmm/rad
S <sub>j,lower boundary</sub>	82239475410.04	Nmm/rad
S <sub>j,upper boundary</sub>	295218714755.80	Nmm/rad

S<sub>j, ini</sub> is inside the boundaries.

The actual joint stiffness conforms to the joint stiffness of the analysis model.

## Ductility Classification

The failure mode is situated in the column shear zone.

This results in a ductile classification for ductility: class 1.

## Design calculations

### Flange welds

data		
M <sub>j,y,Rd</sub>	434243.88	Nm
a	1.7	
h	514.73	mm
FR <sub>d</sub>	1434175.52	N
N <sub>t,Rd</sub>	777595.06	N
f <sub>u</sub>	270000	kN/ m <sup>2</sup>
β <sub>w</sub>	0.85	
minimum af	9.45	mm
af	10	mm

### Web welds

data		
F <sub>t</sub>	424656.07	N
F <sub>v</sub>	1095.51	N
l <sub>w</sub>	314.57	mm
f <sub>u</sub>	2700000	kN/ m <sup>2</sup>
β <sub>w</sub>	0.85	
minimum a <sub>w</sub> (a <sub>2</sub> )	6.71	mm
a <sub>w</sub>	7	mm

APPENDIX B. EARTHQUAKES RECORDS FROM PEER NGA DATABASE

Table B.1 Far-field ground motion records set

<b>ID No.</b>	<b>RSN</b>	<b>Earthquake</b>	<b>Year</b>	<b>M</b>	<b>Recording Station</b>
1	953	Northridge	1994	6.7	Beverly Hills - Mulhol
2	960	Northridge	1994	6.7	Canyon Country-WLC
3	1602	Duzce, Turkey	1999	7.1	Bolu
4	1787	Hector Mine	1999	7.1	Hector
5	169	Imperial Valley	1979	6.5	Delta
6	174	Imperial Valley	1979	6.5	El Centro Array #11
7	1111	Kobe, Japan	1995	6.9	Nishi-Akashi
8	1116	Kobe, Japan	1995	6.9	Shin-Osaka
9	1158	Kocaeli, Turkey	1999	7.5	Duzce
10	1148	Kocaeli, Turkey	1999	7.5	Arcelik
11	900	Landers	1992	7.3	Yermo Fire Station
12	848	Landers	1992	7.3	Coolwater
13	752	Loma Prieta	1989	6.9	Capitola
14	767	Loma Prieta	1989	6.9	Gilroy Array #3
15	1633	Manjil, Iran	1990	7.4	Abbar
16	721	Superstition Hills	1987	6.5	El Centro Imp. Co.
17	725	Superstition Hills	1987	6.5	Poe Road (temp)

18	829	Cape Mendocino	1992	7.0	Rio Dell Overpass
19	1244	Chi-Chi, Taiwan	1999	7.6	CHY101
20	1485	Chi-Chi, Taiwan	1999	7.6	TCU045
21	68	San Fernando	1971	6.6	LA - Hollywood Stor
22	125	Friuli, Italy	1976	6.5	Tolmezzo

**Table B.2 Site and source data for far-field records set**

Site Data			Site-Source Distance (km)				
EQ ID	NEHRP Class	Vs <sub>30</sub> (m/sec)	Source (Fault Type)	Epical	Closest to Plane	Campbell	Joyner-Boore
12011	D	356	Thrust	13.3	17.2	17.2	9.4
12012	D	309	Thrust	26.5	12.4	12.4	11.4
12041	D	326	Strike-slip	41.3	12	12.4	12
12052	C	685	Strike-slip	26.5	11.7	12	10.4
12061	D	275	Strike-slip	33.7	22	22.5	22
12062	D	196	Strike-slip	29.4	12.5	13.5	12.5
12071	C	609	Strike-slip	8.7	7.1	25.2	7.1
12072	D	256	Strike-slip	46	19.2	28.5	19.1
12081	D	276	Strike-slip	98.2	15.4	15.4	13.6
12082	C	523	Strike-slip	53.7	13.5	13.5	10.6
12091	D	354	Strike-slip	86	23.6	23.8	23.6
12092	D	271	Strike-slip	82.1	19.7	20	19.7
12101	D	289	Strike-slip	9.8	15.2	35.5	8.7

12102	D	350	Strike-slip	31.4	12.8	12.8	12.2
12111	C	724	Strike-slip	40.4	12.6	13	12.6
12121	D	192	Strike-slip	35.8	18.2	18.5	18.2
12122	D	208	Strike-slip	11.2	11.2	11.7	11.2
12132	D	312	Thrust	22.7	14.3	14.3	7.9
12141	D	259	Thrust	32	10	15.5	10
12142	C	705	Thrust	77.5	26	26.8	26
12151	D	316	Thrust	39.5	22.8	25.9	22.8
12171	C	425	Thrust	20.2	15.8	15.8	15

**Table B.3 Summary of PEER NGA Database information and parameters for far-field set**

PEER-NGA Record Information					Recorded Motions	
File Names - Horizontal Records						
EQ ID	RSN	Lowest	Component 1	Component 2	PGA <sub>max</sub> (g)	PGV <sub>ma</sub>
		Freq (Hz.)				x (cm/s.)
12011	953	0.25	NORTHR/MUL009	NORTHR/MUL279	0.52	63
12012	960	0.13	NORTHR/LOS000	NORTHR/LOS270	0.48	45
12041	1602	0.06	DUZCE/BOL000	DUZCE/BOL090	0.82	62
12052	1787	0.04	HECTOR/HEC000	HECTOR/HEC090	0.34	42
12061	169	0.06	IMPVALL/H-DLT262	IMPVALL/H-DLT352	0.35	33
12062	174	0.25	IMPVALL/H-E11140	IMPVALL/H-E11230	0.38	42
12071	1111	0.13	KOBE/NIS000	KOBE/NIS090	0.51	37

12072	1116	0.13	KOBE/SHI000	KOBE/SHI090	0.24	38
12081	1158	0.24	KOCAELI/DZC180	KOCAELI/DZC270	0.36	59
12082	1148	0.09	KOCAELI/ARC000	KOCAELI/ARC090	0.22	40
12091	900	0.07	LANDERS/YER270	LANDERS/YER360	0.24	52
12092	848	0.13	LANDERS/CLW-LN	LANDERS/CLW-TR	0.42	42
12101	752	0.13	LOMAP/CAP000	LOMAP/CAP090	0.53	35
12102	767	0.13	LOMAP/G03000	LOMAP/G03090	0.56	45
12111	1633	0.13	MANJIL/ABBAR--L	MANJIL/ABBAR--T	0.51	54
12121	721	0.13	SUPERST/B-ICC000	SUPERST/B-ICC090	0.36	46
12122	725	0.25	SUPERST/B-POE270	SUPERST/B-POE360	0.45	36
12132	829	0.07	CAPEMEND/RIO270	CAPEMEND/RIO360	0.55	44
12141	1244	0.05	CHICHI/CHY101-E	CHICHI/CHY101-N	0.44	115
12142	1485	0.05	CHICHI/TCU045-E	CHICHI/TCU045-N	0.51	39
12151	68	0.25	SFERN/PEL090	SFERN/PEL180	0.21	19
12171	125	0.13	FRIULI/A-TMZ000	FRIULI/A-TMZ270	0.35	31

**Table B.4 Mainshock ground motions downloaded from PEER NGA Database**

Sr	No	Earthquake Name	Station	Mainshocks		
				RSN	M	PGA
	1	"Friuli_ Italy-02"	"Buia"	130	5.91	0.110
	2	"Friuli_ Italy-02"	"Buia"	130	5.91	0.094
	3	"Friuli_ Italy-02"	"Forgaria Cornino"	132	5.91	0.261
	4	"Friuli_ Italy-02"	"Forgaria Cornino"	132	5.91	0.212

5	"Friuli_ Italy-02"	"San Rocco"	133	5.91	0.060
6	"Friuli_ Italy-02"	"San Rocco"	133	5.91	0.134
7	"Umbria Marche_ Italy"	"Aquilpark-Citta"	4342	6	0.004
8	"Umbria Marche_ Italy"	"Aquilpark-Citta"	4342	6	0.004
9	"Umbria Marche_ Italy"	"Aquilpark-Galleria"	4343	6	0.003
10	"Umbria Marche_ Italy"	"Aquilparka-Galleria"	4343	6	0.004
11	"Umbria Marche_ Italy"	"Aquilpark-Parcheggio"	4344	6	0.004
12	"Umbria Marche_ Italy"	"Aquilpark-Parcheggio"	4344	6	0.003
13	"Umbria Marche_ Italy"	"Assisi-Stallone"	4345	6	0.188
14	"Umbria Marche_ Italy"	"Assisi-Stallone"	4345	6	0.166
15	"Umbria Marche_ Italy"	"Bevagna"	4346	6	0.079
16	"Umbria Marche_ Italy"	"Bevagna"	4346	6	0.073
17	"Umbria Marche_ Italy"	"Borgo-Cerreto Torre"	4347	6	0.073
18	"Umbria Marche_ Italy"	"Borgo-Cerreto Torre"	4347	6	0.110
19	"Umbria Marche_ Italy"	"Colfiorito"	4349	6	0.198
20	"Umbria Marche_ Italy"	"Colfiorito"	4349	6	0.201
21	"Umbria Marche_ Italy"	"Gubbio-Piana"	4350	6	0.093
22	"Umbria Marche_ Italy"	"Gubbio-Piana"	4350	6	0.096
23	"Umbria Marche_ Italy"	"Nocera Umbra"	4352	6	0.472
24	"Umbria Marche_ Italy"	"Nocera Umbra"	4352	6	0.383
25	"Umbria Marche_ Italy"	"Rieti"	4353	6	0.017
26	"Umbria Marche_ Italy"	"Rieti"	4353	6	0.019
27	"L'Aquila_ Italy"	"GRAN SASSO (Assergi)"	4477	6.3	0.150

28	"L'Aquila_ Italy"	"GRAN SASSO (Assergi)"	4477	6.3	0.145
29	"L'Aquila_ Italy"	"L'Aquila-V. Aterno-Centro Valle"	4480	6.3	0.664
30	"L'Aquila_ Italy"	"L'Aquila-V. Aterno-Centro Valle"	4480	6.3	0.556
31	"L'Aquila_ Italy"	"L'Aquila-V. Aterno-Colle Grilli"	4481	6.3	0.482
32	"L'Aquila_ Italy"	"L'Aquila-V. Aterno-Colle Grilli"	4481	6.3	0.517
33	Hollister-01 EW	Hollister City Hall	26	5.6	0.059
34	Hollister-01 NS	Hollister City Hall	26	5.6	0.115
35	Imperial Vally-06EW	Bonds Corner	160	6.53	0.599
36	Imperial Vally-06NS	Bonds Corner	160	6.53	0.777
37	Livermore-01 EW	Del Valle Dam (Toe)	212	5.8	0.130
38	Livermore-01 NS	Del Valle Dam (Toe)	212	5.8	0.256
39	MammLakes-01 EW	Convict Creek	230	6.06	0.419
40	MammLakes-01 NS	Convict Creek	230	6.06	0.442
41	MammLakes-03 EW	Long Valley Dam (Upr L Abut)	239	5.91	0.482
42	MammLakes-03 NS	Long Valley Dam (Upr L Abut)	239	5.91	0.195
43	Irpinia_Italy-01 EW	Bagnoli Irpinio	285	6.9	0.130
44	Irpinia_Italy-01 NS	Bagnoli Irpinio	285	6.9	0.190
45	Irpinia_Italy-01 EW	Tricarico	294	6.9	0.047
46	Irpinia_Italy-01 NS	Tricarico	294	6.9	0.036
47	Coalinga-01 EW	Pleasant Valley P.P. - yard	368	6.36	0.602
48	Coalinga-01 NS	Pleasant Valley P.P. - yard	368	6.36	0.525
49	Northridge-01 EW	Newhall - Fire Sta	1044	6.69	0.583
50	Northridge-01 NS	Newhall - Fire Sta	1044	6.69	0.590

51	ChiChi-01 EW	CHY028	1197	7.62	0.636
52	ChiChi-01 NS	CHY028	1197	7.62	0.760
53	"Friuli_ Italy-01"	Tolmezzo"	125	6.5	0.357
54	"Friuli_ Italy-01"	"Tolmezzo"	125	6.5	0.315
55	"Imperial Valley-06"	"Delta"	169	6.53	0.236
56	"Imperial Valley-06"	"Delta"	169	6.53	0.350
57	"Imperial Valley-06"	"El Centro Array #11"	174	6.53	0.367
58	"Imperial Valley-06"	"El Centro Array #11"	174	6.53	0.379
59	"Chi-Chi_ Taiwan"	"CHY101"	1244	7.62	0.249
60	"Chi-Chi_ Taiwan"	"CHY101"	1244	7.62	0.261
61	"Chi-Chi_ Taiwan"	"TCU045"	1485	7.62	0.075
62	"Chi-Chi_ Taiwan"	"TCU045"	1485	7.62	0.083
63	"Imperial Valley-06"	"Bonds Corner"	160	6.53	0.599
64	"Imperial Valley-06"	"Bonds Corner"	160	6.53	0.777
65	"Irpinia_ Italy-01"	"Bagnoli Irpinio"	285	6.9	0.130
66	"Irpinia_ Italy-01"	"Bagnoli Irpinio"	285	6.9	0.190
67	"Northridge-01"	"Newhall - Fire Sta"	1044	6.69	0.583
68	"Northridge-01"	"Newhall - Fire Sta"	1044	6.69	0.590

**Table B.5 Aftershock ground motions downloaded from PEER NGA Database**

Sr No	Earthquake Name	Station	Aftershocks		
			RSN	M	PGA
1	"Friuli_ Italy-02"	"Buia"	4276	5.5	0.231
2	"Friuli_ Italy-02"	"Buia"	4279	4.8	0.062
3	"Friuli_ Italy-02"	"Forgaria Cornino"	4274	5.2	0.044
4	"Friuli_ Italy-02"	"Forgaria Cornino"	4271	4.7	0.082
5	"Friuli_ Italy-02"	"San Rocco"	4278	5.5	0.090
6	"Friuli_ Italy-02"	"San Rocco"	4278	5.5	0.090
7	"Umbria Marche_ Italy"	"Aquilpark-Citta"	4359	5.5	0.003
8	"Umbria Marche_ Italy"	"Aquilpark-Citta"	4359	5.5	0.004
9	"Umbria Marche_ Italy"	"Aquilpark-Galleria"	4360	5.5	0.003
10	"Umbria Marche_ Italy"	"Aquilpark-Galleria"	4360	5.5	0.002
11	"Umbria Marche_ Italy"	"Aquilpark-Parcheggio"	4361	5.5	0.003
12	"Umbria Marche_ Italy"	"Aquilpark-Parcheggio"	4361	5.5	0.003
13	"Umbria Marche_ Italy"	"Assisi-Stallone"	4362	5.5	0.103
14	"Umbria Marche_ Italy"	"Assisi-Stallone"	4362	5.5	0.188
15	"Umbria Marche_ Italy"	"Bevagna"	4363	5.5	0.036
16	"Umbria Marche_ Italy"	"Bevagna"	4363	5.5	0.052
17	"Umbria Marche_ Italy"	"Borgo-Cerreto Torre"	4377	5.2	0.169
18	"Umbria Marche_ Italy"	"Borgo-Cerreto Torre"	4383	5.6	0.334
19	"Umbria Marche_ Italy"	"Colfiorito"	4364	5.5	0.130

20	"Umbria Marche_ Italy"	"Colfiorito"	4364	5.5	0.107
21	"Umbria Marche_ Italy"	"Gubbio-Piana"	4366	5.5	0.073
22	"Umbria Marche_ Italy"	"Gubbio-Piana"	4366	5.5	0.059
23	"Umbria Marche_ Italy"	"Nocera Umbra"	4367	5.5	0.450
24	"Umbria Marche_ Italy"	"Nocera Umbra"	4367	5.5	0.294
25	"Umbria Marche_ Italy"	"Rieti"	4370	5.5	0.014
26	"Umbria Marche_ Italy"	"Rieti"	4370	5.5	0.017
27	"L'Aquila_ Italy"	"GRAN SASSO (Assergi)"	4508	5.6	0.283
28	"L'Aquila_ Italy"	"GRAN SASSO (Assergi)"	4508	5.6	0.252
		"L'Aquila-V. Aterno-Centro			
29	"L'Aquila_ Italy"	Valle"	4510	5.6	0.130
		"L'Aquila-V. Aterno-Centro			
30	"L'Aquila_ Italy"	Valle"	4510	5.6	0.148
		"L'Aquila-V. Aterno-Colle			
31	"L'Aquila_ Italy"	Grilli"	4509	5.6	0.146
		"L'Aquila-V. Aterno-Colle			
32	"L'Aquila_ Italy"	Grilli"	4509	5.6	0.106
33	Hollister-01 EW	Hollister City Hall	27	5.5	0.059
34	Hollister-01 NS	Hollister City Hall	27	5.5	0.070
35	Imperial Vally-06EW	Bonds Corner	193	5.01	0.071
36	Imperial Vally-06NS	Bonds Corner	193	5.01	0.129
37	Livermore-01 EW	Del Valle Dam (Toe)	219	5.42	0.0388
38	Livermore-01 NS	Del Valle Dam (Toe)	219	5.42	0.04495

39	MammLakes-01 EW	Convict Creek	233	5.69	0.16341
40	MammLakes-01 NS	Convict Creek	233	5.69	0.1825
41	MammLakes-03 EW	Long Valley Dam (Upr L Abut)	243	5.7	0.30183
42	MammLakes-03 NS	Long Valley Dam (Upr L Abut)	243	5.7	0.15851
43	Irpinia_Italy-01 EW	Bagnoli Irpinio	296	6.2	0.05594
44	Irpinia_Italy-01 NS	Bagnoli Irpinio	296	6.2	0.04966
45	Irpinia_Italy-01 EW	Tricarico	304	6.2	0.02121
46	Irpinia_Italy-01 NS	Tricarico	304	6.2	0.02357
47	Coalinga-01 EW	Pleasant Valley P.P. - yard	383	5.09	0.09863
48	Coalinga-01 NS	Pleasant Valley P.P. - yard	383	5.09	0.21067
49	Northridge-01 EW	Newhall - Fire Sta	1656	6.05	0.03309
50	Northridge-01 NS	Newhall - Fire Sta	1656	6.05	0.02939
51	ChiChi-01 EW	CHY028	2163	5.9	0.03716
52	ChiChi-01 NS	CHY028	2163	5.9	0.04394
53	"Friuli_Italy-01"	"Tolmezzo"	4267	5.2	0.11737
54	"Friuli_Italy-01"	"Tolmezzo"	4267	5.2	0.0729
55	"Imperial Valley-06"	"Delta"	196	5.01	0.06038
56	"Imperial Valley-06"	"Delta"	196	5.01	0.11831
57	"Imperial Valley-06"	"El Centro Array #11"	199	5.01	0.0972
58	"Imperial Valley-06"	"El Centro Array #11"	199	5.01	0.19243
59	"Chi-Chi_Taiwan"	"CHY101"	2206	5.9	0.03526
60	"Chi-Chi_Taiwan"	"CHY101"	2206	5.9	0.03988
61	"Chi-Chi_Taiwan"	"TCU045"	2367	5.9	0.0236

62	"Chi-Chi_ Taiwan"	"TCU045"	2367	5.9	0.02212
63	"Imperial Valley-06"	"Bonds Corner"	193	5.01	0.07052
64	"Imperial Valley-06"	"Bonds Corner"	193	5.01	0.12886
65	"Irpinia_ Italy-01"	"Bagnoli Irpinioa"	296	6.2	0.05594
66	"Irpinia_ Italy-01"	"Bagnoli Irpinioa"	296	6.2	0.04966
67	"Northridge-01"	"Newhall - Fire Sta"	1665	6.05	0.03653
68	"Northridge-01"	"Newhall - Fire Sta"	1665	6.05	0.04355

**Table B.6 Details of the selected mainshocks for the analysis**

<b>Result</b>					
<b>ID</b>	<b>RSN</b>	<b>Earthquake Name</b>	<b>Station Name</b>	<b>Magnitude</b>	
1	26	"Hollister-01"	"Hollister City Hall"	5.6	
2	125	"Friuli_ Italy-01"	"Tolmezzo"	6.5	
3	133	"Friuli_ Italy-02"	"San Rocco"	5.91	
4	169	"Imperial Valley-06"	"Delta"	6.53	
5	174	"Imperial Valley-06"	"El Centro Array #11"	6.53	
6	239	"Mammoth Lakes-03"	"Long Valley Dam (Upr L Abut)"	5.91	
7	285	"Irpinia_ Italy-01"	"Bagnoli Irpinio"	6.9	
8	4345	"Umbria Marche_ Italy"	"Assisi-Stallone"	6	
9	4346	"Umbria Marche_ Italy"	"Bevagna"	6	
10	4347	"Umbria Marche_ Italy"	"Borgo-Cerreto Torre"	6	
11	4352	"Umbria Marche_ Italy"	"Nocera Umbra"	6	

**Table B.7 Details of the selected aftershocks for the analysis**

<b>Result</b>				
<b>ID</b>	<b>RSN</b>	<b>Earthquake Name</b>	<b>Station Name</b>	<b>M</b>
1	27	"Hollister-02"	"Hollister City Hall"	5.5
2	4267	"Friuli (aftershock 1)_ Italy"	"Tolmezzo"	5.2
3	4278	"Friuli (aftershock 9)_ Italy"	"San Rocco"	5.5
4	196	"Imperial Valley-07"	"Delta"	5.01
5	199	"Imperial Valley-07"	"El Centro Array #11"	5.01
6	243	"Mammoth Lakes-04"	"Long Valley Dam"	5.7
7	296	"Irpinia_ Italy-02"	"Bagnoli Irpinio"	6.2
8	4362	"Umbria Marche (aftershock 1)_ Italy"	"Assisi-Stallone"	5.5
9	4363	"Umbria Marche (aftershock 1)_ Italy"	"Bevagna"	5.5
10	4377	"Umbria Marche (aftershock 8)_ Italy"	"Borgo-Cerreto Torre"	5.2
11	4367	"Umbria Marche (aftershock 1)_ Italy"	"Nocera Umbra"	5.5

**Table B.8 PGA values of the mainshock horizontal components**

<b>Result</b>			
<b>ID</b>	<b>RSN</b>	<b>Horizontal Acc. Filename</b>	<b>PGAs</b>
1	26	RSN26_HOLLISTR_B-HCH181.AT2	0.05842
2	26	RSN26_HOLLISTR_B-HCH271.AT2	0.11475
3	125	RSN125_FRIULI.A_A-TMZ000.AT2	0.35713
4	125	RSN125_FRIULI.A_A-TMZ270.AT2	0.31445

5	133	RSN133_FRIULI.B_B-SRO000.AT2	0.05977
6	133	RSN133_FRIULI.B_B-SRO270.AT2	0.13401
7	169	RSN169_IMPVAL.L_H_H-DLT262.AT2	0.2357
8	169	RSN169_IMPVAL.L_H_H-DLT352.AT2	0.3497
9	174	RSN174_IMPVAL.L_H_H-E11140.AT2	0.36681
10	174	RSN174_IMPVAL.L_H_H-E11230.AT2	0.37748
11	239	RSN239_MAMMOTH.AH_A-LUL000.AT2	0.48221
12	239	RSN239_MAMMOTH.AH_A-LUL090.AT2	0.19464
13	285	RSN285_ITALY_A-BAG000.AT2	0.12931
14	285	RSN285_ITALY_A-BAG270.AT2	0.1897
15	4345	RSN4345_UBMARCHE.P_A-AAL018.AT2	0.18804
16	4345	RSN4345_UBMARCHE.P_A-AAL108.AT2	0.16613
17	4346	RSN4346_UBMARCHE.P_A-BEV000.AT2	0.07797
18	4346	RSN4346_UBMARCHE.P_A-BEV270.AT2	0.07308
19	4347	RSN4347_UBMARCHE.P_A-BCT000.AT2	0.07256
20	4347	RSN4347_UBMARCHE.P_A-BCT090.AT2	0.10939
21	4352	RSN4352_UBMARCHE.P_A-NCR000.AT2	0.47227
22	4352	RSN4352_UBMARCHE.P_A-NCR270.AT2	0.37896

**Table B.9 PGA values of the aftershock horizontal components**

<b>Result</b>			
<b>ID</b>	<b>RSN</b>	<b>Horizontal Acc. Filename</b>	<b>PGAs</b>
1	27	RSN27_HOLLISTR_C-HCH181.AT2	0.05895
2	27	RSN27_HOLLISTR_C-HCH271.AT2	0.07008
3	4267	RSN4267_FRIULI.P_C-TMZ000.AT2	0.11737
4	4267	RSN4267_FRIULI.P_C-TMZ090.AT2	0.0729
5	4278	RSN4278_FRIULI.P_W-SRO000.AT2	0.08927
6	4278	RSN4278_FRIULI.P_W-SRO090.AT2	0.09022
7	196	RSN196_IMPVAL.L.A_A-DLT262.AT2	0.05905
8	196	RSN196_IMPVAL.L.A_A-DLT352.AT2	0.11831
9	199	RSN199_IMPVAL.L.A_A-E11140.AT2	0.09609
10	199	RSN199_IMPVAL.L.A_A-E11230.AT2	0.19243
11	243	RSN243_MAMMOTH.AH_B-LUL000.AT2	0.30183
12	243	RSN243_MAMMOTH.AH_B-LUL090.AT2	0.15851
13	296	RSN296_ITALY_B-BAG000.AT2	0.05546
14	296	RSN296_ITALY_B-BAG270.AT2	0.04963
15	4362	RSN4362_UBMARCHE.P_E-AAL018.AT2	0.10292
16	4362	RSN4362_UBMARCHE.P_E-AAL108.AT2	0.18702
17	4363	RSN4363_UBMARCHE.P_E-BEV000.AT2	0.03578
18	4363	RSN4363_UBMARCHE.P_E-BEV270.AT2	0.05188
19	4377	RSN4377_UBMARCHE.P_I-BCT000.AT2	0.16126

20	4377	RSN4377_UBMARCHE.P_I-BCT090.AT2	0.16169
21	4367	RSN4367_UBMARCHE.P_E-NCR000.AT2	0.44906
22	4367	RSN4367_UBMARCHE.P_E-NCR270.AT2	0.29385

**Table B.10 PGA values for the mainshock and aftershock records scaled for 70% $M_{pb}$  Model**

Result ID	Mainshock PGA	Aftershock
	Value (g)	PGA Value (g)
1	6.17	3.95
2	4.64	2.97
3	2.01	1.30
4	1.72	1.11
5	5.64	3.61
6	4.14	2.65
7	0.86	0.56
8	1.17	0.76
9	1.29	0.84
10	1.28	0.83
11	0.45	0.30
12	0.56	0.37
13	0.77	0.51
14	1.34	0.87
15	1.27	0.82
16	4.12	2.64

17	0.56	0.37
18	0.47	0.32
19	3.01	1.93
20	3.37	2.16
21	6.21	3.97
22	2.78	1.79